

THESIS ON MECHANICAL ENGINEERING E90

Morphological Changes on Diamond and DLC Films During Sliding Wear

ANDREI BOGATOV

TUT
PRESS

TALLINN UNIVERSITY OF TECHNOLOGY
Faculty of Mechanical Engineering
Department of Materials Engineering

Dissertation was accepted for the defence of the degree of Doctor of Philosophy in Engineering on December 1st, 2014

Supervisor: Sen. res. Vitali Podgurski, PhD, Department of Materials Engineering, Tallinn University of Technology

Opponents: Ilmo Sildos, PhD, Institute of Physics, University of Tartu, Estonia

Helena Ronkainen, Dr. (Tech.), VTT Technical Research Centre of Finland

Defence of the thesis: February 4th, 2015

Declaration:

Hereby I declare that this doctoral thesis, my original investigation and achievement, submitted for the doctoral degree at Tallinn University of Technology has not been submitted for doctoral or equivalent academic degree.

/Andrei Bogatov/

Copyright: Andrei Bogatov, 2015
ISSN 1406-4758
ISBN 978-9949-23-730-2 (publication)
ISBN 978-9949-23-731-9 (PDF)

MEHHANOTEHNIKA E90

**Morfoloogilised muutused teemant- ja
teemandilaadsetel pinnitel liugkulumisel**

ANDREI BOGATOV

CONTENTS

PUBLICATIONS	6
INTRODUCTION.....	7
ABBREVIATIONS.....	9
1 REVIEW OF LITERATURE.....	10
1.1 Classification of carbon-based materials.....	10
1.1.1 Allotropes of carbon	11
1.1.2 Diamond and DLC films	16
1.2 CVD diamond growth mechanisms	19
1.3 Mechanical and tribological properties of diamond and DLC films.....	21
1.3.1 Anisotropy of mechanical properties of diamond.....	21
1.3.2 Wear of diamond and DLC films	24
1.4 Objectives of the thesis.....	29
2 METHODS AND TOOLS	31
2.1 Diamond and DLC films deposition methods.....	31
2.2 Characterization methods	33
2.3 Surface texture parameters	35
2.4 Statistical analysis of data	36
3 WEAR BEHAVIOR OF NCD AND DLC FILMS.....	38
3.1 Wear behavior of NCD films	38
3.1.1 Relation between morphological changes of the NCD films and the ball material.....	38
3.1.2 Relation between morphological changes of the NCD films and the sliding distance.....	46
3.1.3 Deformation of the NCD films during sliding tests	49
3.2 Wear behavior of the DLC films.....	56
CONCLUSIONS	62
REFERENCES.....	64
ACKNOWLEDGEMENTS	71
ABSTRACT	72
KOKKUVÕTE.....	73
APPENDICES.....	75
Curriculum vitae	77
Elulookirjeldus	79
Publications.....	81

PUBLICATIONS

The present thesis is based on the following papers, which are referred in the text as Publications I – IV

- Publication I. Podgursky, V., Hantschel, T., Bogatov, A., Kimmari, E., Antonov, M., Viljus, M., Mikli, V., Tsigkourakos, M., Vandevorst, W., Buijnsters, J. G., Raadik, A. T., Kulu, P. Rippling on wear scar surfaces of nanocrystalline diamond films after reciprocating sliding against ceramic balls. *Tribology Letters*. 2014, Vol. 55, 3, 493 - 503
- Publication II. Bogatov, A., Podgursky, V., Raadik, A. T., Kamjula, A. R., Hantschel, T., Tsigkourakos, M., Kulu, P. Investigation of morphology changes on nanocrystalline diamond film surfaces during reciprocating sliding against Si₃N₄ balls. *Key Engineering Materials*. 2014, Vol. 604, 126 - 129
- Publication III. Bogatov, A., Viljus, M., Raadik, T., Hantschel, T., Podgursky, V. Nanocrystalline diamond films deformation observed during sliding tests against Si₃N₄ balls. *Accepted for publication in Materials Science (Medžiagotyra)*
- Publication IV. Podgursky, V., Bogatov, A., Freund, M., Kulu, P. Influence of surface morphology on the tribological behavior of diamond-like carbon coating. *Key Engineering Materials*. 2013, Vol. 527, 83 - 91

Author's contribution:

Publication I: testing, data analysis

Publication II: testing, measurements of surface roughness, profilometric measurements, AFM scanning, writing, data analysis

Publication III: testing, measurements of surface roughness, profilometric measurements, AFM scanning, writing, data analysis

Publication IV: testing, measurements of surface roughness, profilometric measurements, data analysis

INTRODUCTION

Carbon in the form of diamond and graphite is known to the humankind since ancient times. Nowadays the carbon-based technology has an enormous range of applications, including manufacturing of components for the automotive and aerospace industry, electronic devices, abrasives. Wear-resistant carbon films are used in the manufacture of high-performance cutting tools, scratch-resistant optical lenses, highly loaded engine parts like camshafts or valves. It is possible to use the coating technology for the production of microelectromechanical systems (MEMS) and atomic force microscopy (AFM) tips.

Activities related to the design and manufacturing of hard coatings in Estonia date back to the beginning of the 1980s when the TiN films were obtained using the cathodic arc deposition method. Presently, modern metal- and carbon-based hard films can be prepared in Department of Materials Engineering of Tallinn University of Technology (TUT). Development of new coatings suitable for industrial applications and research in the field of carbon-based films are the parts of ongoing work.

The surface morphology plays an important role in the tribological behavior of materials, especially during the run-in period [1, 2]. Wear of polycrystalline diamond and amorphous diamond-like films is affected by such factors like surface and counterbody asperities interlocking followed with material fracture, micro-ploughing, self-polishing of the film surface and formation of the transfer layer [3, 4, 5, 6].

The aim of the current study is to investigate the tribological behavior of diamond and DLC films in sliding tests against hard ceramic materials: measurements of the coefficient of friction, wear rate and investigation of surface morphology changes under variable test parameters.

The following research activities were conducted:

1. Reciprocating sliding tests of diamond and DLC films against various counter-body ceramic materials.
2. Characterization of clean and worn surfaces of the samples.
3. Investigation of tribological properties (wear rates, coefficients of friction) of the films.
4. Development of models describing evolution of morphology of diamond and DLC films under reciprocating sliding conditions.

Scientific novelty of the current work is as follows:

- Rippling phenomenon occurring during reciprocating sliding tests on NCD and DLC films against ceramic balls was investigated and possible mechanisms of ripple patterns formation were proposed.

- Deformation of polycrystalline diamond film on silicon substrate was observed under relatively low load and possible causes were suggested.

The results of the study have been published in one journal and two proceedings; one journal article has been accepted for publication. The results were presented at two international conferences (Baltmattrib 2013, Riga, Latvia, and Materials Engineering 2014, Kaunas, Lithuania)

ABBREVIATIONS

a-C – Amorphous Carbon
a-C:H – Amorphous Hydrogenated Carbon
ACCVD – Alcohol Cathalytic Chemical Vapor Deposition
AFM – Atomic Force Microscope
BSE – Backscattered Electrons
CF – Carbon Fibers
CNF – Carbon Nanofibers
CNT – Carbon Nanotubes
COF – Coefficient Of Friction
CVD – Chemical Vapor Deposition
DLC – Diamond-Like Carbon
DoSi – Diamond on Silicon
FCC – Face Centered Cubic
HFCVD – Hot Filament Chemical Vapor Deposition
HPHT – High Pressure High Temperature
MCD – Microcrystalline Diamond
Me-C:H – Metal-doped Hydrogenated Carbon
MEMS – Microelectromechanical Systems
MWCNT – Multi-Walled Carbon Nanotubes
MWPCVD – Microwave Plasma Chemical Vapour Deposition
NCD – Nanocrystalline Diamond
PAN – Polyacrylonitrile
PCD – Polycrystalline Diamond
PECVD – Plasma Enchased Chemical Vapor Deposition
PLD – Pulsed Laser Deposition
PTFE – Polytetrafluoroethylene
RMS – Root Mean Squared
SCD – Single-Crystalline Diamond
SE – Secondary Electrons
SEM – Scanning Electron Microscopy
SWCNT – Single-Walled Carbon Nanotubes
t-PA – Trans-Polyacetylene
ta-C – Tetrahedral Amorphous Carbon
ta-C:H – Tetrahedral Amorphous Hydrogenated Carbon
TEM – Transmission Electron Microscopy
UHMWPE – Ultra-High Molecular Weight Polyethylene
UNCD – Ultrananocrystalline Diamond

1 REVIEW OF LITERATURE

Allotropes of carbon have an enormous range of applications. High hardness, low COF and chemical inertness, unique electronic and optical properties, high thermal conductivity make these materials attractive for use in mechanical engineering, optics, electronics, information technology, biology, *etc.*

1.1 Classification of carbon-based materials

Diamond and graphite are well-known allotropes of carbon, other types include glossy carbon, DLC, fullerenes, CNT, *etc.* Carbon is the 6th element in the periodic table, and has 6 electrons located on the two electronic shells with the principal quantum numbers $n = 1$ and 2. Two paired s-electrons are on the shell with $n = 1$, and 4 electrons on the shell with $n = 2$. Those 4 electrons fully occupy the s-orbital (orbital quantum number $l = 0$, corresponding s-shell) with 2 electrons, and 2 unpaired electrons occupy the p-orbital ($l = 1$ corresponding p-shell).

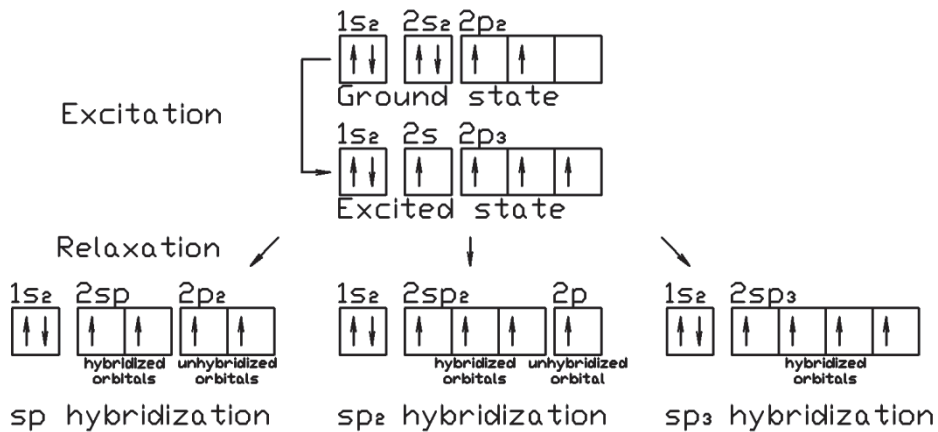


Figure 1.1 Hybridization of carbon [7].

The hybridization process is shown in Figure 1.1. When an s-electron from the valence shell excites, it goes to the unoccupied place in the p-orbital. This process is followed immediately with relaxation when the remaining s-electron and 1, 2 or all 3 p-electrons transit to an intermediate sp state. After the relaxation of the excited state carbon atom can have one of the three (sp , sp^2 or sp^3) hybridizations. In the sp hybridization state there are 2 hybridized sp -electrons and 2 non-hybridized p-electrons in the valence shell. In the sp^2 hybridization state the valence shell has 3 sp electrons and 1 non-hybridized p-electron and there are 4 sp -electrons in the sp^3 hybridization state.

Carbon allotropes can be classified based on their hybridization state: sp , sp^2 or sp^3 .

1.1.1 Allotropes of carbon

Sp form of carbon

Crystalline form of carbon with sp hybridization is a chain of atoms bounded together with alternating single and triple bonds $-C\equiv C-C\equiv C-$ in the case of α -carbyne, or double bonds $=C=C=C=C=$ for β -carbyne. A synthesis of carbyne was first announced in the early 1960s last century in the USSR, however still there is no unambiguous experimental evidence supporting that achievement.

Calculations carried out by Liu *et al.* [8] and Itzhaki *et al.* [9] showed that Young's modulus of carbyne can be about 33 - 47 TPa, *i.e.* in 30-50 times higher than diamond value.

Sp² form of carbon

A number of sp² carbon allotropes exist. The basic structural element of sp² form of carbon is graphene, *i.e.*, a sheet of carbon atoms arranged in a two-dimensional hexagonal crystal lattice. Carbon sp² allotropes are formed by stacking graphene sheets (graphite, glassy carbon, *etc.*) or rolling them (fullerenes, nanotubes, nanofibers).

The discovery and investigation of graphene by Geim and Novoselov in 2004 [10] was awarded with the Nobel Prize in Physics in 2010. The syntheses of fullerenes was reported at the end of the 20th century. The discovery by Kroto *et al.* [11, 12] was awarded with the Nobel Prize in Chemistry in 1996.

Table 1.1 Graphene properties [13, 14, 15].

Property	Unit	Value
Young's modulus	GPa	1000
Fracture strength	GPa	130
Carrier mobility	cm ² /V·s	15000
Thermal conductivity	W/m·K	4840 – 5300

Due to its 2D structure, graphene possesses remarkable properties, distinguishing it from bulk graphite. It has very high mechanical strength, high carrier mobility and thermal conductivity. As different from common semiconductors, the carrier mobility in graphene does not change substantially with temperature. Stacking together two or more layers gives materials with properties different from both single-layer graphene and bulk graphite. An example can be a possibility of electronically tunable bandgap in double-layer graphene [16].

Table 1.2 Crystalline sp^2 carbon materials formed by stacking graphene sheets.

Property	Unit	Graphite [17, 18]	Glassy carbon [19]
Density	g/cm^3	2.26	1.3 – 1.55
Crystal system		Hexagonal	-
Lattice constant	nm	$a = 0.246, c = 0.671$	-
Young's modulus	GPa	1060 (in (001) plane), 36 (normal to (001) plane)	14 – 18
Hardness	GPa		2 – 3
Thermal conductivity (300 K)	$\text{W/m}\cdot\text{K}$	140 – 500 (in (001) plane), 3 – 10 (normal to (001) plane)	
Band gap	eV	0.04	0.01

Graphite is a bulk counterpart of graphene. Due to its crystal structure, graphite exhibits high anisotropy in properties. The elastic modulus of graphite (in-plane) is comparable to diamond and 30 times higher than the modulus in normal direction to the graphene layer (see Table 1.2).

Glassy carbon has an irregular structure comprised of graphene sheets. It was shown by Harris *et al.* [20] that high chemical and thermal inertness of glassy carbon can be explained by its fullerene-like structure.

Fullerenes are molecules composed of carbon atoms forming a hollow sphere or tube. Spherical fullerenes are called buckyballs. Fullerenes may form molecular crystals named fullerite. Carbon spheres in fullerite crystal are bonded by van der Waals forces between each other, therefore their mechanical properties are rather low. Young's modulus of C_{60} fullerite is only 15.9 GPa [21], thermal conductivity is 0.4 $\text{W/m}\cdot\text{K}$ [22], hardness 125 – 165 MPa that increases up to 1 GPa after low frequency laser irradiation [23, 24]. The density of fullerite is 1.7 g/cm^3 [25]. There have been reports about synthesis of an ultrahard form of fullerite surpassing diamond in hardness (290 – 310 GPa against 167 GPa) by applying pressures of 6 – 18 GPa [26, 27].

Carbon nanotubes (CNT) are cylindrical fullerene molecules that can be represented as rolled graphene sheets with diameter in the range of 0.6 – 3 nm [28, 29]. CNT can be single- and multi-walled (SWCNT and MWCNT). Tensile strength of CNT is about 100 times stronger than the strength of steel (see Table 1.3). Young's modulus is about 1000 GPa, which is similar to diamond. Elongation range is 5 – 20 %.

CNT are essentially free of lattice defects, which provides exceptional strength of the material. SWCNT are stronger than steel, while the electrical conductivity is comparable to that of copper, with the maximal current density more than 10^9 A/cm^2 at room temperature. They also have a high thermal conductivity (2000 $\text{W/m}\cdot\text{K}$ at room temperature) [33]. However, in spite of their excellent mechanical properties, SWCNT are not in wide use, because it is difficult to produce nanotubes with a length of more than a few μm . Poor adhesion to matrix materials remains a challenge. A variety of methods, such as

arc discharge, laser ablation and chemical vapour deposition (CVD) have been developed for the production of CNT in industrial-scale quantities.

Table 1.3 Crystalline sp^2 carbon materials formed by rolling of grapheme sheets, as well as carbon fibers and steel for comparison purposes. Properties of carbon nanotubes, carbon fibers/nanofibers and stainless steel [17, 29, 30, 31, 34, 35].

Material	Density, g/cm³	Tensile strength, GPa	Young's modulus, GPa
SWCNT	1.3 – 1.4	50.0 – 500.0	900 – 1700
MWCNT	1.8 – 2.6	6.2 – 63.0	270 – 1870
CF	1.6 – 2.2	1.4 – 5.5	159 – 965
CNF	2.0	2.9 – 4.0	240 – 300
AISI 304 steel	7.9	0.6	200

It is important to distinguish between carbon nanotubes and carbon fibers (CF). CF is defined as a fiber containing not less than 90 % of carbon, made by controlled pyrolysis and heat treatment. Most of the CF prepared from polyacrylonitrile (PAN). CF have diameters ranging from a few hundreds to thousands of nanometers, and can be up to several mm in length. Tensile strength of CF is an order of magnitude smaller than that of the CNT. CF do not react with water or common solvents, acids, *etc.* at room temperature and retain their properties at high temperatures. Although these mechanical properties are not as excellent as those of CNT, CF are relatively light and inexpensive to manufacture. One of the application areas where the mechanical properties of carbon fibers are of great importance is manufacturing of composites. The CF with relatively low density are attractive for low-weight applications. In fact, CF is the most common material used in the polymer composites as an armature material. Parts made from CF are five times stronger than their steel equivalents, but five times lighter. Applications include airspace, automotive and sports equipment industries.

Currently there is no specific classification of carbon nanofibers (CNF). CNF internal structure is composed of graphene cones stacked into each other. Thus, CNT are actually CNF with graphene cones reduced to cylindrical shape. CNF can be prepared by a number of methods including arc discharge, laser ablation and various types of CVD. One of the most promising methods is Alcohol Catalytic CVD (ACCVD) due to relatively low temperatures (600 – 700 °C), high purity of obtained CNF and low cost [32]. CNF grown from the gas phase are thicker than CNT with the diameter of about 50 – 200 nm and a length up to 200 μm [36, 37].

Finally, different amorphous forms of carbon with mainly sp^2 hybridization exist. Amorphous form represents an assortment of carbon atoms in a non-crystalline, irregular state. This form is essentially graphitic but atoms are not held in a crystalline macrostructure. Carbon in amorphous form is black

powder, and it is the main constituent of such substances as charcoal, lampblack (soot) and activated carbon.

Sp³ form of carbon

The name of the well-known gemstone *diamond* is derived from the ancient Greek *αδάμας (adámas)*, "proper", "unalterable", "unbreakable, untamed" [38]. Among other main characteristics of the gem diamond, known as four C-s (carat, cut, color and clarity), color is the most important one. Carbon atoms in diamond are bound with short and strong covalent bonds, therefore only a few elements with atom radii close to those of carbon are capable of being incorporated into diamond lattice. The most common impurities are nitrogen and boron, therefore diamonds can be classified into two groups (I and II) and subgroups depending on nitrogen (yellow diamond) and boron (blue diamond) content in the crystal lattice, see Table 3. Type IIa diamond can be pink, red, or brown, due to the presence of structural defects such as dislocations, vacancies and twins. Pure diamonds are transparent and colorless.

Table 1.4 Classification of types of diamond [39].

Type	Structure
IaA	Aggregated N pairs
IaB	N aggregates + vacancies
Ib	Isolated N atoms
IIa	No impurities (only lattice defects)
IIb	B impurities

The properties of diamond (natural or synthetic) depend strongly on material purity and presence of lattice defects. Impurity atoms can be either isolated in the crystal lattice or compose aggregates between themselves and vacancies. Such lattice defects are called color centers. Diamond is an ultrahard material with unique combinations of properties including high mechanical strength and thermal conductivity, outstanding optical and electronic properties, exceptional chemical inertness. The potential utilities of diamond are enormous: it is used in mechanical engineering, electronics, optics, information technology, biology, *etc.* Most important properties and applications of undoped diamond are listed in Table 1.5.

Table 1.5 Properties and applications of Type II diamond at room temperature [40, 41, 42].

Property	Unit	Value	Application
Density	g/cm ³	3.52	
Knoop hardness, {110} plane, direction [001]	GPa	113	Tools, surgery blades
Young's modulus, direction [100]	GPa	1053	
Bulk modulus	GPa	442	
Shear modulus, direction [100]	GPa	574	
Anisotropic ratio		1.21	
Poisson ratio		0.1	
Band gap	eV	5.4	High-temperature electronics
Carrier mobility	cm ² /V·s	1600 h 2200 e	Radiation-hard detectors Optoelectronic switches
Resistivity	Ω·cm	10 ¹³ – 10 ¹⁵	Optical (electron) switches
Thermal conductivity at 20 °C	W/m·K	2600 – 3200	Heat spreaders, windows for power lasers, computer chips
Dielectric constant		5.7	
Loss tangent at 170 GHz		0.3·10 ⁻⁶	Windows for gyrotrons, klystrons
Optical transmission range	nm	220 – 2500, > 6000	Optics for lasers (mostly IR)
Debye temperature	K	1200	Stable NV ⁻ color centers, quantum computers
Acoustic wave velocity	km/s	18.4 along direction [111]	Surface acoustic wave devices
Thermal expansion coefficient	10 ⁻⁶ K ⁻¹	0.8	Stable-dimension components, computer chips
Corrosion resistance			Electrochemistry (doped diamond)
Low or negative electron affinity			Field electron emitters
Biocompatibility			Coatings on implants, detectors for blind people

Bulk single-crystal diamond demonstrates a certain anisotropy of its mechanical, tribological, optical and electrical properties. Mechanical properties of diamond including Young's modulus, Poisson ratio, *etc.* can be calculated using elastic constants (C_{11} , C_{12} and C_{44}) that can be found from direct measurements. See more detailed discussion on the anisotropy of diamond and its impact on mechanical and tribological properties (section 1.3).

Nanodiamond

Diamond exhibits a certain size effect in mechanical tests. Indentation on diamond octahedral plane using diamond indenters with radii of 0.5 – 0.005 mm can increase strength values from 16.66 to 63.96 GPa [43]. Loading diamond grit particles shows a steady increase of failure load with a decrease of particle size (from 300 MPa for 1 mm grit to 900 MPa for 0.3 mm grit) [44].

Nanodiamond is a type of carbon allotropy. Particles of about 2 – 10 nm in size can be prepared by the detonation of the TNT/hexogen mixture in a rugged chamber. The process was developed in the 1960s in the USSR [45]. The core of the nanodiamond particle possesses a diamond structure, however the structure of the nanodiamond surface is a more controversial issue. A fullerene-like surface reconstruction was found for particles with the size of 2 – 4 nm prepared in hydrogen-free conditions. Such nanodiamonds with hybrid structure (sp^3 core and sp^2 surface) are called bucky-diamonds [46].

Nanodiamond particles were applied in tribology as lubricant additives and composite fillers, and in medicine where surface-activated particles can be used for drug delivery [47, 48].

Hexagonal diamond

Hexagonal diamond or lonsdaleite is a carbon allotrope with a hexagonal lattice. Initially it was found in meteorites and synthesized from graphite in 1967 [49]. Lonsdaleite can be obtained also from cubic diamond by means of high pressures and temperatures [50]. Up to now it remains a challenge to produce large-size good quality samples of this material. Computer simulations predict 58% higher indentation hardness of lonsdaleite compared to diamond [51].

1.1.2 Diamond and DLC films

Regarding to the classification of carbon allotropes presented in section 1.1.1, diamond and DLC films can be considered as the sp^3 form of carbon in the case of monocrystalline diamond films and a mixture of sp^2 and sp^3 species in the case of other types of diamond and DLC films. Diamond and DLC films are resistant to wear and exhibit high hardness, low coefficient of friction and chemical inertness under normal conditions (in the air at moderate temperatures and speeds).

Table 1.6 Classification of diamond films [52].

Property	MCD	NCD	UNCD
Crystallinity	Columnar	Mixed diamond and non-diamond	Equiaxed diamond
Grain size	0.5 – 10 μm	50 – 100 nm	2 – 5 nm
Surface roughness	0.4 – 1 μm	50 – 100 nm	20 – 40 nm
Electronic bonding	sp^3	sp^3 + up to 50 % sp^2	sp^3 + 2 – 5 % sp^2

Diamond films can be classified into single-crystal diamond (SCD) and polycrystalline diamond (PCD). Depending on their crystal size, polycrystalline forms are divided into microcrystalline diamond (MCD), nanocrystalline diamond (NCD) and ultra-nanocrystalline diamond (UNCD). Grains size is one of the most important characteristics of diamond films. The majority of MCD films consists of columnar grains and thus demonstrates considerable anisotropy of properties in different directions. NCD and UNCD films consist of smaller randomly oriented crystals. The NCD films were investigated in the present study.

Grain size exerts significant influence on film surface roughness and mechanical properties. MCD films with rough surface are hard to use in rubbing parts due to severe wear of the mating surface. At the same time polishing of diamond surface is a difficult, expensive and tedious process. However, surface roughness can be substantially decreased by using NCD and UNCD films with grain size of 5 – 10 nm and roughness up to RMS 10 – 20 nm. As shown by Field *et al.* [53], films with smaller crystallite size have higher hardness and Young's modulus.

Various CVD methods are used to synthesize polycrystalline diamond films which require high temperatures (up to 1000 °C). CVD deposition methods are discussed in more detail in section 2.1. Versatility of diamond film structures and ability to prepare films with well-textured surface, to tailor the properties by doping with different elements (N, B, Si, *etc.*) allow to meet particular application objectives and to deliver different functionalities (mechanical, electrical, optical, *etc.*) [54, 55, 56, 57]

Diamond films can be deposited to the surface of cutting tools made from tungsten carbide and other materials. The diamond coating provides improved productivity in cutting of nonferrous metals, graphite, plastics, composite materials and wood. Diamond films can be applied to shaft seals in pumps, which considerably decreases wear in slurries pumping. Currently MEMS are produced usually from silicon by etching. However, silicon has unsatisfactory mechanical and tribological properties that limit its use in the conditions of high speeds and loads. A possible solution to this problem could be application of thin diamond films as a protective layer.

Table 1.7 Types and properties of DLC films [59, 60, 61].

Type	Density, g/cm ³	Hardness, GPa	sp ³ content, %	H content, %	Band gap, eV
Me-C:H (Ti, W)		20	35	10 – 20	
a-C, evap	1.9 – 2.0	2 – 5	1	-	0.4 – 0.7
a-C, sputt.	1.9 – 2.4	11 – 15	2 – 5	-	0.4 – 0.7
a-C:H, hard	1.6 – 2.2	10 – 25	30 – 60	10 – 40	0.8 – 1.7
a-C:H, soft	0.9 – 1.6	<5	50 – 80	40 – 65	1.6 – 4
ta-C	3.0	55 – 65	~100	<1	

Unlike diamond films, diamond-like carbon (DLC) films have amorphous structure. DLC is a mixture of sp³ and sp² carbon structures. There are four main types of DLC films (a-C, ta-C, a-C:H and Me-C:H). The structure and properties of a particular DLC film type might vary substantially and depend also on the deposition methods (see Table 1.7). Me-C:H type of DLC was investigated in the present study.

Depending on the deposition method and conditions films can be either diamond- or graphite-like. Structurally DLC consists of sp³ (diamond or tetrahedral, ta-C) and sp² (graphitic, a-C) phases. Depending on the carbon source (methane, acetylene, ethylene, *etc.*), it can include a considerable amount of hydrogen (a-C:H and ta-C:H films). Films obtained using solid sources of carbon contain virtually no hydrogen.

The coefficient of friction (COF) of DLC decreases with an increase of the hydrogen content. At the same time, the decrease of COF correlates with the improvement of film wear resistance. COF depends also on atmospheric humidity.

Incorporation of dopants (silicon, oxygen, fluorine, nitrogen, and boron) allows to substantially modify the wetting behavior of DLC without essential losses in the tribological properties. Thus, the surface energy of DLC can be decreased by the addition of fluorine, silicon or oxygen. Doping with boron and nitrogen leads, on the contrary, to the surface energy increase [58].

DLC films can be deposited on the metallic and ceramic substrates using PECVD, ion plating, laser ablation *etc.* Carbon-containing gases (C_nH_m) and hydrogen are used to produce gas-discharge plasma used in the CVD process.

DLC possesses smoother surface in contrast to diamond films. DLC films are used in various applications such as tooling, ball bearings, sliding bearings and aluminium extrusion. In addition, DLC films have been successfully used in car engines (coatings for moving parts and fuel injection systems of diesel engines) and in hard disk drives.

1.2 CVD diamond growth mechanisms

In the CVD process, the chemical composition of species precipitating from the gas phase is different from the composition of the crystal, thus growth is provided with chemical reactions taking place on the surface. Diamond crystal growth is a relatively complicated multistage process. The free hydrogen atoms (H) and radicals (CH_3 – methyl radical) play a key role in the growth process, as shown in Figure 1.2, Figure 1.3 and Table 1.8. During the growth the surface of diamond is almost completely passivated with hydrogen atoms (see Figure 1.3), which limits the possibility of attaching hydrocarbon molecules and blocks their migration on the surface after attaching.

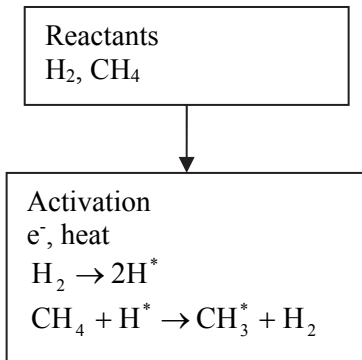


Figure 1.2 Precursor gases H_2 and CH_4 are flushed into the chamber. Due to plasma activation H^* and CH_3^* species are formed.

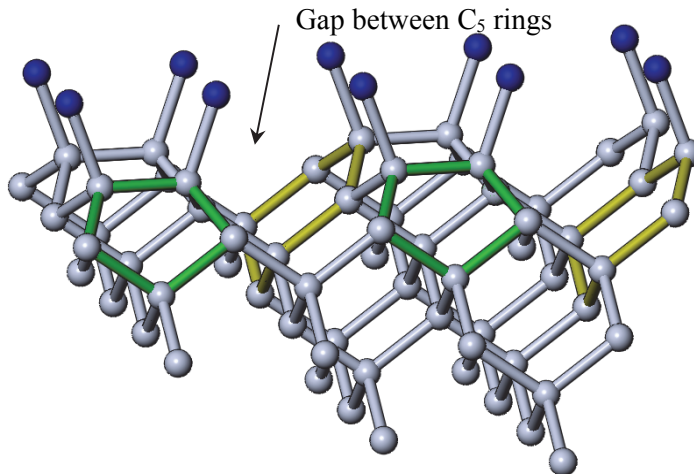


Figure 1.3 Diamond (100) surface passivated with H atoms (denoted by blue balls). Examples of C_5 rings are indicated with green and those of C_6 rings – with yellow.

Molecular mechanics calculations [62] have shown that a surface with every carbon atom bonded with one hydrogen atom and dimer bonds between pairs of surface carbon atoms is thermodynamically the most stable under typical CVD growth conditions. So as shown in Figure 1.3, (100) surface represents rows of carbon atoms pairs incorporated into five-membered rings (C_5) divided by gaps. Two mechanisms are needed for crystal growth: addition of a carbon atom into C_5 ring to form a C_6 ring and in a gap between two adjacent rings. A detailed description of the process is given by Harris and Goodwin [63]. Main reactions are shown in Table 1.8.

Table 1.8 The growth process of diamond (100) surface.

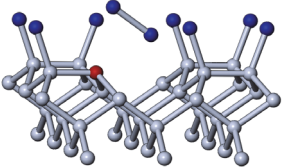
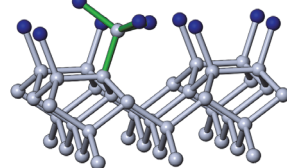
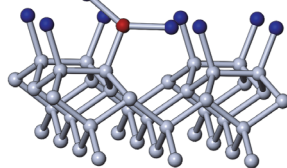
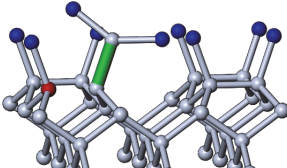
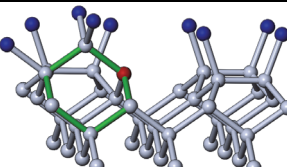
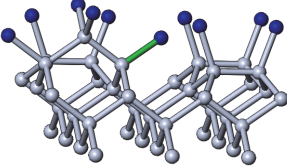
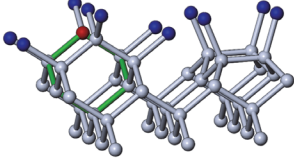
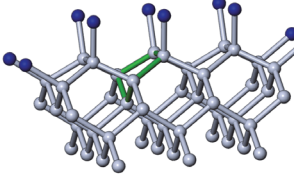
	<p>1. $C_5 + H^* \rightleftharpoons C_5^* + H_2$ H^+ ion recombines with a hydrogen atom on the surface leaving a radical site</p>
	<p>2. $C_5^* + CH_3^* \rightarrow C_5 - CH_3$ CH_3 radical attaches to the surface. The structure $C_5 - CH_3$ is formed</p>
	<p>3. $C_5 - CH_3 + H^* \rightarrow C_5 - CH_2^* + H_2$ One H atom is removed from CH_3 radical</p>
	<p>4. $C_5 - CH_2^* \rightleftharpoons C_5^* + CH_2$ Rearranging of C-C bonds with formation of double bond (β-scission)</p>
	<p>5. $C_5^* + CH_2^* \rightleftharpoons C_6^* - H$ Formation of C_6 ring</p>
	<p>6. $C_6^* - H + H^* \rightarrow C_6 - H$ Passivation of C_6 ring with H</p>

Table 1.8 (continued)

	<p>7. $C_6 - H + H^* \Leftrightarrow C_6^* + H_2$</p> <p>Formation of a radical site on a C_6 ring. Before this reaction, a second C_6 ring (green) was formed behind the first one by the same sequence 1 – 6.</p>
	<p>Filling the gap between the former rows of C_5 rings by 4 reactions (not shown), with following joining of C_6 rings by reactions 7 and 8.</p> <p>7. $C_6 - H + H^* \Leftrightarrow C_6^* + H_2$</p> <p>8. $C_6^* + C_6 - H + H^* \rightarrow C_6 - C_6 + H_2$</p> <p>As the result addition of the next layer of carbon atoms occurs, the structure consisting from parallel rows of C_5 rings (highlighted with green) remains intact but rotated 90°.</p>

1.3 Mechanical and tribological properties of diamond and DLC films

1.3.1 Anisotropy of mechanical properties of diamond

Diamond lattice represents two FCC Bravais lattices shifted to $\frac{1}{4}$ of the main diagonal. All carbon atoms in diamond are in the sp^3 hybridization state. Diamond demonstrates certain anisotropy of its properties depending on the crystallographic plane and the direction. Understanding of anisotropy of diamond is important for understanding wear on diamond as well as diamond films. For instance, Young's modulus depends on the surface orientation and also on the direction on a particular surface. The Knoop hardness test depends on the diamond surface and the direction on the surface. For instance, for the synthetic type of IIa diamond, hardness increases with the direction rotating from $[100]$ to $[110]$ on (100) surface [64]. Tribological properties also depend on the direction.

The general form of Hooke's Law or the strain-stress relation in the material is described with the following equations [65]:

$$\sigma_{ij} = C_{ijkl} \varepsilon_{kl} \quad (1.1)$$

$$\varepsilon_{ij} = S_{ijkl} \sigma_{kl} \quad , \quad (1.2)$$

where

σ and ε – second-rank stress and strain tensors

C and S – fourth-rank compliance and stiffness tensors (in total 81 components, *i.e.* 3^4)

$i, j, k, l = 1, 2, 3$

Due to symmetry of C and S tensors in the first two and last two indexes (e.g. $s_{ijkl} = s_{ijlk}$ and $s_{ijkl} = s_{jilk}$) from 81 components only 36 components are independent. It allows changing tensor notation to matrix notation according to the following scheme [66]:

tensor notation	11	22	33	23, 32	31, 13	12, 21
matrix notation	1	2	3	4	5	6

At the same time the following changes must be introduced:

$$\begin{aligned}
 s_{ijkl} &= s_{mn} \text{ when } m \text{ and } n \text{ are } 1, 2, 3 \\
 2s_{ijkl} &= s_{mn} \text{ when either } m \text{ or } n \text{ is } 4, 5 \text{ or } 6 \\
 4s_{ijkl} &= s_{mn} \text{ when both } m \text{ and } n \text{ is } 4, 5 \text{ or } 6
 \end{aligned}$$

Therefore Hooke's Law can be rewritten:

$$\sigma_i = C_{ij} \varepsilon_j \quad (1.3)$$

$$\varepsilon_i = S_{ij} \sigma_j, \quad (1.4)$$

where $i, j = 1, 2, 3, 4, 5, 6$

Due to symmetry of the crystal structures from 36 elastic constants only 21 are independent. In the case of a cubic crystal structure, there are three independent elastic constants (C_{11} , C_{12} and C_{44} , or S_{11} , S_{12} and S_{44}) and the matrixes C_{ij} and S_{ij} are as follows:

$$C_{ij} = \begin{pmatrix} C_{11} & C_{12} & C_{12} & 0 & 0 & 0 \\ C_{12} & C_{11} & C_{12} & 0 & 0 & 0 \\ C_{12} & C_{12} & C_{11} & 0 & 0 & 0 \\ 0 & 0 & 0 & C_{44} & 0 & 0 \\ 0 & 0 & 0 & 0 & C_{44} & 0 \\ 0 & 0 & 0 & 0 & 0 & C_{44} \end{pmatrix} \quad (1.5)$$

$$S_{ij} = \begin{pmatrix} S_{11} & S_{12} & S_{12} & 0 & 0 & 0 \\ S_{12} & S_{11} & S_{12} & 0 & 0 & 0 \\ S_{12} & S_{12} & S_{11} & 0 & 0 & 0 \\ 0 & 0 & 0 & S_{44} & 0 & 0 \\ 0 & 0 & 0 & 0 & S_{44} & 0 \\ 0 & 0 & 0 & 0 & 0 & S_{44} \end{pmatrix} \quad (1.6)$$

Material constants for cubic crystals can be found from the following relations. Young's modulus E in the arbitrary directions h, k, l :

$$\frac{1}{E_{hkl}} = S_{11} - 2(S_{11} - S_{12} - \frac{S_{44}}{2})(\varphi_1^2 \varphi_2^2 + \varphi_2^2 \varphi_3^2 + \varphi_1^2 \varphi_3^2) \quad (1.7)$$

$\varphi_1 = \cos\alpha_1$, $\varphi_2 = \cos\alpha_2$ and $\varphi_3 = \cos\alpha_3$ – direction cosines (Figure 1.4)

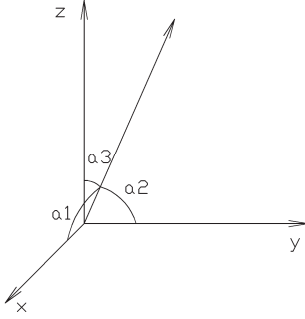


Figure 1.4 Coordinate axes and direction angles.

Shear modulus G in the arbitrary directions h, k, l :

$$\frac{1}{G_{hkl}} = S_{44} - 4(S_{11} - S_{12} - \frac{S_{44}}{2})(\varphi_1^2 \varphi_2^2 + \varphi_2^2 \varphi_3^2 + \varphi_1^2 \varphi_3^2) \quad (1.8)$$

Bulk modulus B :

$$B = \frac{C_{11} + 2C_{12}}{3} \quad (1.9)$$

Poisson ratio ν :

$$\nu_{21} = \frac{C_{12}}{C_{11} + C_{12}} \quad (1.10)$$

In practice, the polycrystalline materials are mainly used and their mechanical properties can be calculated by the following relations [67]:

$$G = \frac{3C_{44} + C_{11} - C_{12}}{5} \quad (1.11)$$

$$E = \frac{9BG}{3B + G} \quad (1.12)$$

$$\nu = \frac{1}{2} \left(1 - \frac{E}{3B} \right) \quad (1.13)$$

In Table 1.9 the elastic moduli of diamond and graphite (for comparison purposes) are presented. Graphite has hexagonal lattice and therefore 5 independent elastic constants.

Table 1.9 Elastic moduli of diamond and graphite [68, 69].

Modulus	Value, GPa	
	Diamond	Graphite
C_{11}	1076.4	1060.0
C_{12}	125.2	180.0
C_{13}	-	15.0
C_{33}	-	36.5
C_{44}	574.4	4.0

1.3.2 Wear of diamond and DLC films

Historically, diamond polishing (polishing of a diamond single crystal) invented in ancient times (4th century BC) is used unchanged so far. However only recently, the mechanisms of the polishing process were revealed experimentally and proved by theoretical calculations. The friction resulting from a contact sliding can be described by two major components: mechanical ploughing and physical/chemical attraction or adhesion. Friction and wear depend on intrinsic factors (surface roughness, hydrogen and impurities concentration, *etc.*) and extrinsic factors (test conditions and counter body materials). Explanation of tribological properties of CVD diamond films is more complicated. In most cases diamond films consist of micro- or nanosized diamond crystals with either random or uniform orientation.

Anisotropy of diamond polishing

Diamond gemstone polishing is usually carried out on the diamond grids embedded in rotating cast iron wheel called “scaife”, see Figure 1.5. The wear behavior of a single crystal diamond depends on the polishing direction, *i.e.* the wear is anisotropic. “Soft” directions correspond to directions with higher wear, and “hard” directions to ones with minor wear. When polishing in “soft” directions, high heat, low vibration and low-frequency noise are observed. Correspondingly, there is a grating sound, little emitted heat and much vibration in “hard” directions [70]. Amorphous sp^2 form of carbon was found on the wear scars after sliding along “soft” directions, however debris produced after sliding in “hard” directions was identified as sp^3 form of carbon particles, indicating fracture of diamond [71].

A model of diamond polishing as a three-body wear process (fracture-based mechanism) is discussed by Tolkowsky [72]. However, this mechanism can explain diamond polishing only in “hard” directions. Emergence of nanosized grooves shown in Figure 1.5b cannot be related to scratching by small particles of diamond due to the three-body wear mechanism, such grooves appear already after one stroke of sliding [73]. In addition, the cleavage of asperities on the

diamond surface due to fracture toughness anisotropy of diamond was observed only in the tests where counterbodies were made of hard materials.

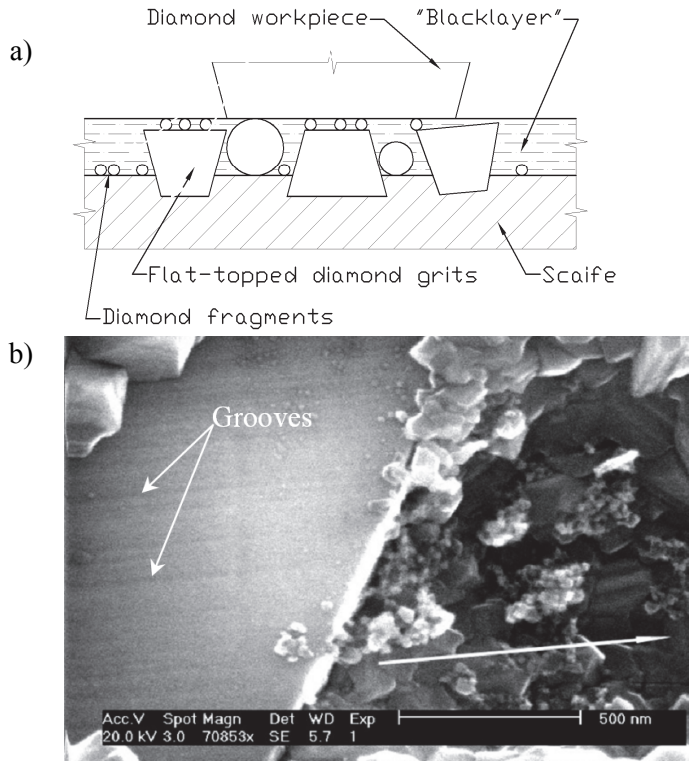


Figure 1.5 Diamond polishing process (a) and nano-sized grooves on a grit particle on the scaife surface (b). White arrow in (b) shows the sliding direction, darker area corresponds to the 'black layer' in (a). Adopted from [74].

The anisotropy of diamond polishing can be described using a model developed by van Bouwelen [73]. In his model a concept of a periodic bond chain vector (PBC) is used. A periodic bond chain is defined as an uninterrupted chain of bounded growth units connecting two translation-equivalent lattice positions in the crystal. As mentioned above, diamond possesses a cubic structure with two FCC structures shifted to the vector $\frac{1}{4}, \frac{1}{4}, \frac{1}{4}$. In the case of diamond such zigzag chain, for instance, interconnects atoms in positions $(0, 0, 0), (\frac{1}{4}, \frac{1}{4}, \frac{1}{4}), (\frac{1}{2}, \frac{1}{2}, 0), \dots$. The direction of such a path is indicated by a PBC vector (Figure 1.6)

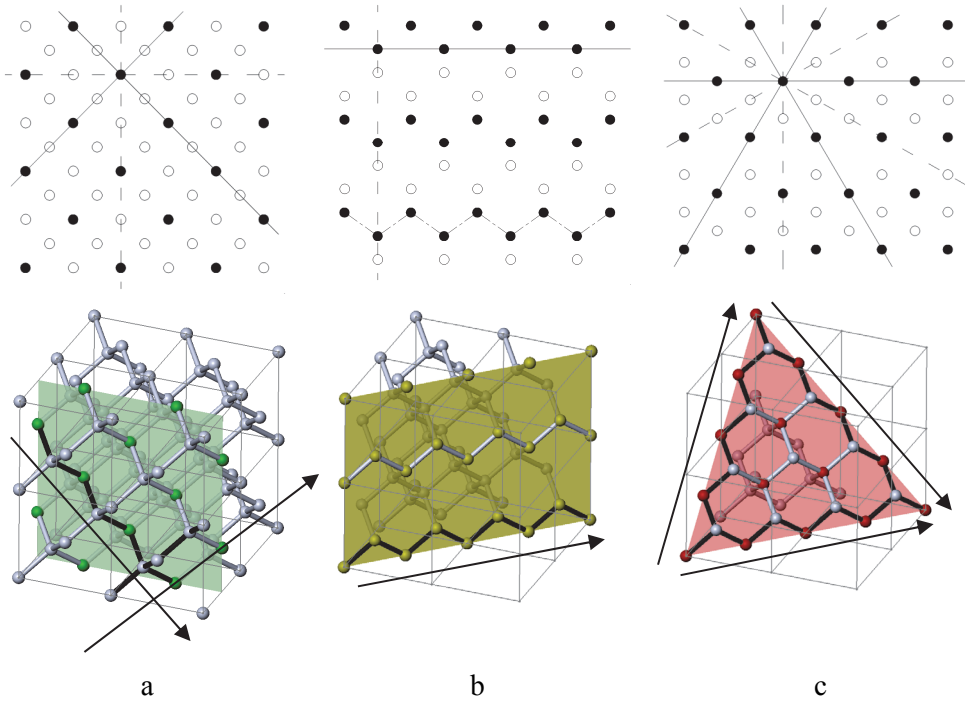


Figure 1.6 Diamond lattice crystallographic planes $\{100\}$ (a), $\{110\}$ (b) and $\{111\}$ (c) (upper row) and their representation in 3D (lower row). Solid lines on the plane projections denote “hard” and dashed lines – “soft” polishing directions. PBC vectors are shown by arrows. For convenience, the zigzag chains are highlighted. Colored dots in the lower row denote in-plane atoms. Note that for $\{110\}$ planes zigzag chains, defining the PBC vectors are located within the plane.

According to the van Bouwelen model, the difference in the polishing rates is fully explained in terms of PBC vectors. The fact that polishing is impossible in the direction of a PBC vector can be explained by coincidence of this direction with that of a strongly bonded zigzag C–C–C chain in the lattice. The decrease of the polishing rate for “hard” directions can be explained by considering as a vector product of the applied force direction and the nearest PBC vector direction $C = \mathbf{F} \cdot \mathbf{P}_{nearest}$ (where F and P are the direction of the applied force and the PBC vector). If the product $C \geq 0.9$, the polishing is difficult, in other words the angle between \mathbf{P} and \mathbf{F} vectors is small ($\leq 25^\circ$). For easy polishing the product $C \geq 0.7$, i.e. the angle is relatively large ($\geq 45^\circ$). An example is shown in Figure 1.6b, in this case $C = 1$, corresponding to hard polishing. As can be seen from Figure 1.6, there is 1 PBC vector in $\{110\}$ planes, 2 vectors in $\{100\}$ planes and 3 vectors in $\{111\}$ planes. Consequently, the minimal C in $\{111\}$ planes is higher than in $\{100\}$ and $\{110\}$ planes. For $\{111\}$ planes the product C is always higher than 0.7, therefore $\{111\}$ planes show harder polishing.

The Poisson ratio for diamond depends on the direction in crystal [73]. For the “soft” directions Poisson ratio is relatively high, i.e. diamond shows

relatively high expansion in the directions perpendicular to the direction of compressive stress. Expansion corresponds to the chemical bond bending, it was shown that bond bending is much less energy consuming than bond stretching or compression. Finally, bending of the bond ends up with its rehybridization from sp^3 to sp^2 form. Therefore in the case of sliding in “soft” directions much less work must be done to achieve the aforementioned transformation. For the “hard” directions, Poisson ratio is small because bond expansion proceeds via mainly stretching and compression of bonds that requires considerable energy.

The mechanochemical amorphization mechanisms on the diamond surface during sliding were further developed by Patevka *et al.* [6]. The diamond polishing is a velocity and load driven process. Sliding at the velocity of 30 m/sec under the load of 10 GPa lead to the formation of an amorphous layer on the diamond surface. Authors suggest that so-called pilot a-C atoms move along the diamond surface during sliding, and, depending on the environmental conditions, exert forces on the surface terminating atoms in the diamond crystal. This can result in removing carbon atoms from the diamond lattice and, thus, formation of an amorphous layer.

Environmental conditions

Under ambient air conditions carbon films demonstrate low COF and wear. However, both rise significantly in vacuum and at high temperatures. It is believed that such behavior is caused by the passivation of dangling bonds of carbon atoms on the surface with water molecules, hydrogen and oxygen atoms and carbonaceous species that leads to considerable decrease of adhesion forces.

For ultra smooth and polished diamond films as well as cleaved natural diamonds, the ploughing component of friction is minimal and the friction behavior is then largely controlled by the extent of adhesive interaction across the sliding contact interfaces. When a metal or ceramic is sliding against such a chemically passive surface, very low friction coefficients are observed. If the dangling surface bonds of diamond are reactivated by desorbing surface contaminants from the sliding surfaces, *i.e.*, by thermal excitation or at ultrahigh vacuum, large increases in friction are observed [3].

Diamond grains orientation

The polishing of polycrystalline diamond films is strongly related to the polishing of single crystal diamond described above. Anisotropy of diamond mechanical properties substantially complicates the ability to polish polycrystalline films with random crystals orientation. El-Dasher *et al.* [75] showed that grains oriented in $\{100\}$ and $\{111\}$ planes perpendicular to the surface undergo significantly lower wear than grains with other orientations. It is consistent with the data presented in the previous section of the thesis (Anisotropy of diamond polishing).

Diamond grain size

The typical diamond grain size of polycrystalline diamond films can vary from several nanometers to micrometers. The reduction of grain size means also a significant increase in grain boundary volume. In the UNCD films up to 10 % of carbon atoms can be associated with grain boundaries [76]. Formation of nanocrystalline grain structure is accompanied by an increase of the hydrogen content in the film due to deposition conditions. This leads to a significant change in the mechanical properties of the film, particularly to a decrease of hardness. As shown in [77] and [78], at the same time, a decrease in the wear rate and COF is observed.

Surface roughness

The roughness of films is an important factor, which influences the diamond film wear. Surface asperities of the film interlock with the counterbody surface asperities, which results in material fracture followed by micro-ploughing and self-polishing wear on the diamond film surfaces. Relationship between surface roughness and coefficient of friction was investigated by Bhushan *et al.* [5]. Reciprocating sliding tests were performed with unpolished and polished PCD films with different roughness. Alumina balls were used as a counterbody. The results show a clear correspondence in the increase of the COF value for the run-in period to the increase of the surface roughness.

The polycrystalline diamond films, *i.e.* films with randomly oriented grains can be grown with preferable orientations. Diamond films with [111] growth orientation exhibit high roughness due to the pyramidal shape of single crystals. However, the growth with preferential [100] texture results in the flat top surfaces of crystals and lower roughness. Diamond films with [100] texture show lower COF [79].

Holmberg *et al.* [1] suggested different wear mechanisms acting on surfaces of PCD with different roughness, see Table 1.10.

Table 1.10 Contact modes of PCD surfaces by Holmberg [1].

Roughness $R_a, \mu\text{m}$	COF	Wear rate, mm^3/Nm	Contact mechanisms
0.1 – 1	0.1 – 0.7	$10^{-1} - 10^{-4}$	asperity interlocking, breaking and ploughing
0.01 – 0.1	0.001 – 0.1	$10^{-4} - 10^{-7}$	$\text{sp}^3 \rightarrow \text{sp}^2$ transformation at high local pressure and temperatures followed by shear within graphitic basal planes
0.001 – 0.01	0.03 – 0.15	$10^{-2} - 5 \cdot 10^{-6}$	Shear between layers of H atoms at dangling bonds

Wear of DLC films

There are many factors influencing friction in DLC films [80], including surface roughness, adhesion between counterbodies, tribochemical and third-body interactions, hydrogen content and the sp^3/sp^2 ratio in films, environmental conditions (dry air, N, vacuum) [81], doping (Si, P, N, F) [82, 83], *etc.* The method of deposition is an additional key element influencing the tribological behavior of DLC films. Films obtained by pulsed laser deposition or cathode arc deposition methods commonly have numerous microparticles ejected from the solid carbon source surface and this causes the rise of the COF, especially in the run-in period. Formation of transfer layer on the surface of counterbodies at the steady stage of the tribological test results in sliding between two carbonaceous layers and subsequently corresponds to low friction observed of the DLC films [1].

Rippling

The experiments conducted in the scope of the current thesis revealed ripple patterns after sliding on DLC and NCD films against ceramic counterbodies. Therefore this effect could be reviewed here as well.

Rippling is a very common natural phenomenon where such structures appear due to the motion of gases, liquids and solid particles. Ripple patterns were found at macro-tribological scale as well, like rail corrugation [84].

The formation of periodic ripple patterns on the micro/nano scale has been reported in literature. Shi *et al.* [85] found formation of ripples on the surface of ultra-high molecular weight polyethylene (UHMWPE) during cyclic loading in a sliding test against Ti_6Al_4V . This was explained by the stress-induced preferential orientation of the crystalline lamellae in the UHMWPE and a micro-fatigue wear. Nanoscopic ripple patterns were also found after repeated scratching by an atomic force microscopy (AFM) tip on different materials including polymers [86], ionic crystals and metals [87], and semiconductors [88]. A mathematical model of AFM tip-surface interaction describing formation of the ripple pattern was suggested by Filippov *et al.* [89]. Nanometric-sized ripple patterns can also be produced by focused ion-beam bombardment of targets including semiconductors and single crystal diamond under a range of inclination angles [90, 91].

Ripple patterns were observed on the wear scar surfaces of diamond films rubbed under stick-slip motion against cubic boron nitride (cBN) [92] and diamond [93]. However, no systematic studies of the formation and the nanoscale surface topography of ripples on NCD have been carried out so far.

1.4 Objectives of the thesis

Outstanding properties of diamond and DLC films are important for tribological applications. Therefore understanding of the tribological properties is crucial.

The aim of the present study is to investigate frictional and wear behavior of NCD and DLC films in sliding tests against ceramic materials with high

hardness. A major part of the study deals with the dynamics of morphological changes on the wear scars surface during sliding and understanding of possible mechanisms involved in the formation of morphological patterns. The study includes an estimation of the influence of counterbody materials, load, test duration and surface roughness of films on the COF and wear rate. Thus, main activities of the work can be stated as follows:

- Study of frictional and wear behavior of diamond and DLC films against various counterbody materials: namely, influence of the coating/substrate and counterbody properties (chemical composition, initial surface roughness, Young's modulus) on the tribological behavior.
- Study of the influence of the sliding test parameters including the load, sliding speed and test duration on the frictional and wear behavior.
- Study of the influence of the sliding test parameters on the alteration in the morphology of the wear scars surface in the course of sliding.

2 METHODS AND TOOLS

2.1 Diamond and DLC films deposition methods

Diamond and DLC films as well as bulk diamond can be deposited using a number of chemical vapor deposition methods. The process involves feeding a deposition chamber with reacting gases, their ionization and providing conditions for bonding of ionized carbon-containing species with the substrate. Hot filament, microwave power or DC discharge are widely used tools of supplying energy needed for the process.

Regarding to the deposition of diamond and DLC films, CVD is a process in which a gaseous mixture (usually $\text{CH}_4 - \text{H}_2$) or C_2H_2 is heated up to the plasma activation temperature followed by formation of radicals (CH_3) and free hydrogen atoms (H). Chemical reaction occurs between these particles resulting in the formation of diamond films.

HFCVD

In the HFCVD reactor gaseous mixture (hydrocarbons, hydrogen and dopant-containing gases) is heated by hot filament made from materials with a high melting temperature (W, Ta), followed by the dissociation of gaseous species. The filament temperature is 2000 °C. The filament is located close to the substrate at the distance 4 – 10 mm and the pressure of the gaseous mixture is relatively low, *i.e.* about 20 – 60 Tr. Hot filament method allows the deposition of diamond films on a relatively large area of 2500 cm², but the deposition rate is not higher than 1 μm/h.

The advantages of the method are its relatively low cost and possibility to produce high-quality diamond films [96], however there are also some drawbacks. High temperature of the filament causes its degradation and the need for frequent exchange with a new one. Another disadvantage is poisoning of gaseous mixture by the filament materials. It results in micro and macro defects in the diamond films.

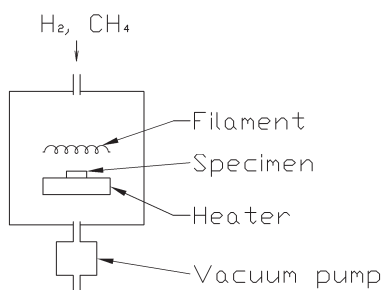


Figure 2.1 HFCVD schematics [97].

The NCD films used in the current study were deposited in a sp^3 Diamond Technologies, Inc. 655 reactor.

PECVD

In the PECVD method gas-discharge plasma is used for the dissociation of precursor gases into active radicals. This method allows use of higher pressures and hence reaching higher deposition rates.

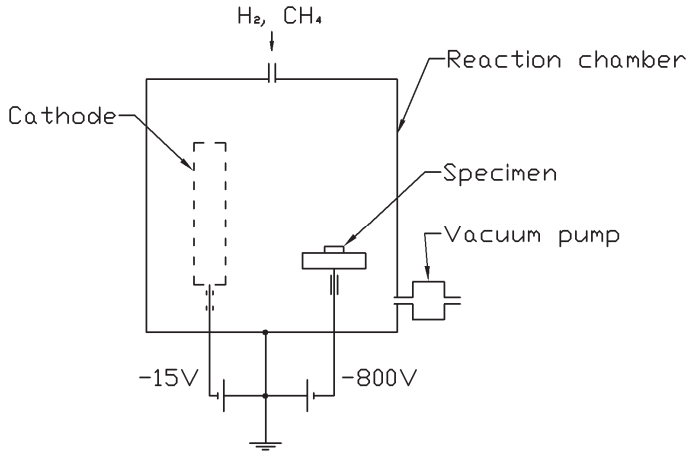


Figure 2.2 Schematics of the PECVD process implemented in a Platit $\pi 80$ PVD-PECVD reactor. Parts not used in the CVD process are shown by dashed lines.

The DLC films used in the present study were deposited in a Physical Vapor Deposition- Plasma Enhanced Chemical Vapor Deposition (PVD-PECVD) unit PLATIT $\pi 80$. DLC film was grown by the dissociation of acetylene (C_2H_2) in the glow discharge plasma process. The voltage drop (bias voltage) between the chamber and the specimen sample holder is about 100 V (AC).

MW-PECVD

One of the most popular methods is the MW-PECVD. Because no electrodes are used during the deposition the level of pollution is minimal in comparison with other methods. The MW-PECVD method allows depositing films on the area of 900 cm^2 with the rate of $20\text{ }\mu\text{m/h}$. By using that system, the growth of films can continue for many hours and the thickness of diamond films can reach 1 mm. A specific feature of microwave plasma is that at low pressures it consists from high energy electrons and “cool” ions as well as neutral molecules.

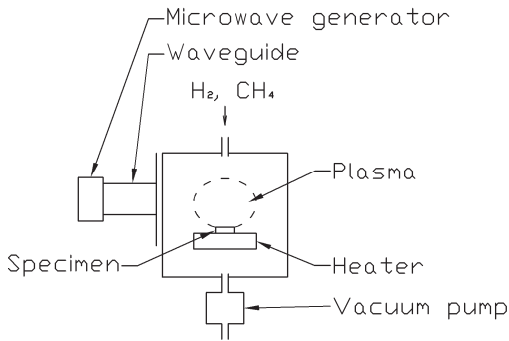


Figure 2.3 Schematics of the MW-PECVD chamber [97].

In the MW-PECVD reactor energy needed for the ionization of the precursor gases is supplied from microwave plasma usually of 2.45 GHz. The power is provided by the microwave generator (magnetron) and transmitted by the waveguide to the reaction chamber. An UPSA-100 (Optosystems Ltd.) reactor is used for deposition of diamond films in TUT.

2.2 Characterization methods

Raman spectroscopy

In Raman spectroscopy monochromatic radiation (laser light) is inelastically scattered on the molecules of the analyzed sample. Inelastic (Raman) scattering occurs due to energy exchange between photons and phonons generated by vibrating molecules, in contrast no energy exchange occurs in the case of elastic (Rayleigh) scattering. If a molecule obtains energy, the frequency of the scattered radiation becomes lower than the initial one (Stokes scattering) and higher if it loses energy (anti-Stokes). The shift in the radiation energy provides information about molecular vibrations in the material that allows us to identify its chemical composition and crystal structure. The value of the radiation energy shift depends strongly on the interatomic bonds orientation in the crystal and the weight of atoms. The heavier the atom the lower the frequency of its vibrations is and accordingly the maximum in the spectrum shifts in the direction of lower frequencies. Similarly the frequency shifts with the change in the bond energy.

In the current study the chemical structure of the diamond and DLC films was characterized by Raman measurements using a Horiba LabRam HR 800 high-resolution spectrometer equipped with a multichannel CCD detection system in the backscattering configuration. The laser light wavelength was 532 nm, and the spectral resolution of the spectrometer was 0.5 cm^{-1} .

SEM

In the SEM, an electron beam is thermionically emitted from an electron gun fitted with a tungsten or lanthanum hexaboride filament cathode. The electron beam is focused on the sample by condenser lenses and primary electron beam interacts with the sample surface. The electrons lose energy by repeated random scattering and absorption within the interaction volume. Interaction includes a

number of processes, namely the reflection of high-energy electrons by elastic scattering, emission of secondary electrons by inelastic scattering and the emission of electromagnetic radiation. Mentioned types of interaction can be measured by specialized detectors.

There are two main SEM modes used for imaging. In the secondary electron (SE) mode low-energy (<50 eV) secondary electrons are collected, *i.e.* those electrons that are ejected from the atoms of the sample due to inelastic scattering interactions with the primary electron beam. It is important because the energy of electrons is relatively low, only electrons located close to the sample surface can escape the sample, therefore this mode is sensitive to the roughness of the sample surface and the SE mode is used for topography imaging. In BSE mode the backscattered electrons which are high-energy electrons originating from the primary electron beam that are reflected or back-scattered by elastic scattering interactions with specimen atoms. Since heavy elements backscatter electrons more strongly than light elements, and thus appear brighter in the image, BSE mode is used to detect areas with different chemical composition.

In the present study SEM images were taken by a Zeiss EVO MA-15 system with LaB6 cathode in the SE mode, applying an accelerating voltage of 10 – 15 kV and 6.5 – 8.5 mm working distance.

Tribometry

To characterize the tribological properties of films reciprocating sliding tests were conducted using the CETR UMT-2 test system. The tester includes three motor driven linear stages providing reciprocating / rotating movement of the lower specimen and positioning of the upper one (with the counterbody holder). The lateral positioning stage is equipped with 2D force sensor perceiving the loading force and the lateral drag or friction force. The loading force sensor is used as a feedback for the vertical carriage positioning system to maintain a constant loading force. The combination of the loading force and friction is used to calculate the coefficient of friction.

Table 2.1 Main parameters of tribological tests.

Parameter	Value
Sliding distance	1 – 2 mm
Normal force	1 – 4 N
Frequency	2, 5, 8, 10 Hz
Duration	1800 – 108000 cycles
Balls material	Si ₃ N ₄ , Al ₂ O ₃ , ZrO ₂

The balls of Ø 3 mm (surface roughness $R_a = 0.012 \mu\text{m}$) (REDHILL, Czech Republic) were used as counterbodies.

Mechanical and optical profilometry

The wear volume was evaluated by means of mechanical and optical profilometry.

In mechanical profilometers a diamond stylus is moved in contact with a sample for a specified distance with a specified contact force. A profilometer can measure small surface variations using vertical stylus displacement as a function of position. The geometrical parameters of the wear scars (shape, length, depth, width) can be evaluated by scanning along and across the wear scar. Profilometric scans were done with a Mahr Perthometer[®] (Göttingen, Germany). Profile vertical resolution provided by the profilometer is 0.07 nm, lateral 0.5 μm .

In the optical profilometer the beam of primary light is split into two separate beams. One beam is directed towards the sample and another towards an internal reference mirror. The reference beam interferes with the beam reflected from the sample. Positive interference measured by a light detector as an interference maximum can be used to calculate the position of the surface. The roughness of the whole sample surface can be estimated by scanning of the beam along the surface. Optical measurements were done with a Bruker Contour GT-K0 optical 3D microscope. Vertical resolution of the device is 0.01 nm and lateral resolution 0.38 μm .

AFM

Atomic force microscope scans the surface with a sharp probe fixed on the end of a cantilever. When the tip is situated in the proximity of the sample surface, forces between the tip and the sample (mechanical, van der Waals, electrostatic, magnetic and others) lead to the deflection of the cantilever. This deflection is measured using a laser spot reflected from the cantilever into the photodiode array. There are several imaging modes available. In contact mode the probe is in constant contact with the surface. In semi-contact mode the probe touches the surface performing oscillations near its resonance frequency. The amplitude of oscillations depends on the distance to the surface. In non-contact mode the probe oscillates at its resonance frequency. Oscillation frequency decreases due to the influence of van der Waals and other long-range forces in the vicinity of the sample. AFM resolution depends on the probe shape and can reach fractions of a nanometer.

AFM measurements were conducted with an NT-MDT Solver P47 system at scan sizes of 20x20 and 5x5 μm^2 using Si cantilevers and tips in contact mode. AFM measurements (NT-MDT Solver P47) were performed in contact mode using Si cantilevers and tips.

2.3 Surface texture parameters

Surface texture parameters with their calculation formulas and descriptions used in the current work are listed in Table 2.2 In the present thesis both parameters R_a and R_q were used to characterize the surface roughness, because

some authors argue importance of both parameters. Parameter R_z is suitable to describe the distribution of large asperities and deep valleys on the surface.

Table 2.2 Main surface roughness parameters [94].

Parameter	Description	Formula
R_a	Arithmetic average height. Average absolute deviation of the roughness irregularities from the mean line over the sampling length.	$R_a = \frac{1}{n} \sum_{i=1}^n y_i $
R_q	Root mean squared. Standard deviation of the distribution of surface heights.	$R_q = \sqrt{\frac{1}{n} \sum_{i=1}^n y_i ^2}$
R_z	Ten points height. Average distance between the 5 highest peaks and the 5 lowest valleys over the sampling length	$R_z = \frac{1}{S} \sum_{i=1}^S R_{ti}$

2.4 Statistical analysis of data

Between variables X and Y (random variables) a functional dependence can exist, and the variable Y can be described by X through a mathematical equation. However mainly there are situations when one variable (say Y) reacts on the change in another (say X) with the change in its distribution. Such relation is named a stochastic relation and occurs due to the influence of some factors on both variables X and Y. In the correlation analysis approach, the correlation denotes a measure of relation between variables. The degree of correlation can be described using correlation coefficients, ranging from -1 to 1 . Correlation coefficients equal to -1 and 1 denote perfect negative and positive correlation and 0 means absence of correlation.

There are two main types of statistical methods. First, in parametrical methods variables can be characterized by a known class of distribution functions, for instance variable X and Y are distributed according to normal distribution law under any disturbing factors. Second, in nonparametric methods the distribution function is unknown and only some conditions should be satisfied (continuity, *etc.*). In other words, the conditions are not so tough in comparison with parametrical methods, which correspond to many situations in the analysis of experimental data [95].

The Spearman correlation analysis is a nonparametric statistical method. The Spearman correlation rank coefficient is determined by the following formula:

$$r_s = 1 - \frac{6}{n^3 - n} \sum_{i=1}^n (r_i - q_i)^2 \quad (2.1)$$

where r_i and q_i mean the ranks of the corresponding variables x_i and y_i . The number n is the sample size. Variables must be ranked before applying that formula.

The next step in the analysis of statistical data is to estimate the statistical significance of the correlation. Because the sample size is always restricted, there is a possibility of a sampling error, *i.e.* the observed effect may not appear with another sample size. Therefore the hypothesis of the existence of correlation (hypothesis H_1) must be carefully tested and compared with null hypothesis, *i.e.* no correlation exists (hypothesis H_0). For the sample size $n > 10$, the critical quantity

$$T = r_s \frac{\sqrt{n-2}}{\sqrt{1-r_s^2}} \quad (2.2)$$

If H_0 is valid, then r_s possesses a special distribution and, correspondingly, the distribution of quantity T is asymptotically the Student's distribution. The critical value of t_c is the quintile c_p of the Student's distribution with the $n - 2$ degrees of freedom calculated for the specific p -value. P -value is the probability of error due to rejecting the null hypothesis (Type I error). Hypothesis H_0 is accepted if $|T| \leq t_c$, otherwise H_0 is rejected. In practice, 90 % (p -value is 0.1) is the minimum of confidence level for statistically significant results.

3 WEAR BEHAVIOR OF NCD AND DLC FILMS

The experimental part of the present research includes morphology studies of the wear scar surfaces on the diamond and DLC films. Reciprocating ball-on-disc tests were conducted under normal air ambient conditions. Section 3.1 presents the investigation of the influence of the ball materials (Si_3N_4 , ZrO_2 and Al_2O_3 ceramics) on the morphology of the wear scar surface. In sections 3.2 and 3.3 only Si_3N_4 balls were used as the counterbodies. It was found that the manifestation of the ripple patterns can depend on test duration and applied load (see section 3.2). Section 3.3 analyzes the deflection of the NCD film surface during the sliding test. Based on the observed deformation of diamond films, a ripple formation mechanism is suggested. Section 3.4 discusses the correlation between the initial DLC film surface roughness and roughness observed after relatively extended tests (steady stage regimes).

3.1 Wear behavior of NCD films

3.1.1 Relation between morphological changes of the NCD films and the ball material

The chemical composition of the counterbody material and, correspondingly, mechanical/tribological properties is an important factor defining the frictional behavior and the wear resistance of the diamond films. Silicon nitride, alumina and zirconia ceramic balls were selected as the counterbodies to evaluate tribological properties of the NCD film under dry sliding conditions. In the case of Si_3N_4 and Al_2O_3 the frictional behavior was quite similar, however tests with ZrO_2 revealed remarkable differences.

Using HFCVD technique diamond films were deposited on monocrystalline (100)-oriented silicon wafers. The deposition parameters were as follows: 2.4 % CH_4/H_2 gas mixture at 6 Torr and substrate temperature was 850 °C. The unbalanced deposition process was used to prepare cauliflower-like surface structure, see Figure 3.1. Films thickness was 0.8 μm . The tribological tests were conducted using \varnothing 3 mm Si_3N_4 , Al_2O_3 , and ZrO_2 balls. According to the manufacturer data, the hardness and Young's modulus of the balls were 1400-1700 HV and 310 GPa, 1400 HV and 350 GPa, and 650-830 HV and 195 GPa respectively. Tests duration was 3000, 9000 and 36000 cycles. A 2 N load was applied, the sliding distance was 1 mm and the sliding frequency was 5 Hz.

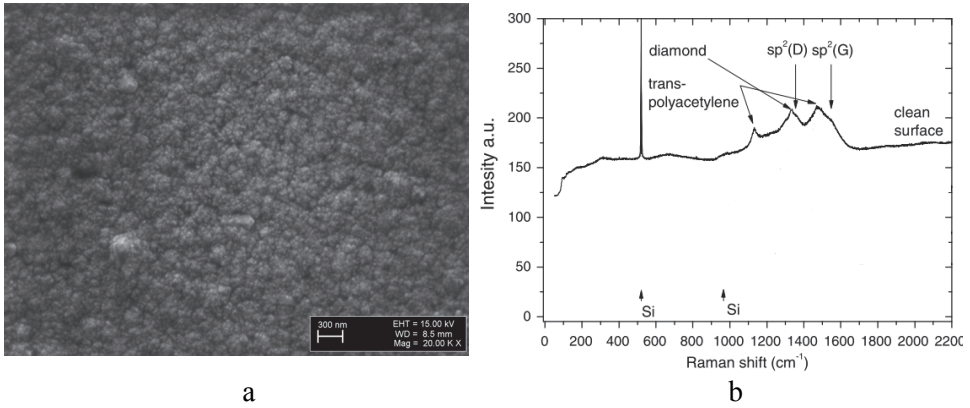


Figure 3.1 SEM image (a) and Raman spectrum (b) of the pristine NCD film [Publication I].

Figure 3.1 shows the typical Raman spectrum of the pristine NCD film. The peaks at 522 and 976 cm^{-1} correspond to the Si substrate, the peak at 1332 cm^{-1} relates to diamond and the peaks at 1134 and 1478 cm^{-1} relate to the presence of trans-polyacetylene (t-PA) at the grain boundaries [98]. The peaks at 1355 and 1540 cm^{-1} correspond to the D and G bands [99]

Ripple patterns on the NCD films formed after sliding with Si_3N_4 balls

Figure 3.2 shows the COF versus the number of cycles. The COF value quickly changes from 0.4 at the beginning of the test to 0.1 after about 2000 cycles, *i.e.* steady-state regime is reached relatively fast.

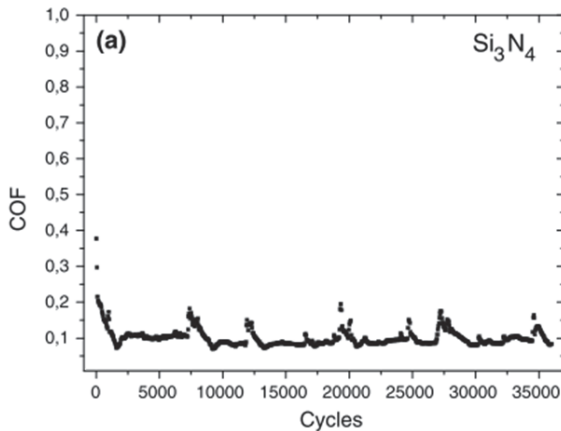


Figure 3.2 Coefficient of friction in sliding test with Si_3N_4 ball against the NCD film [Publication I].

However, the periodic spikes in the COF value were observed during steady-stage sliding. Similar behavior of COF in the Si_3N_4 /NCD sliding tests was reported by Erdemir *et al.* [4]. Such spikes were explained with periodic formation and destruction of the carbonaceous transfer layer. Short run-in

period can be explained by the formation of stress-induced sp^2 -rich layer [100] as well.

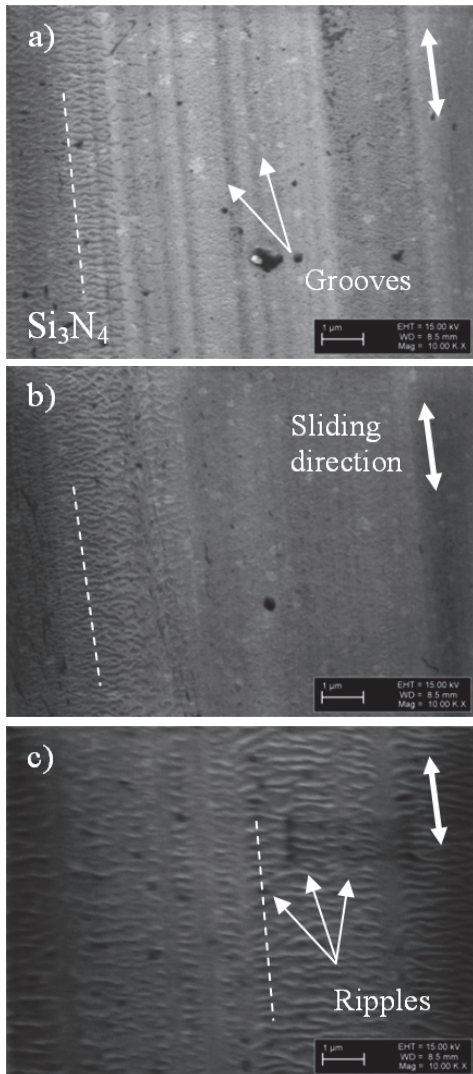


Figure 3.3 SEM images of rippling on wear scar surfaces at 3000 cycles (a), 9000 cycles (b) and 36000 cycles (c) of sliding with Si_3N_4 ball [Publication I].

Longitudinal grooves and transverse rippling can be observed on the SEM images, see Figure 3.3. We suggest that the micro-ploughing mechanism is a reasonable explanation of the possible origin of grooves. The rippling patterns on the wear scar surface can be observed already after 3000 cycles. The density of ripples, *i.e.* the number of ripples per micrometer varies with the test duration. It changes from about 6 ripples/ μm for 3000 and 9000 cycles to about 4 ripples/ μm after 36000 cycles. In addition the ripple patterns manifestation is more clear after 36000 cycles than 3000 and 9000 cycles.

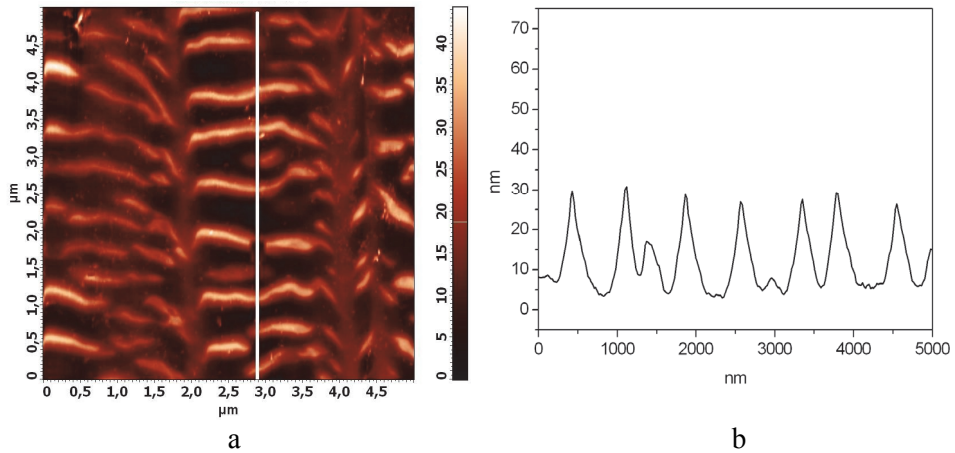


Figure 3.4 AFM image of the wear scar after 36000 cycles of sliding against Si_3N_4 ball (a). The place of the line scan (b) marked with a white line on the image (a) [Publication I].

The size of the ripples is about 25 – 30 nm in height as measured after 36000 cycles by the AFM technique (see Figure 3.4).

Ripple patterns on the NCD films formed after sliding with Al_2O_3 balls

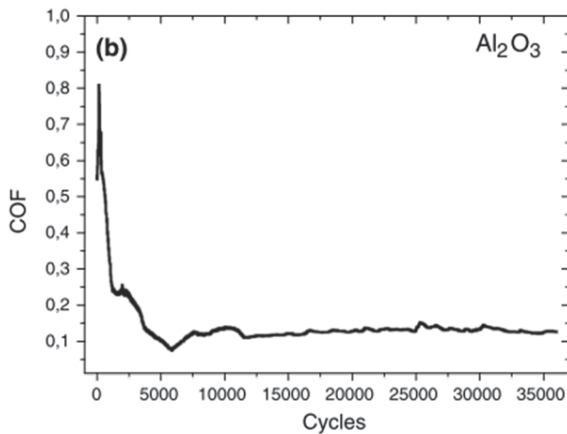


Figure 3.5 Coefficient of friction in the sliding tests with Al_2O_3 ball against the NCD film [Publication I].

There is a slight difference between the frictional behavior of NCD films against Si_3N_4 and Al_2O_3 balls. The run-in period is longer in the case of tests with Al_2O_3 balls (up to 10000 cycles), see Figure 3.5 and, in addition no COF oscillations during the steady-state regime occur.

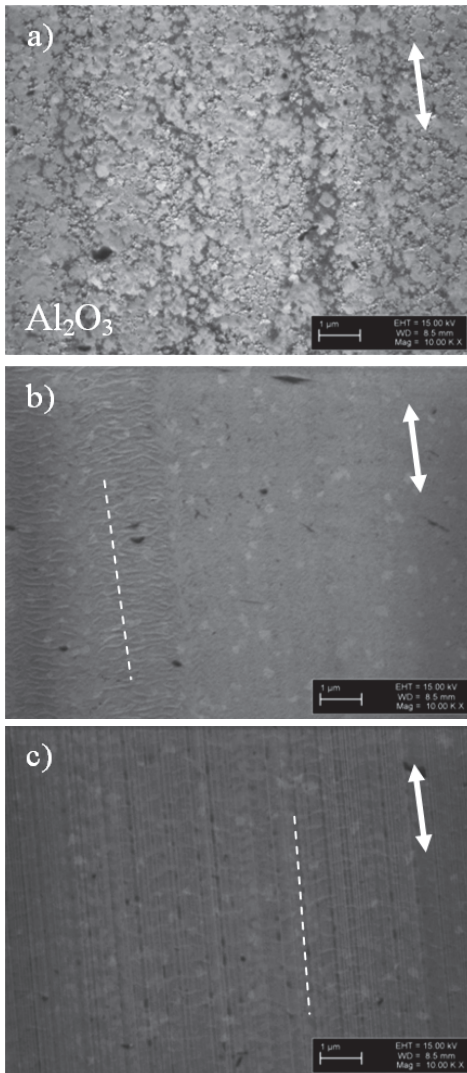


Figure 3.6 SEM images of rippling on wear scar surfaces at 3000 cycles (a), 9000 cycles (b) and 36000 cycles (c) of sliding with Al_2O_3 ball [Publication I].

In the case of alumina balls ripples were not observed after 3000 cycles, see Figure 3.6. The polished NCD film surface was revealed on the SEM image taken after 3000 cycles. However, ripples density varied similarly to the tests with Si_3N_4 balls tests after 9000 and 36000 cycles of sliding. Ripples density was about 6 ripples/ μm after 9000 cycles and 3 ripples/ μm after 36000 cycles. In contrast, ripple patterns were much fainter compared to patterns obtained in the tests with Si_3N_4 balls.

A systematic investigation of wear rate dynamics on the NCD films in sliding tests with Al_2O_3 balls was carried out.

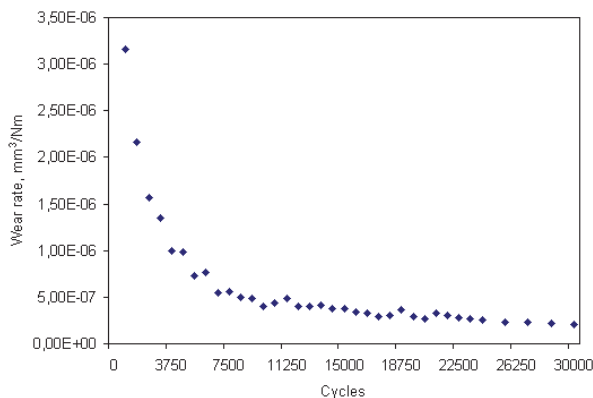


Figure 3.7 Wear rate vs cycles in NCD/Al₂O₃ tests. Load 2 N, distance 1 mm, sliding frequency 5 Hz.

Sliding tests were conducted with alumina balls. Test duration ranged from 750 to 30000 cycles with the step of 750 cycles (last 4 tests were done with 1500 cycles step). The wear volume was measured using a mechanical profilometer and the wear rate was evaluated. Additionally wear scars volume was measured using the optical profilometer. The results obtained by both methods have shown good coincidence. The wear rate calculated for the first scars equals to $3.2 \cdot 10^{-6} \text{ mm}^3/\text{N} \cdot \text{m}$, whereas for the last one to $2.1 \cdot 10^{-7} \text{ mm}^3/\text{N} \cdot \text{m}$. The wear rate shows fast exponential-like behavior, indicating that the main part of wear occurs during the run-in period, *i.e.* about 10000 cycles. This is close to the results obtained for Si₃N₄ balls rubbed against NCD in air [4]. COF values obtained in these tests were quite similar to those described above for Al₂O₃ balls.

Ripple patterns on NCD films formed after sliding with ZrO₂ balls

The frictional behavior of NCD films against ZrO₂ remarkably differs from that with Si₃N₄ and Al₂O₃ balls.

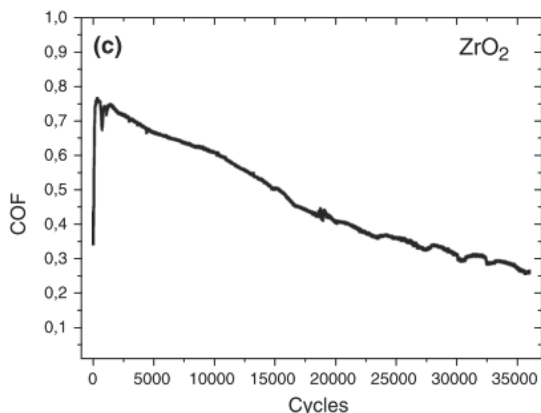


Figure 3.8 Coefficient of friction in sliding tests with ZrO₂ ball against NCD film [Publication I].

The COF increase at the very beginning from 0.35 to 0.75 is followed by a slow decrease during the test, neither clear run-in nor steady-state regimes were observed, see Figure 3.8. Figure 3.9 shows the wear scars on the NCD surface after sliding tests with different test durations.

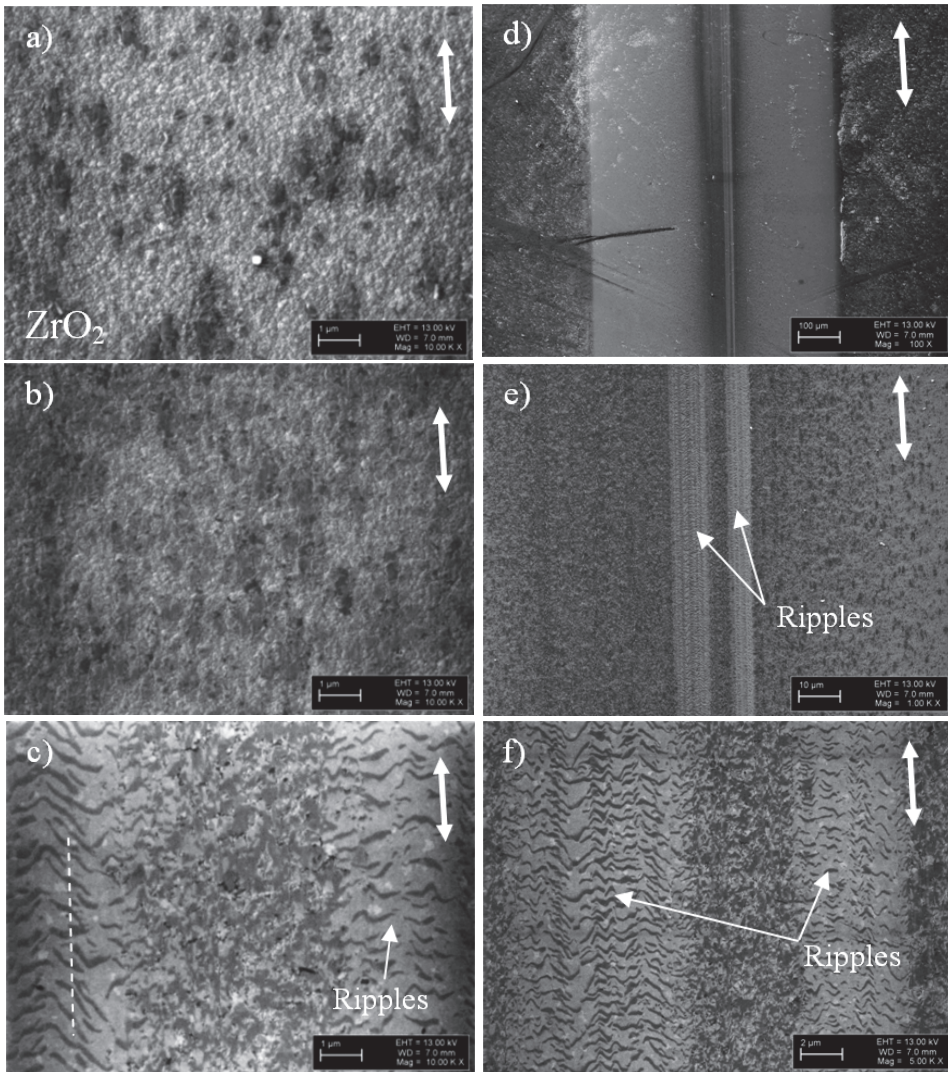


Figure 3.9 SEM images of rippling on wear scar surfaces at 3000 cycles (a), 9000 cycles (b) and 36000 cycles (c) of sliding with ZrO_2 ball and the wear scar surface at different magnifications (d: $\times 100$, e: $\times 1000$, f: $\times 5000$) taken from the center of the wear scar surface formed on the NCD film after 36000 cycles of sliding against ZrO_2 [Publication I].

The SEM images in Figure 3.9a – c show that ripple patterns appear only after 36 000 cycles, and Figure 3.9d – f shows that ripple patterns, first of all, are formed in the middle of the wear scar. The last observation allows us to

stress the importance of contact pressure to explain the observed frictional behavior of NCD films. We believe that the black spots within the wear scars correspond to the points where the stress-induced amorphization of the NCD films occurs with the following formation of a carbon-like layer. The slow descent in the COF value in Figure 3.8 can be explained by insufficient formation of the amorphous layer. Indeed the Young's modulus of ZrO_2 is about 1.5 times lower than that of Al_2O_3 and Si_3N_4 , therefore the contact pressure is lower in the case of ZrO_2 . The COF decreases because the total area of black spots increases. On the other hand, the contact pressure is highest at the center of the contact area and the density of the black spots is the highest in the central part of the wear scar. Ripples appear after percolation of black spots, which suggests that there is a correlation between the ripple formation and the stress-induced amorphization of the diamond surface.

Relation between amorphization and rippling

Comparison of Raman spectra recorded on as-deposited NCD film (see Figure 3.1b) and wear scar surfaces after 3000, 9000 and 36000 cycles of sliding against Si_3N_4 and Al_2O_3 (see Publication I) has shown a clear decrease in the peak intensity ratios between the diamond peak and peaks corresponding to sp^2 (D, G) and t-PA at 1.478 cm^{-1} observed on the wear scar surfaces, *i.e.*, a stress-induced transition from sp^3 to sp^2 bonding takes place on the diamond surface. In the case of Si_3N_4 the minimal ratio is reached after 3000 cycles and in the case of Al_2O_3 and ZrO_2 after 9000 cycles. The alteration of the ratio value between the intensities of diamond and sp^2 (D, G) peaks is lower in the case of zirconia balls. The relative decrease in Raman peak intensity ratios seems to depend on the mechanical properties of the counterbody material, *i.e.*, the greatest differences are detected for the hardest counterbody materials (Si_3N_4 and Al_2O_3), whereas differences for softer ZrO_2 balls are less pronounced.

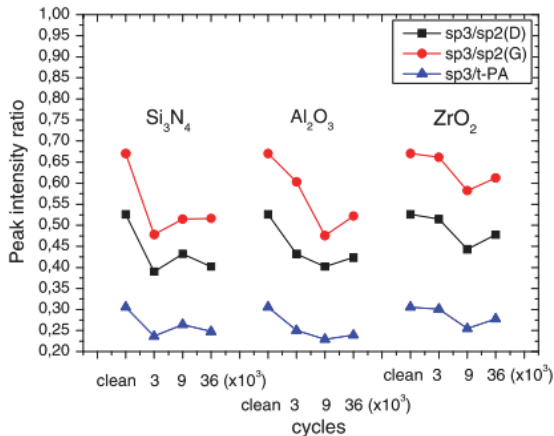


Figure 3.10 $Sp^3/sp^2(G)$, $sp^3/sp^2(D)$ and $sp^3/t-PA$ peak intensity ratios for clean NCD surface and after 3000, 9000 and 36000 cycles of sliding respectively [Publication I].

The ripples are formed in the surface regions enriched with amorphous carbon material. In the case of sliding against Si_3N_4 and Al_2O_3 the first observations of ripple patterns coincide with minimal values of sp^3/sp^2 (D, G). A gradual smoothing of the NCD pristine surface was observed in the case of ZrO_2 , with a minor decrease in the diamond/ sp^2 (D, G) intensity ratios as compared with Si_3N_4 and Al_2O_3 , and ripples were observed only after 36000 sliding cycles. Therefore, it can be assumed that there is a correlation between the NCD surface amorphization and the formation of ripple patterns.

For more details see Publication I

Wear rate of the ZrO_2 ball

The SEM images taken on the ZrO_2 ball after 54000 cycles of sliding are shown in Figure 3.11. The diameter of the worn area is about $400\ \mu\text{m}$ that gives the wear rate of the ball equal to $4 \cdot 10^{-6}\ \text{mm}^3/\text{Nm}$. Grooves can be clearly seen on the surface. Because no visible transfer layer can be observed, a ploughing mechanism can be reasonably suggested as the wear mechanism for ZrO_2 balls.

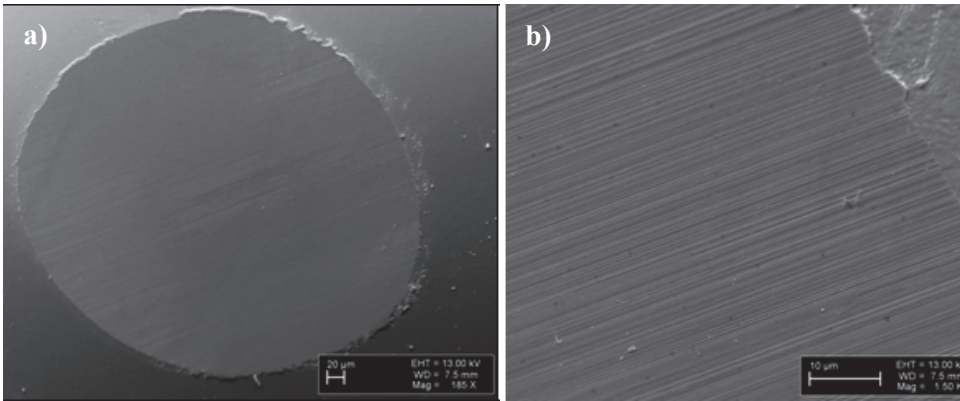


Figure 3.11 SEM image of the worn ZrO_2 ball after 54000 cycles of sliding at 5 Hz at different magnification. The scale bar length is $20\ \mu\text{m}$ (a) and $10\ \mu\text{m}$ (b).

3.1.2 Relation between morphological changes of the NCD films and the sliding distance

The cauliflower-like NCD films described in section 3.1 were used. The load in the tribological tests was 2, 3 and 4 N, the frequency was 2, 5 and 10 Hz, the distance varied from 14 400 cycles up to 108 000 cycles and $\text{Ø}3\ \text{mm}$ Si_3N_4 balls were used as a counterbody.

Although three different loads were used, the results are based only on the tests with 2 and 3 N. A sudden delamination of the NCD films was observed for all tests with 4 N load (catastrophic wear), in the case of tests with 3 N only a part of tests was successfully conducted. The longest one for 3 N load was for 36000 cycles at 5 Hz. Figure 3.12 shows typical COF curves obtained for the NCD/ Si_3N_4 tribopair. In the steady-state stage COF stabilizes at the values of

0.08 – 0.12. Periodic COF spikes were observed, which are similar to those mentioned in the previous section.

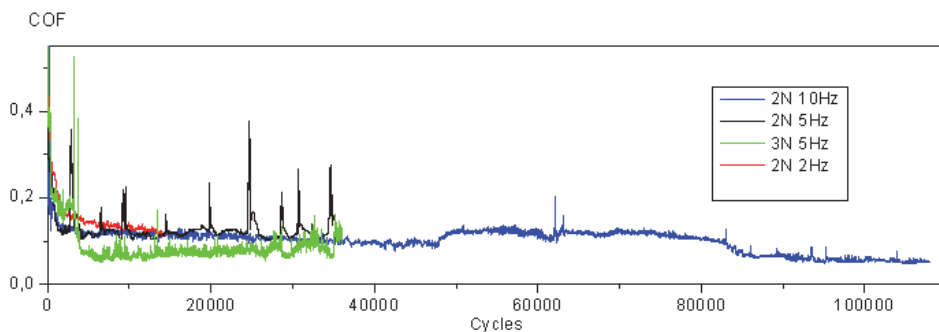


Figure 3.12 COF versus cycles curves at 2, 5 and 10 Hz, load 2 and 3 N, for different sliding distances [Publication II].

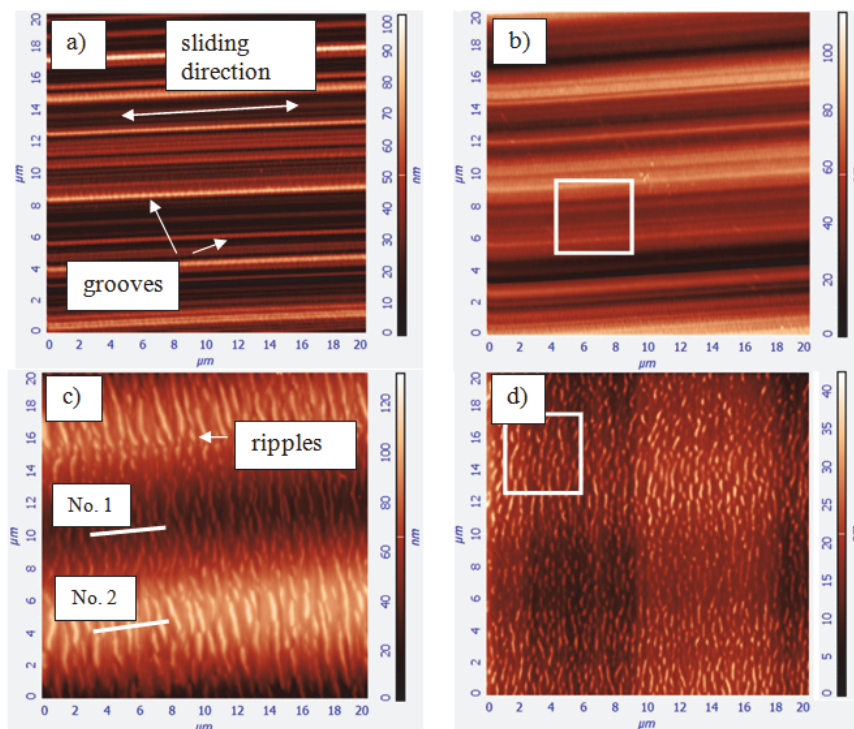


Figure 3.13 AFM images ($20 \times 20 \mu\text{m}^2$) taken after (a) 2 N, 2 Hz (14 400 cycles), (b) 2 N, 5 Hz (36 000 cycles), (c) 2 N, 10 Hz (72 000 cycles) and (d) 2 N, 10 Hz (108 000 cycles) tests. The white squares in b and d are about $5 \times 5 \mu\text{m}^2$ in size and indicate locations at which images shown in Figure 3.14a and Figure 3.14c were taken [Publication II].

The wear scars investigation by AFM (see Figure 3.13 and Figure 3.14) revealed longitudinal grooves and transversal ripples. The density of grooves decreases with increasing frequency (from 2 Hz to 10 Hz) and sliding distance (from 14 400 to 108 000 cycles).

Figure 3.14a is a part of Figure 3.13b confined within the white square; the same applies for Figure 3.14c and Figure 3.13d.

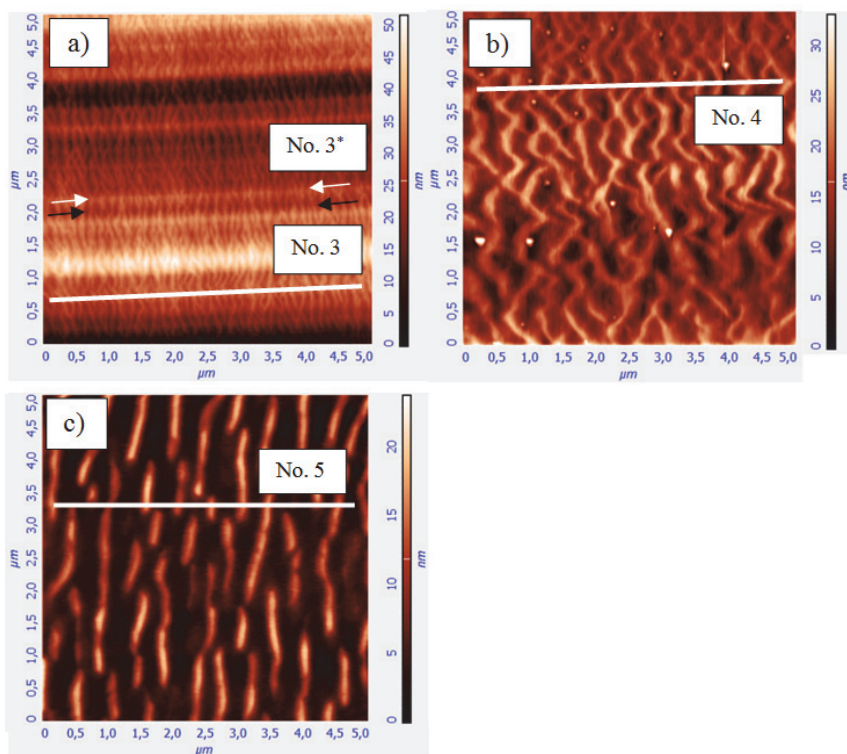


Figure 3.14 AFM images ($5 \times 5 \mu\text{m}^2$) taken after (a) 2 N, 5 Hz (36 000 cycles), (b) 3 N, 5 Hz (36 000 cycles) and (c) 2 N, 10 Hz (108 000 cycles) tests. The image (a) was taken on the place marked by white square in Figure 3.13b and the image (c) in Figure 3.13d, respectively [Publication II].

Line scans of approximately $5 \mu\text{m}$ in length were taken from Figure 3.13c and Figure 3.14a – c at the locations indicated by straight white lines and the surface geometrical parameters R_a (arithmetic average roughness), R_q (root-mean-square roughness), R_z (ten point height of irregularities) and D (profile peak density, *i.e.* the number of peaks along the scan line) were obtained from it and are reported in Table 3.1.

Table 3.1 Parameters R_a , R_q , R_z and D , derived from scans No. 1 – 5.

Line scan No.	R_a , nm	R_q , nm	R_z , nm	D , pcs
No. 1 (20x20 μm^2)	4.6	5.8	19.6	9.4
No. 2 (20x20 μm^2)	6.2	7.9	24.8	7.5
No. 3 (5x5 μm^2)	1.7	2.0	8.4	38.0
No. 3* (5x5 μm^2)	1.2	1.5	6.4	29.0
No. 4 (5x5 μm^2)	2.3	2.7	10.4	17.8
No. 5 (5x5 μm^2)	3.3	3.9	12.5	7.8

It is worth noting that the experiments done at 2 and 3 N, see Figure 3.14 show similar results. The transversal ripples appear as continuous surface corrugations in both tests at 5 Hz and 36 000 cycles, see Figure 3.14a and b. The difference between R_a , R_q and R_z is about 20 – 25 %, however the peak density obtained from Figure 3.13a nearly doubles compared to Figure 3.13b; see Table 3.1 (line scans No. 3 and 4).

Although continuous ripples are observed in Figure 3.14a and b, the ripples become broken in Figure 3.13c, Figure 3.13d and Figure 3.14c. The decrease in peak density for the line scan No. 3* can be explained by fragmentation of ripples due to wear, which starts on top of the ripples and results in a decrease of their apparent height and possible final elimination. It is indicated by a decrease in the roughness parameter value for the line scan No. 3*, as opposed to No. 3. A difference in the wear regime for certain ripples may explain the formation of the complex ripple patterns shown in Figure 3.13c and d. The geometrical parameters for the line scan between the black arrows (see Figure 3.14a) were similar to those for the line scan No. 3.

For more details see Publication II

3.1.3 Deformation of the NCD films during sliding tests

A NCD film with a thickness of 0.8 μm was grown on a 100-mm diameter (100)-oriented 500 μm thick Si wafer by hot-filament chemical vapour deposition (HFCVD) under balanced conditions using an sp^3 Diamond Technologies, Inc. 655 reactor in a 2.4 % CH_4/H_2 gas mixture. The substrate temperature was about 850 °C and the chamber pressure was maintained at 6 Torr. After the NCD film deposition, the Si wafer was cut into bars of about 10 mm^2 in size along cleavage directions. The average roughness R_a value of the as-deposited film was 0.019 μm .

Room temperature Raman spectra were recorded by using a Horiba LabRam HR 800 high-resolution spectrometer equipped with a multichannel CCD detection system in the backscattering configuration. The laser light wavelength was 532 nm, and the spectral resolution of the spectrometer was 0.5 cm^{-1} .

Reciprocating sliding tests (normal load 2 N, displacement amplitude 1 mm, frequency 2, 5 and 8Hz, relative humidity about 35 %, ball diameter $\text{\O} 3$ mm) were carried out by means of a CETR[®] UMT-2 tribometer. Si_3N_4 balls (surface

roughness $R_a = 0.012 \mu\text{m}$) (REDHILL, Czech Republic) were used as a counterbody. The duration of the tests was 1800, 3000 and 6000 cycles.

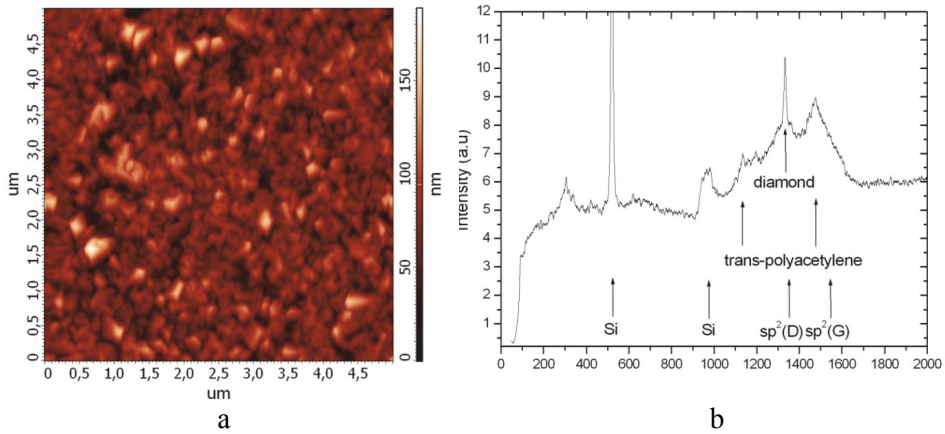


Figure 3.15 AFM image of the pristine surface (a) and Raman spectrum (b) of the NCD film [Publication III].

Figure 3.15 shows surface morphology and Raman spectra taken on the NCD film. The run-in period of the NCD films is characterized by high initial COF value (0.4 – 0.6), which further goes down to the value of about 0.1 – 0.15.

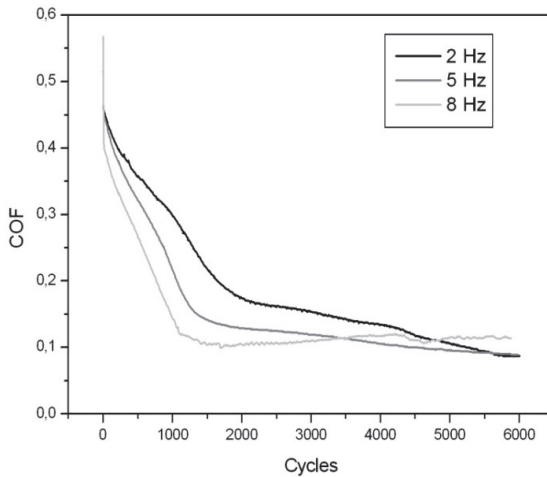


Figure 3.16 COF versus cycles curves after 6000 cycles at 2, 5 and 8 Hz [Publication III].

Because of the progressing NCD film surface abrasion, the COF value decreases gradually and, finally, stabilizes at about 0.1. In the case of the test done at 8 Hz, the run-in period is shorter than for tests carried out at 2 and 5 Hz, *i.e.* the surface smoothening proceeds faster with the higher ball velocity.

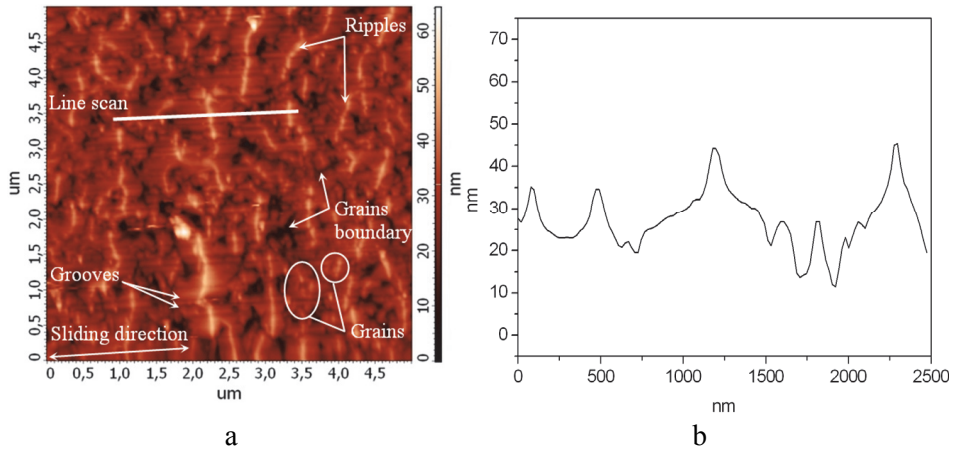


Figure 3.17 AFM image of the worn NCD film surface after 1800 cycles of sliding at 8 Hz (a) and a line scan of the surface (b).

The results of AFM measurements indicate that polishing occurred on the diamond surface. Clear ripple patterns are formed approximately in the middle of diamond grains (visible as white lines in Figure 3.17a. Figure 3.17b represents a line scan taken along the wear scar. Asperities of 15 – 20 nm in height seen on the image represent ripples. The ripple density is about 2 ripples/ μm and the ripple height is 15 – 20 nm.

Three line scans were done on each particular wear scar, *i.e.* scanning in the direction perpendicular to the sliding direction and an averaged line scans profile was prepared shown in Figure 3.18.

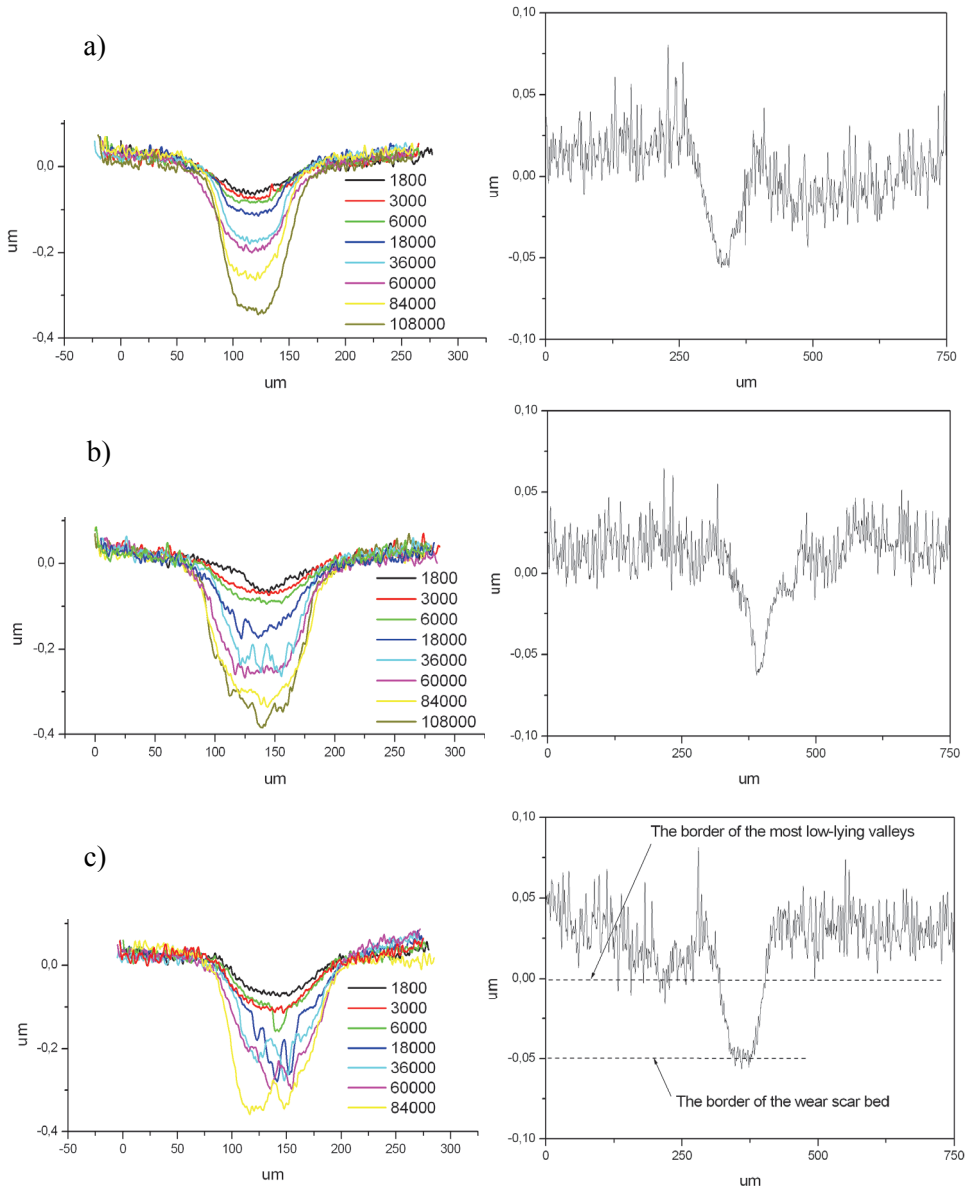


Figure 3.18 Averaged line scans taken on the wear scar surfaces after 1800 – 108000 cycles of sliding at 2 Hz (a), 5 Hz (b) and 8 Hz (c). Left row – averaged results from 5 measurements, right row – single measurement after 1800 cycles [Publication III].

It can be seen that already after 1800 cycles the border of the wear scar bed is about $0.05 \mu\text{m}$ below the border of the deepest valleys of the pristine NCD film surface, see Figure 3.18. At the same time the diamond grains and grain boundaries are still visible in Figure 3.17. Therefore the results of profilometric measurements shown in Figure 3.18 are more adequately described by the scheme shown in Figure 3.19a than in Figure 3.19b

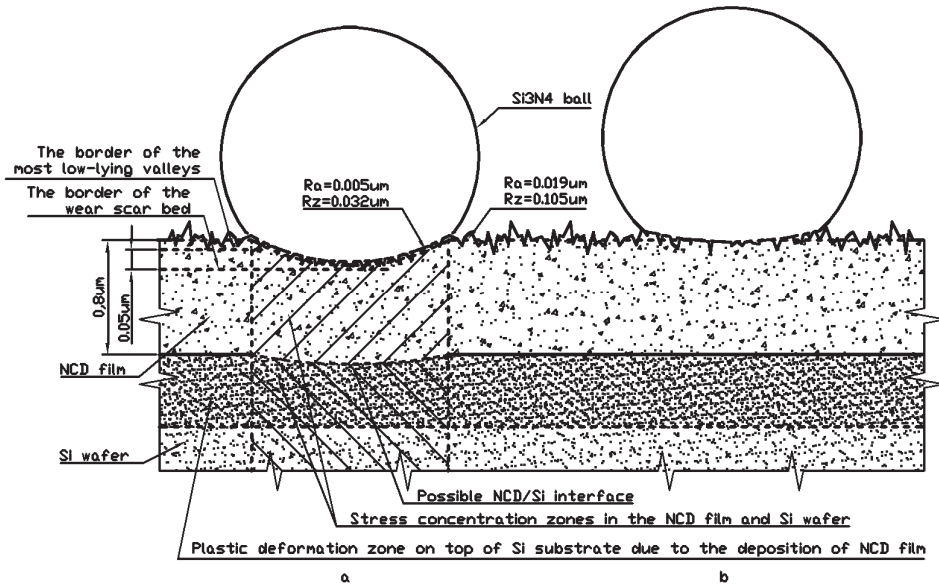


Figure 3.19 Schematic representation of the results shown in Figure 3.18: wear scar profile according to profilometric measurements after 1800 cycles sliding at 8 Hz (a) and expected wear scar profile in assumption that no NCD film deflection occurs (b) [Publication III].

It can be assumed that the NCD film is not deflected as schematically shown in Figure 3.19b. However the analysis of wear scars profile suggests that the NCD film can be plastically deformed during the sliding tests. This vertical deformation (further called ‘deflection’) is about 0.05 μm after 1800 cycles sliding at 8 Hz, wherein, no visible cracks were observed on the wear scars surface.

Analysis of the line scans shown in Figure 3.18 suggests that the wear scars surface can be substantially corrugated. The average roughness R_a within the wear scars (excluding the area out of wear scar in Figure 3.18) is shown in Figure 3.20.

The roughness varies considerably with the speed of sliding and the test duration. The highest roughness was observed for the test with 8 Hz. After the initial decrease in the roughness from $R_a = 0.019 \text{ nm}$ for the pristine film to $R_a = 0.003 - 0.004 \text{ nm}$ after 1800 cycles of sliding, the R_a value increases, however a dependence on sliding speed can be observed. The highest value of R_a equal to 0.019 nm was found after 18000 cycles with 8 Hz, R_a equal to 0.015 nm was found after 36000 cycles with 5 Hz and R_a equal 0.005 nm was found after 60000 cycles with 2 Hz.

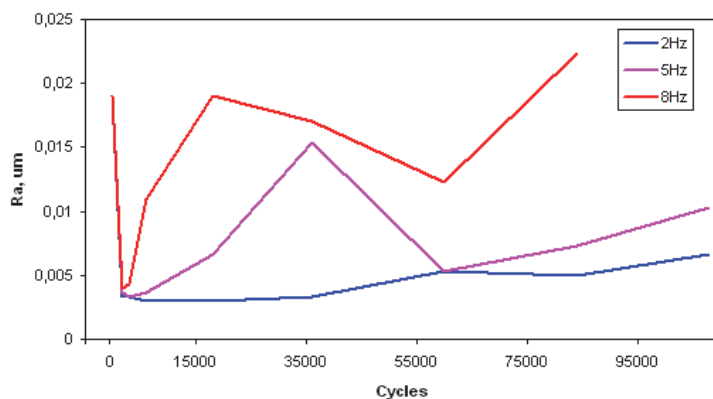


Figure 3.20 Roughness across wear scars at 2, 5 and 8 Hz.

Corrugations within the wear scars can be explained by the appearance of grooves similar to ones described in section 3.1.2.

The deflection of NCD films can be correlated with the plastic deformation of the silicon substrate. Hardness of monocrystalline Si (100) is about 12 GPa [101]. Young's modulus varies along the directions on (100) plane from about 130 [102] to 170 – 180 GPa [101, 102], the Poisson ratio is 0.278 [103]. According to the data provided by Ericsson *et al.* [104], the fracture strength of silicon is 6.1 GPa. In the case of 2 N load, the maximal contact pressure on the Si surface should be only 1.2 – 1.4 GPa and the mean contact pressure 0.8 – 0.9 GPa, which is clearly insufficient for the plastic deformation of silicon. However, a considerable decrease in strength, up to 1.5 GPa, was reported for the damaged surface. Michler *et al.* report [105, 106] that considerable plastic deformations are present in the surface layer of the Si wafer due to thermal stress. Such layer will obviously have reduced mechanical strength and will be subject to deformation under mechanical loading.

Thus, the NCD film deflection can be explained by the plastic deformation of the Si (100)/NCD interface. The high Young's modulus and a relatively small thickness of the NCD film provide flexibility to the NCD film [107] and hence the NCD film surface can deform during sliding without cracks and surface failure. A bent torus on the NCD film surface is likely formed in front of the ball (as shown in [107]) during sliding. Periodic bending of the NCD film during reciprocating sliding could also contribute to the formation of ripples on the wear scar surface.

For more details see Publication III

Surface of the Si_3N_4 balls after sliding tests against the NCD film

The tests were conducted using the Si_3N_4 balls rubbed against the NCD-coated samples, described at the beginning of section 3.1.

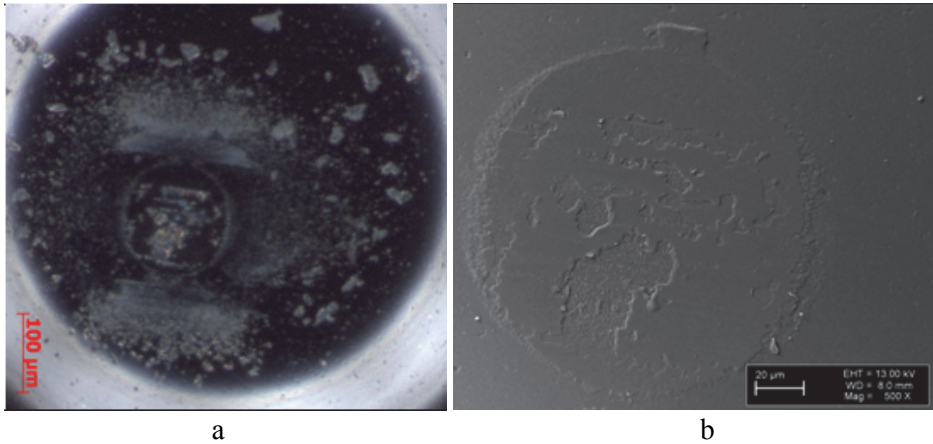


Figure 3.21 Optical micrograph (a) and SEM image (b) of the worn Si_3N_4 ball after 60000 cycles of sliding at 8 Hz, 2 N load.

The images taken by optical microscopy and SEM on the Si_3N_4 ball are shown in Figure 3.21. The diameter of the worn area is about 140 μm and the corresponding wear volume (the volume of the spherical segment) of Si_3N_4 is $1.2 \cdot 10^{-5} \text{ mm}^3$ that gives the wear rate of $5 \cdot 10^{-8} \text{ mm}^3/\text{N}\cdot\text{m}$. This is about 3 times lower than the wear rate of the NCD film ($1.4 \cdot 10^{-7} \text{ mm}^3/\text{N}\cdot\text{m}$). However, such result can be explained if a possible film deflection is taken into account.

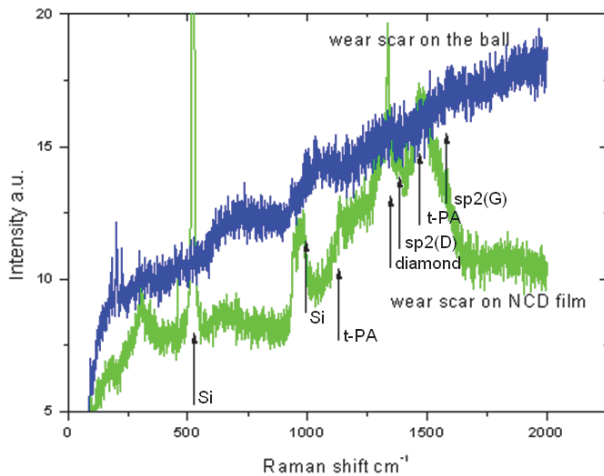


Figure 3.22 Raman spectra taken on the wear scar surface of the NCD film and on the worn surface of the Si_3N_4 ball after 60000 cycles of sliding at 8 Hz, 2 N load.

The peaks shown by arrows in Figure 3.22 can be identified as diamond peak (1332 cm^{-1}), graphite (1355 and 1540 cm^{-1} corresponding to D and G

bands) and to trans-polyacetylene peaks (1478 cm^{-1}). Unfortunately, clear distinguishing is impossible, however the present data allow us to conclude that the chemical composition of materials on the ball to some extent is similar to that of the NCD films. In other words, a transfer layer is formed on the ball surface. The transfer layer is not continuous as can be seen on the image taken by SEM. With regard to the discussion of sudden spikes observed in COF vs cycles curves (see sections 3.1.1 and 3.1.2), periodical abrupt delamination of the transfer layer on the ball surface probably causes changes in the COF value.

3.2 Wear behavior of the DLC films

Me-C:H (metal doped DLC) DLC films were prepared by means of the Plasma Enhance Chemical Vapor Deposition (PECVD) method on PLATIT $\pi 80$ unit. Prior to the deposition of the DLC, hard films (nanocomposite nACo (nc-AlTiN/(a-Si₃N₄)) and single layers of CrN and TiCN) were deposited on top of WC-Co substrates.

The following DLC films were studied:

- FiVic^{2®} (nACo + DLC)
- CROMVic^{2®} (CrN + DLC)
- CVic^{2®} (TiCN + DLC)

FiVic^{2®}, CROMVic^{2®} and CVic^{2®} are trademarks of Platit AG.

The thickness of the DLC layer was 1 – 1.5 μm . CROMVic^{2®} samples were used to investigate the rippling phenomenon on the DLC against the ZrO₂ balls. Tests with Al₂O₃ balls were conducted with FiVic^{2®}, CROMVic^{2®} and CVic^{2®} samples.

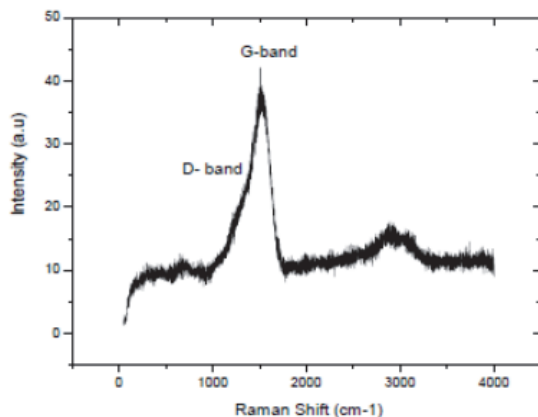


Figure 3.23 Raman spectrum of the DLC film. Reproduced from Supplementary material to [Publication IV].

Characteristic Raman spectrum of the DLC film is shown in Figure 3.23. The laser wavelength of 514.5 nm was used. The broad peak is composed of G band corresponding to the well-ordered graphite and centered at approximately

1550 cm^{-1} and D band at 1360 cm^{-1} , corresponding to disordered graphite [108]. Peaks at about 3000 cm^{-1} are attributed to the C–H bands [99].

Ripples on DLC surfaces

Rippling patterns were found after sliding tests with zirconia balls against 1 – 1.5 μm thick DLC film (CROMVic²[®]) deposited to the WC-Co substrate with the CrN interlayer. The surface roughness R_q of the DLC film is about 100 nm and the nanohardness around 20 GPa. It should be stressed that DLC films are amorphous and the roughness of the DLC layer follows the roughness of the underlying layer, *i.e.* WC-Co/CrN. This explains the relatively high roughness of the DLC films.

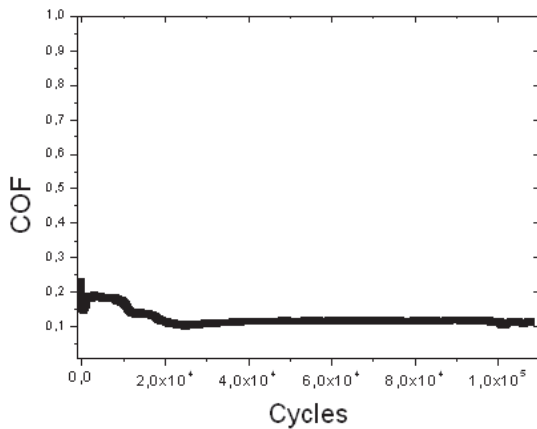


Figure 3.24 COF vs. the number of cycles for DLC film against the ZrO₂ ball. Reproduced from Supplementary material to [Publication IV].

Figure 3.24 shows the frictional behavior of the DLC films against the ZrO₂ ball. After a relatively extended run-in period (30000 cycles) the value of the COF in the steady state regime is about 0.1. Interestingly, that such a long run-in stage is in agreement with the frictional behavior of the NCD films against zirconia (see section 3.1.1).

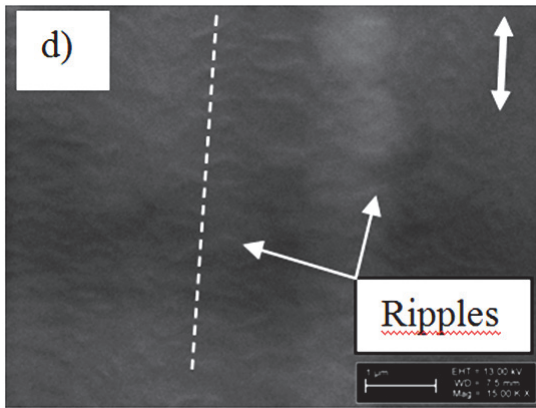


Figure 3.25 SEM image of ripples on the DLC wear scar surface after 112000 cycles at the frequency of 10 Hz. Reproduced from the Supplementary material to [Publication IV]

The SEM image of the wear scar surface (Figure 3.25) shows a ripple pattern. The ripple density is about 3.5 ripples/ μm , as measured along the line scan indicated by the white dashed line. The line scan is approximately 5 μm in length. Ripple pattern is much fainter compared to those obtained on NCD films.

Wear of the DLC film

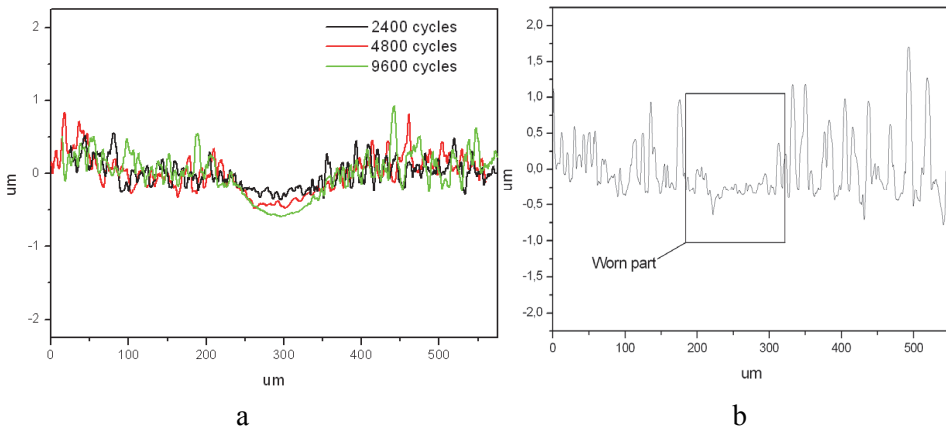


Figure 3.26 Averaged line scans of the wear scars on the DLC surface (a) and a single line scan after 2400 cycles of sliding against Si_3N_4 at 2N 2Hz (b).

Figure 3.26 shows line scans taken on the wear scars after 2400, 4800 and 9600 cycles of sliding with Si_3N_4 ball in the direction perpendicular to the sliding direction. The normal load was 2 N, sliding frequency 2 Hz. The profiles in Figure 3.26a represent the result of averaging of three line scans taken across each wear scar. Figure 3.26b represents the result of a single measurement of the wear scar after 2400 cycles of sliding. A gradual increase of

the wear scar depth due to the increase of the test duration can be seen. Wear starts with polishing of the pristine DLC surface. No clear evidence of the surface deflection (see section 3.1.3) was observed.

Correlation between the roughness parameters of the pristine DLC film and the wear scar surfaces obtained after extended sliding tests

The main purpose of this study was to understand the extent at which the surface roughness of pristine DLC films influences the frictional and wear behavior during steady-state regimes of the sliding test. Particular attention was paid to the evaluation of correlation between the roughness parameters of the clean DLC film surface and those of the wear scar surface.

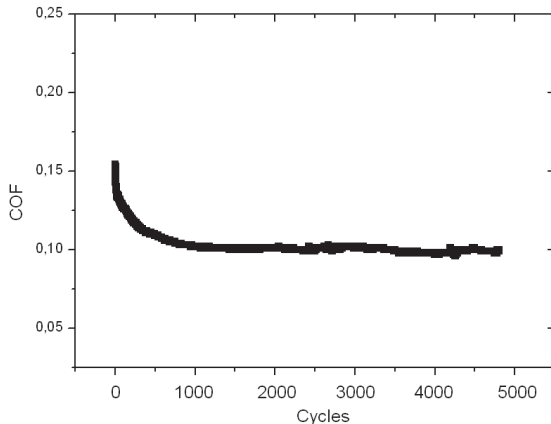


Figure 3.27 COF vs the number of cycles obtained after 4800 cycles for CromVic² samples with a 2 N load [Publication IV].

Figure 3.27 shows the COF vs the number of cycles curve measured against the Al₂O₃ ball. The run-in period (400 – 600 cycles) is followed by a steady stage with the COF value about 0.1. It is important to stress that the run-in period is remarkably shorter than that of ZrO₂ balls (*i.e.* about 30000 cycles, see Figure 3.24). Similar frictional behavior was found on the NCD film, namely a short run-in stage against the Al₂O₃ balls and a long one against the ZrO₂ balls (see Figure 3.5 and Figure 3.8 in section 3.1.1).

In total, six samples with different roughness parameters were used. The sliding tests (1 and 2 N, 2 mm, 2 Hz, room humidity, Ø 3 mm Al₂O₃) were conducted by means of a CETR[®] tribometer. The loads of 1 and 2 N were used during the sliding tests, stroke distance was 2 mm and frequency 2 Hz. Tests duration was 2400 and 4800 cycles corresponding to steady-state regimes.

The Spearman nonparametric rank correlation tests (see section 2.4 for details) was used to estimate the correlation.

Table 3.2 Coefficient of correlation R between R_a and R_z parameters of the initial DLC surface and wear scar surfaces observed after 2400 and 4800 cycles. The significant correlation is highlighted in bold [Publication IV].

Parameters	N^*	R^{**}	T^{***}	p -value
R_a clean DLC & R_z clean DLC	6	0.98561	11.6619	0.000309
R_a 2400 & R_z 2400	12	0.964918	11.6219	0.000009
R_a 4800 & R_z 4800	12	0.920671	7.4587	0.000022
R_a clean DLC & R_a 2400	12	0.460539	1.6407	0.131894
R_z clean DLC & R_a 2400	12	0.510651	1.8782	0.089795
R_a 2400 & R_a 4800	12	0.838950	4.875	0.000647
R_z 2400 & R_a 4800	12	0.814846	4.4452	0.001244
R_z clean DLC & R_z 2400	12	0.678483	2.9206	0.015284
R_z clean DLC & R_z 4800	12	0.522998	1.9404	0.081028
R_z 2400 & R_z 4800	12	0.741259	3.4923	0.005801

* N – number of observations.

** R – Spearman coefficient of correlation.

*** Critical quantity T is explained in the section 2.4.

Table 3.2 shows that the correlation between R_a and R_z is significant (see the first three lines in Table 3.2), corresponding to the three kinds of investigated surfaces, namely, initial DLC surface and wear scar surfaces created after 2400 and 4800 cycles of sliding. Among the geometrical parameters, the most sensitive ones were R_a and R_z , *i.e.* the highest correlation coefficient between these parameters for different surfaces were found. Clearly, as higher roughness means higher difference between the highest peak and the lowest valley, the correlation coefficient must be positive.

Correlation between the geometrical parameters corresponding to a different kind of a surface was observed. For instance, there is correlation between R_z measured on the wear scar after 2400 cycles and clean DLC surfaces, however no correlation was found for R_a . It indicates that R_z parameter is more sensitive than R_a . The conclusion that no correlation was found for R_a parameter can be treated as an evidence of strong modification of the pristine DLC surface during run-in. However, in spite of that finding, a correlation was found between R_a and R_z .

It is interesting that a stronger correlation was found between roughness parameters measured on the wear scars after 2400 and 4800 cycles than between those for the pristine DLC surface and the surface after 2400 cycles. These results support a conclusion that the alternation of the DLC surface between 2400 and 4800 cycles is smaller than that between the pristine DLC surface and after 2400 cycles. Finally, still there is correlation between R_z measured on the pristine DLC surface and after 4800 cycles.

The existence of such correlations can indicate that wear correlates probably with the large asperities distribution and its properties, *i.e.* parameter R_z . This suggestion can be supported by the following reasons. First, the roughness of the DLC surface is an important factor in the characterization of wear because

asperities on the coating surface are considered as centers where coating failure can occur. Second, as it was shown by Wieleba [109] for the case of polytetrafluoroethylene (PTFE) composites, the parameter R_{3z} is well correlated with the COF and linear wear. Roughness parameter R_{3z} is similar to R_z except that less extreme peaks and valleys are included into the evaluation of the parameter.

For more details see Publication IV

CONCLUSIONS

Tribological properties of carbon-based films have attracted a considerable practical and theoretical interest. Mechanical contact of two bodies leads to numerous changes taking place within the bulk of the counterbodies (for instance, cracks *etc.*), on the interfaces between the film and the substrate (for instance, delamination of the film *etc.*) and on the contact surface between the counterbodies (for instance, removal of asperities, formation of ripples and grooves, ploughing *etc.*). Wear is a dynamical process and such parameters as COF, wear rate, surface roughness and surface morphology may vary substantially during run-in, steady state and catastrophic wear.

The conclusions can be formulated as follows:

1. Wear and frictional behavior of the NCD films deposited on a Si substrate show clear dependence on the counterbody material. Tests with silicon nitride, alumina and zirconia balls used as counterbodies have shown that silicon nitride has the shortest run-in period in comparison with the other two materials. However, tests with silicon nitride balls have shown that sudden spikes of COF occur in steady state regime, as well. These spikes are likely to contribute to periodic destruction of the carbonaceous transfer layer. The formation of such layer on the surface of the Si_3N_4 ball was confirmed by Raman and SEM measurements. Alumina balls exhibit a longer run-in period but COF in the steady state regime shows no spikes. Zirconia has the longest run-in period which can be attributed to the absence of a sufficiently sp^2 -rich low-friction layer. Because Young's modulus of the zirconia is remarkably lower than that for alumina and silicon nitride, the lower contact pressure can be expected reducing formation of the carbonaceous layer. The wear rates of $2.1 \cdot 10^{-7} \text{ mm}^3/\text{N} \cdot \text{m}$ and $1.4 \cdot 10^{-7} \text{ mm}^3/\text{N} \cdot \text{m}$ were obtained for NCD films in sliding tests against Al_2O_3 and Si_3N_4 balls respectively.
2. Formation of grooves on the wear scar surfaces was observed and these peculiarities on the wear scars surface play an important role in the formation of ripple patterns. It was found that the roughness R_a of the wear scar surface (due to grooves) measured in the direction perpendicular to the sliding direction can vary considerably with the speed of the sliding and the test duration; the highest roughness was found for the tests with the highest sliding speed.
3. Deflection of the thin NCD film deposited on the Si wafer under a relatively low load was observed. This result can be explained by a plastic deformation of the Si substrate that occurred on the Si / NCD interface.
4. Rippling as a wear-related phenomenon on NCD and DLC surfaces was systematically investigated. Formation of ripple patterns is a

dynamical process. Ripple formation is preceded with a short period of initial polishing of surface asperities. Tests with Si_3N_4 balls have shown that ripples appear approximately at the middle of diamond grains. The shape and size of ripples can be affected by the formation of grooves. Ripples may compose a continuous network that may further disintegrate into separate ripples. Density and size of ripples depend substantially on the load, the sliding speed and the test duration. The exact mechanism of ripples formation remains still unclear, but several mechanisms were outlined in the present study including the influence of periodic NCD film surface deflection and surface stress-induced amorphization.

5. Correlation between geometrical parameters of pristine and worn surfaces was observed on DLC films. Namely, correlation between parameters R_z measured on clean and worn DLC surface was observed. This finding can indicate that probably wear is affected by large asperities distributed on the DLC surface.

The scientific novelty and practical importance.

Formation of ripple patterns was observed on the wear scar surfaces in reciprocating sliding tests on NCD and DLC films against ceramic counterbodies. A systematic investigation of this phenomenon was carried out for the first time.

In the scope of the current work a deflection of the NCD films deposited on the Si substrate was observed under relatively low load. This effect may have a substantial influence to the calculation of the NCD wear rates in similar tribological tests.

The aforementioned findings may have a substantial importance for the better understanding of the frictional and wear behavior of diamond and DLC films. The use of NCD and DLC films for production of MEMS and AFM tips operating on micro/nano level can be affected by deflection and rippling of films, therefore present study is of interest for industrial applications.

REFERENCES

1. Holmberg, K., Ronkainen, H., Laukanen, A., Wallin, K. Friction and wear of coated surfaces – scales, modeling and simulation of tribomechanisms. *Surface & Coating Technology*. 2007, Vol. 202, 1034 - 1049
2. Blau, P. J. On the nature of running-in. *Tribology International*. 2005, Vol. 38, 11 - 12, 1007 - 1012
3. Erdemir, A., Donnet, C. Tribology of Diamond and Diamond-Like Carbon Films: An Overview. *Wear – Materials, Mechanics and Practice*. Ed. Stachowiak, G. W. John Wiley & Sons, 2005
4. Erdemir, A., Halter, M., Fenske, G. R., Zuiker, C., Csencsits, R., Crauss, A. R., Gruen, D. M. Friction and Wear Mechanisms of Smooth Diamond Films During Sliding in Air and Dry Nitrogen. *Trib. Trans.* 1997, Vol. 40, 4, 667 - 675
5. Bhushan, B., Subramaniam, V. V., Malshe, A., Gupta, B. K., Ruan, J. Tribological properties of polished diamond films, *J. Appl. Phys.* 1993, Vol. 74, 4174 - 4180
6. Pastewka, L., Moser, S., Gumbsch, P., Moseler, M. Anisotropic mechanical amorphization drives wear in diamond. *Nature Materials*. 2011, 10, 1, 34 - 38
7. Ladon, L. Study aids for chemistry: <http://pages.towson.edu/ladon/> (accessed: 20.11.2014)
8. Liu, M., Artyukhov, V. I., Lee, H., Xu, F., Yakobson, B. I. Carbyne from the first principles: chain of C atoms, a nanorod, or a nanorope. *ACS Nano*. 2013, Vol. 7, 11, 10075 - 10082
9. Itzhaki, L., Altus, E., Basch, H., Hoz, S. Harder than diamond: determining the cross-sectional area and Young's modulus of molecular rods. *Angewandte Chemie*. 2005, Vol. 44, 45, 7432 - 7435
10. Novoselov, K. S., Geim, A. K., Morozov, S. V., Jiang, D., Zhang, Y., Dubonos, S. V., Grigorieva, I. V., Firsov, A. A. Electric field effect in atomically thin carbon films. *Science*. 2004, Vol. 306, 666 - 669
11. Kroto, H. W., Heath, J. R., O'Brien, S. C., Curl, R. F., Smalley, R. E. C₆₀: Buckminsterfullerene. *Letters to Nature*. 1985, Vol. 318, 162 - 163
12. Kroto, H. W., Allaf, A. W., Balm, S. P. C₆₀: Buckminsterfullerene. *Chem. Rev.* 1991, Vol. 91, 1213 - 1235
13. Lee, C., Wei, X., Kysar, J. W., Hone, J. Measurement of the elastic properties and intrinsic strength of monolayer graphene. *Science*. 2008, Vol. 321, 5887, 385 - 388
14. Geim, A., Novoselov, K. The rise of graphene. *Nature Materials*. 2007, Vol. 6, 3, 183 - 191
15. Balandin, A. A., Ghosh, S., Bao, W., Calizo, I., Teweldebrhan, D., Miao, F., Lau, C. N. Superior thermal conductivity of single-layer graphene. *Nano Letters*. 2008, Vol. 8, 3, 902 - 907
16. Zhang, Y., Tang, T.-T., Girit, C., Hao, Z., Martin, M. C., Zettl, A., Crommie, M. F., Shen, Y. R., Wang, F. Direct observation of a widely

- tunable bandgap in bilayer graphene. *Nature*. 2009, Vol. 459, 7248, 820 - 823
17. Melechko, A. V., Merkulov, V. I., McKnight, T. E., Guillom, M. A., Klein, K. L., Lowndes, D. H., Simpson, M. L. Vertically aligned carbon nanofibers and related structures: controlled synthesis and direct assembly. *J. Appl. Phys.* 2005, Vol. 97, 041301
 18. Smalc, M., Shives, G., Chen, G., Guggari, S., Norley, J., Reynolds, R. A. III. Thermal performance of natural graphite heat spreaders. *Proceedings of IPACK 2005*
 19. Schueller, O. J. A., Brittain, S. T., Marzolin, C., Whitesides, G. M. Fabrication and characterization of glassy carbon MEMS. *Chem. Mater.* 1997, Vol. 9, 1399 - 1406
 20. Harris, P. J. F. Fullerene-related structure of commercial glassy carbons. *Phil. Mag.* 2004, Vol. 84, 29, 3159 - 3167
 21. Shi, X. D., Kortan, A. R., Williams, J. M., Kini, A. M., Saval, B. M., Chaikin, P. M. sound Velocity and Attenuation in Single-Crystal C₆₀. *Phys. Rev. Lett.*, 1992, Vol. 68, 6, 827 - 830
 22. Yu, R. C., Tea, N., Salamon, M. B. Thermal Conductivity of single Crystal C₆₀. *Phys. Rev. Lett.* 1992, Vol. 68, 13, 2050 - 2053
 23. Manika, I., Maniks, J., Pokulis, R., Kalnacs, J., Erts, D. Polymerisation and Damage of C₆₀ Single Crystals under Low Fluency Laser Irradiation. *Phys. Stat. Sol. (a)* 2001, Vol. 188, 3, 989 - 998
 24. Manika, I., Maniks, J., Kalnacs, J. Photo-induced modifications of the structure and microhardness of fullerite C₆₀. *Hydrogen Materials Science and Chemistry of Carbon Nanomaterials*. Ed. Veziroglu, T. N. *et al.* Kluwer Academic Publishers, 2004
 25. Huffman, D. R. Solid C₆₀. *Physics Today*. 1991, Vol. 44, 11, 22 - 29
 26. Popov, M., Mordkovich, V., Perfilov, S., Kirichenko, A., Kulnitskiy, B., Perezhogin, I., Blank, V. Synthesis of ultrahard fullerite with a catalytic 3D polymerization reaction of C₆₀. *Carbon*. 2014, Vol. 76, 250 - 256
 27. Blank, V., Popov, M., Pivovarov, G., Lvova, N., Gogolinsky, K., Reshetov, V. Ultrahard and superhard phases of fullerite C₆₀: comparison with diamond on hardness and wear. *Diamond & Related Materials*. 1998, Vol. 7, 427 - 431
 28. Chen, G., Seki, Y., Kimura, H., Sakurai, S., Yumura, M., Hata, K., Futaba, D. N. Diameter control of single-walled carbon nanotube forests from 1.3-3.0 nm by arc plasma deposition. *ScientificReports*. 2014, Vol. 4, 3804-1 - 7
 29. Al-Saleh, M. H., Sundararaj, U. Review of the mechanical properties of carbon nanofiber/polymer composites. *Composites: Part A*. 2011, Vol. 42, 2126 - 2142
 30. Minus, M. L., Kumar, S. The processing, properties and structure of carbon fibers, *JOM*. 2005, Vol. 57, 52 - 58

31. Outokumpu:
<http://www.outokumpu.com/SiteCollectionDocuments/Austenitic-Standard-Cr-Ni-Grades-Data-sheet.pdf> (accessed: 15.10.2014)
32. Kimmari, E., Podgursky, V., Simunin, M., Adoberg, E., Surženkov, A., Viljus, M., Hartelt, M., Wäsche, R., Sildos, I., Kulu, P. Tribological behavior of carbon nanofibers deposited on hard nanocomposite (nc-Ti_{1-x}Al_xN)/(a-Si₃N₄) coating. *Surface & Coating Technology*. 2013, Vol. 225, 21 - 25
33. Seetharamappa, J., Yelappa, S., D'Souza, F. Carbon nanotubes: next generation of electronic materials. *Interface*. 2006, Vol. 15, 2, 23-25 - 61
34. Barron, A. R., Khan, R. M. Carbon nanotubes: opportunities and challenges. *Advanced Materials & Processes*. 2008, Vol. 166, 10, 41 - 43
35. Krishnan, A., Dujardin, E., Ebbesen, T. W., Yianilos, P. N., Treacy, M. M. J. Young's modulus of single-walled nanotubes. *Phys. Rev. B*. 1998, Vol. 58, 20, 14013 - 14019
36. Endo, M., Kim, Y. A., Hayashi, T., Nishimura, K., Matusita, T., Miyashita, K., Dresselhaus, M. S. Vapor-grown carbon fibers (VGCFs). Basic properties and their battery applications. *Carbon*. 2001, Vol. 39, 1287 - 1297
37. Kim, Y.-A., Hayashi, T., Naokawa, S., Yanagisawa, T., Endo, M. Comparative study of herringbone and stacked-cup carbon nanofibers. *Carbon*. 2005, Vol. 43, 3002 - 3039
38. Wikipedia: <http://en.wikipedia.org/wiki/Diamond> (accessed 27.10.2014)
39. Breeding, C. M., Shigley, J. E. The "Type" Classification System of Diamonds and Its Importance in Gemology. *Gems & Gemology*. 2009, Vol. 45, 2, 96 - 111
40. Field, J. E., The Properties of Natural and Synthetic Diamond, *Academic Press*, 1992
41. Field, J. E. The mechanical and strength properties of diamond. *Rep. Prog. Phys.*, 2012, Vol. 75, 126505-1 - 35
42. Gielisse, P. J. Mechanical properties of diamond, diamond films, diamond-like carbon and like-diamond materials. *Handbook of Industrial Diamonds and Diamond Films*. CRC Press, 1997
43. Ruoff, A. L., Wanagel, J. High pressures on small areas. *Science*. 1977, Vol. 198, 4321, 1037 - 1038
44. Field, J. E., Strength and fracture properties of diamond. *The Properties of Diamond*. Ed. Field, J. E. *Academic*, 1979
45. Danilenko, V. V. On the history of the discovery of nanodiamond synthesis. *Physics of the Solid State*. 2004, Vol. 46, 4, 595 - 599
46. Raty, J.-Y., Galli, G., Bostedt, C., van Buuren, T. W., Terminello, L. J. Quantum confinement and fullerene-like surface reconstructions in nanodiamonds. *Phys. Rev. Lett.* 2003, Vol. 90, 037401-1 - 4
47. Mochalin, V. N., Shenderova, O., Ho, D., Gogotsi, Y. The properties and applications of nanodiamonds. *Nature Nanotechnology*. 2012, Vol. 7, 11 - 23

48. Dolmatov, V. Y., Detonation synthesis ultradispersed diamonds: properties and applications. *Rus. Chem. Rev.* 2001, Vol. 70, 7, 607 - 626
49. Bundy, F. P., Kasper, I. S. Hexagonal diamond – a new form of carbon. *J. Chem. Phys.* 1963, Vol. 46, 9, 3437 - 3446
50. He, H., Sekine, T., Kobayashi, T. Direct transformation of cubic diamond to hexagonal diamond. *Appl. Phys. Lett.* 2002, Vol. 81, 4, 610 - 612
51. Pan, Z., Sun, H., Zhang, Y., Chen, C. Harder than diamond: superior indentation strength of wurtzite BN and lonsdaleite. *Phys. Rev. Lett.* 2009, Vol. 102, 055503-1 - 4
52. Krauss, A. R., Auciello, O., Gruen, D. M., Jayatissa, A., Sumant, A., Tucek, J., Mancini, D. C., Moldovan, N., Erdemir, A., Ersoy, D., Gardos, M. N., Busmann, H. G., Meyer, E. M., Ding, M. Q. Ultrananocrystalline diamond thin films for MEMS and moving mechanical assembly devices. *Diamond & Related Materials.* 2001, Vol. 10, 1952 - 1961
53. Field, J. E., Nicholson, E., Seward, C. R., Feng, Z. Strength, fracture and erosion properties of CVD diamond. *Phil. Trans. R. Soc. Lond. A.* 1993, Vol. 342, 261 - 275
54. Yao, C., Sun, F., Zhang, Z., Chen, M. Effect of boron concentration on adhesion and cutting performance of diamond-coated cemented carbide tools. *Key Engineering Materials*, 2008, Vol. 375-376, 138 - 142
55. Liang, Q., Stanishevsky, A., Vohra, Y. K., Tribological properties of undoped and boron-doped nanocrystalline diamond films. *Thin Solid Films*, 2008, Vol. 517, 800 - 804
56. Birrell, J., Carlisle, J. A., Auciello, O., Gruen, D. M., Gibson, J. M. Morphology and electronic structure in nitrogen-doped ultrananocrystalline diamond. *Appl. Phys. Lett.* 2002, Vol. 81, 12, 2235 - 2237
57. Shen, L., Chen, Z. A study of mechanical properties of pure and nitrogen-doped ultrananocrystalline diamond films under various loading conditions. *International Journal of Solids and Structures.* 2009, Vol. 46, 811 - 823
58. Grischke, M., Hieke, A., Morgenweck, F., Dimigen, H. Variation of the wettability of DLC coatings by network modifications using silicon and oxygen. *Diamond & Related Materials.* 1998, Vol. 7, 454 - 458
59. Robertson, J. Depositions and properties of diamond-like carbons. *MRS Proceedings.* 1998, Vol. 555, 291
60. Voevodin, A. A., Phelps, A. W., Zabinski, J. S., Donley, M. S. Friction induced phase transformation of pulsed laser deposited diamond-like carbon. *Diamond & Related Materials.* 1996, Vol. 5, 11, 1264 - 1269
61. Platit: http://issuu.com/platit/docs/coating_guide_ev4_preview (accessed 16.10.2014)
62. Yang, Y. L., D'Evelyn, M. P. Theoretical studies of clean and hydrogenated diamond (100) by molecular mechanics. *J. Vac. Sci. Technol. A.* 1992, Vol. 10, 978 - 984
63. Harris, S. J., Goodwin, D. G. Growth on the Reconstructed Diamond (100) Surface. *J. Phys. Chem.* 1993, Vol. 97, 23 - 28

64. Sumiya, H., Toda, N., Satoh, S. Mechanical properties of synthetic type IIa diamond crystal, *Diamond & Related Materials*. 1997, Vol. 6, 12, 1841 - 1846
65. Gersten, J. I., Smith, F. W. *The Physics and Chemistry of Materials*. Wiley, New York, 2001
66. Nye, J. F. Physical properties of crystals. *Oxford University Press*. 1985
67. Podgursky, V. *Ab initio* calculations of elastic properties of isotropic and oriented Ti_{1-x}Al_xN hard coatings. *J. Phys. D: Appl. Phys.* 2007, Vol. 40, 4021 - 4026
68. Grimsditch, M. H., Ramdas, A. K. Brillouin scattering in diamond. *Phys. Rev. B*. 1975, Vol. 11, 8, 3139 - 3148
69. Blackslee, O. L., Proctor, D. G., Seldin, E. J., Spence, G. B., Weng, T. Elastic constants of compression-annealed pyrolytic graphite. *J. Appl. Phys.* 1970, Vol. 41, 8, 3373 - 3382
70. Hird, J. R., Field, J. E. A wear mechanism map for the diamond polishing process. *Wear*. 2005, Vol. 258, 18 - 25
71. van Bowelen F. M., Field, J. E., Brown, L. M. Electron microscopy analysis of debris produced during diamond polishing, *Phil. Mag.* 2003, Vol. 83, 7, 839 - 855
72. Tolkowsky, M. Research on the abrading, grinding or polishing of diamonds. *D.Sc. thesis, City and Guilds Colledge, University of London*
73. van Bowelen, F. M., van Enckevort, W. J. P. A simple model to describe the anisotropy of diamond polishing, *Diamond & Related Material*. 1999, Vol. 8, 840 - 844
74. Hird, J. R., Field, J. E. Diamond polishing. *Proc. R. Soc. Lond. A*. 2004, Vol. 460, 3547 - 3568
75. El-Dasher, B. S., Gray, J. J., Tringe, J. W. Crystallographic anisotropy of wear on a polycrystalline diamond surface. *Appl. Phys. Lett.* 2006, Vol. 88, 24915
76. Wiora, M., Brühne, K., Flöter, A., Gluche, P., Willey, T. M., Kucheyev, S. O., van Buuren, A. W., Hamza, A. V., Biener, J., Fecht, H.-J. Grain size dependent mechanical properties of nanocrystalline diamond films grown by hot-filament CVD. *Diamond & Related Materials*. 2009, Vol. 18, 927 - 930
77. Wiora, M., Sadrifar, N., Brühne, K., Gluche, P., Fecht, H.-J. Correlation of microstructure and tribological properties of dry sliding nanocrystalline diamond coatings. *3rd European Conference on Tribology*. 2011
78. Erdemir, A., Fenske, G. R., Krauss, A. R., Gruen, D. M., McCauley, T., Csencsits, R. T., Tribological properties of nanocrystalline diamond films. *Surface & Coating Technology*. 1999, Vol. 120 - 121, 565 - 572
79. Erdemir, A., Bindal, C., Fenske, G. R., Wilbur, P. Tribological properties of hard carbon films on zirconia ceramics. *Tribol. Trans.* 1996, Vol. 39, 735 - 741

80. Erdemir, A., Donnet, C. Tribology of diamond-like carbon films: recent progress and future prospects. *J. Phys. D: Appl. Phys.* 2006, Vol. 39, 311 - 327
81. Memming, R., Tolle, H. J., Wierenga, P. E. Properties of polymeric layers of hydrogenated amorphous carbon produced by a plasma-activated chemical vapour deposition process II: Tribological and mechanical properties. *Thin Solid Films.* 1986, Vol. 143, 31 - 41
82. Grill, A. Review of the tribology of diamond-like carbon. *Wear.* 1993, Vol. 168, 143 - 153
83. Miyamoto, T., Kaneko, R., Miyake, S. Tribological characteristics of amorphous carbon films investigated by point contact microscopy. *J. Vac. Sci. Technol. B.* 1991, Vol. 9, 1336
84. Grassie, S. L. Rail corrugation: characteristics, causes and treatments. *J. Rail and Rapid Transit.* 2009, Vol. 223, 6, 581 - 596
85. Shi, W., Dong, H., Bell, T. Tribological behaviour and microscopic wear mechanisms of UHMWPE sliding against thermal oxidation-treated Ti6Al4V. *Materials Science and Engineering A.* 2000, Vol. 291, 27 - 36
86. Leung, O. M., Goh, M. C. Orientational ordering of polymers by atomic force microscope tip-surface interaction. *Science.* 1992, Vol. 255, 5040, 64 - 66
87. Socoliuc, A., Gnecco, E., Bennewitz, R., Meyer, E. Ripple formation induced in localized abrasion. *Phys. Rev. B.* 2003, Vol. 68, 11, 115416-1 - 4
88. Such, B., Krok, F., Szymonski, M. AFM tip-induced ripple pattern on AlIn-BV semiconductor surfaces. *Applied Surface Science.* 2008, Vol. 254, 5431 - 5434
89. Filippov, A. E., Popov, V. L., Urbakh, M. Mechanism of wear and ripple formation induced by the mechanical action of an atomic force microscope tip. *Phys. Rev. Lett.* 2011, Vol. 106, 025502-1 - 4
90. Datta, D., Bhattacharyya, S. R., Chini, T. K., Sanyal, M. K. Evolution of surface morphology of ion sputtered GaAs(100). *Nucl. Instr. And Meth. in Phys. Res. B.* 2002, Vol. 193, 596 - 602
91. Datta, D., Wu, Y.-R., Wang, Y. L. Real-time observation of ripple structure formation on a diamond surface under focused ion-beam bombardment. *Phys. Rev. B.* 2001, Vol 63, 12, 125407-1 - 6
92. Brookes, E. J., Greenwood, P., Xing, G. Friction and wear of synthetic diamond. *Int. J. Refract. Metals Hard Mater.* 1999, Vol. 17, 69 - 77
93. Vandenbulcke, L., De Barros, M. I. Deposition, structure, mechanical properties and tribological behavior of polycrystalline to smooth fine-grained diamond coatings. *Surface & Coating Technology.* 2001, Vol. 146 - 147, 417 - 424
94. Gadelmawla, E. S., Koura, M. M., Maksoud, T. M. A., Elewa, I. M., Soliman, H. H., Roughness parameters. *Journal of Materials Processing Technology.* 2002, Vol. 123, 133 - 145
95. Hill, T., Lewicki, P. Statistics: methods and applications. *StatSoft*, 2007

96. Herlinger, J. Sp³'s experience using Hot Filament CVD Reactors to grow diamond for an expanding set of applications. *Presentation at ICNDST*, 2004
97. May, P. W. Diamond thin films: a 21st-century material. *Phil. Trans. R. Soc. Lond. A*. 2000, Vol. 358, 473 - 495
98. Ferrari, A. C., Robertson, J. Raman spectroscopy of amorphous, nanostructured, diamond-like carbon, and nanodiamond. *Phil. Trans. R. Soc. Lond. A*. 2004, Vol. 362, 2477 - 2512
99. Ferrari, A. C., Robertson, J. Resonant Raman spectroscopy of disordered, amorphous and diamondlike carbon. *Phys. Rev. B*. 2001, Vol. 64, 7, 075414-1 - 13
100. Chromic, R. R., Winfrey, A. L., Lüning, J., Nemanich, R. J., Wahl, K. J. Run-in behavior of nanocrystalline diamond coatings studied by in situ tribometry. *Wear*, 2008, Vol. 265, 477 - 489
101. Bhusan, B., Li, X. Micromechanical and tribological characterization of doped single-crystal silicon and polysilicon films for microelectromechanical systems devices. *Journal of Materials Research* 1997, Vol. 12, 1, 54 - 63
102. Boyd, E. J., Uttamchandani, D. Measurement of the Anisotropy of Young's Modulus in Single-Crystal Silicon. *Journal of Microelectromechanical Systems*. 2012, Vol. 21, 1, 243 - 249
103. Gan, L., Ben-Nissan, B., Ben-David, A. Modelling and finite element analysis of ultra-microhardness indentation of thin films. *Thin Solid Films*. 1996, Vol. 290 - 291, 362 - 366
104. Ericson, F., Schweitz, J.-A. Micromechanical fracture strength of silicon. *J. Appl. Phys.* 1990, Vol. 68, 11, 5840 - 5844
105. Michler, J., von Kaenel, Y., Stiegler, J., Blank, E. complementary application of electron microscopy and micro-Raman spectroscopy for microstructure, stress, and bonding defect investigation of heteroepitaxial chemical vapor deposited diamond films. *J. Appl. Phys.* 1998, Vol. 83, 1, 187 - 197
106. Michler, J., Mermoux, M., von Kaenel, Y., Haouni, A., Lucazeau, G., Blank, E. Residual stress in diamond films: origins and modeling. *Thin solid films*. 1999, Vol. 357, 189 - 201
107. Holmberg, K., Laukainen, A., Ronkainen, H., Wallin, K., Varjus, S., Koskinen, J. Tribological contact analysis of a rigid ball sliding on a hard coated surface. Part II: Material deformations, influence of coating thickness and Young's modulus. *Surface & Coating Technology*. 2006, Vol. 200, 3810 - 3823
108. Robertson, J. Diamond-like amorphous carbon. *Materials Science & Engineering R*. 2002, Vol. 37, 129 - 281
109. Wieleba, W. The statistical correlation of the coefficient of friction and wear rate of PTFE composites with steel counterface roughness and hardness. *Wear*. 2002, Vol. 252, 719 - 729

ACKNOWLEDGEMENTS

I would like to express my special thanks to my supervisor, Vitali Podgurski, for his strong support and guidance which made this work possible. I also would like to thank Maksim Antonov and Valdek Mikli for helping and supporting me in testing and conducting of profilometric and AFM measurements, and all other colleagues from Tallinn University of Technology who helped and advised me in the course of this work.

This thesis was written with support of institutional research funding IUT19-29 and projects ETF 8696 and ETF 7442 of the Estonian Ministry of Education and Research

My special thanks to my parents for their support and patience, without it this work would hardly be possible.

ABSTRACT

Morphological changes on diamond and DLC films during sliding wear

Outstanding properties of the diamond and diamond-like carbon (DLC) films like high hardness, chemical inertness, wear resistance and low coefficient of friction enable a number of industrial applications.

The wear and frictional behavior of the diamond and DLC films is affected by different factors including counterbody and substrate materials, load, sliding speed, and distance. Consequently, wear mechanisms depend on the mentioned factors as well, and evolution of surface morphology on the wear scars surface during sliding can be attributed to particular wear mechanisms.

The wear and frictional behavior of the nanocrystalline diamond (NCD) and DLC films against different ceramic materials under reciprocating sliding conditions was investigated in the thesis. The NCD and DLC films were deposited on silicon and WC-Co substrates, correspondingly and characterized by Raman spectrometry, AFM, SEM and profilometry.

The mechanisms of sliding wear of NCD and DLC films were studied and the ripple patterns formed during sliding were systematically investigated. For the first time the dynamics of morphological changes of NCD films during sliding wear was studied.

Amorphization of the NCD films surface under mechanical loading was observed.

A deflection of an NCD film deposited on a single-crystal silicon substrate was observed. The deflection can be explained with the formation of dislocation network on the Si/diamond interface due to thermal stresses related to CVD process.

It was found that amorphization and deflection of the NCD films correlate with the formation of ripple patterns on the wear scars. The manifestation of the ripple patterns depends on the sliding test parameters, namely on the load and the sliding distance.

Morphological changes on the DLC film surface during sliding were studied. Correlation was found between R_a and R_z parameters of the pristine and wear scars surfaces of the DLC films. The large asperities on the DLC film surface may play an important role in the frictional behavior during the steady stage regime of sliding.

KOKKUVÕTE

Morfoloogilised muutused teemant- ja teemandilaadsetel pinnitel liugkulumisel

Teemant- ja teemandilaadsete pinnete suurepäraseks omadused nagu suur kõvadus, keemiline inertsus, kulumiskindlus ja madal hõõrdetegur võimaldavad nende kasutamist erinevates tööstusrakendustes.

Teemant- ja teemandilaadsete pinnete kulumine on mõjutatud mitmesuguste tegurite poolt, kaasa arvatud vastaskeha ja alusmaterjal, koormus, liikumiskiirus ning -distsants. Järelikult, ka kulumismehhanismid sõltuvad ülalnimetatud faktoritest ja kulumisjälje pinna morfoloogia muutus liuge käigus on erinevatele kulumismehhanismidele erinev.

Doktoritöös on uuritud nanokristalse teemantpinde (*nanocrystalline diamond*, NCD) ja teemandilaadse süsinikpinde (*diamond-like carbon*, DLC) kulumis- ja hõõrdumiskäitumist paaris erinevate keraamikamaterjalidega. Pinned olid sadestatud räni ja WC-Co kõvasulami alustele. Pinnete karakteriseerimiseks kasutati Raman spektroskoopiat, AFM, SEM ja profilomeetria.

Uuriti teemantpinde ja teemandilaadse süsinikpinde kulumise mehhanisme. Esmakordselt uuriti süstemaatiliselt pinde pinna morfoloogiliste muutuste dünaamikat – säbarlainetumustrite teket NCD ja DLC pinnitel liuge käigus.

NCD pinnete korral täheldati mehaanilise koormuse all struktuuri amorfisatsiooni. Lisaks selgitati välja, et NCD pinnete läbipaine liuge käigus on suure tõenäosusega seotud NCD pinnete sadestumisprotsessiga.

Täheldati monokristalse räni alusele sadestatud NCD pinde läbipaine. Seda saab seletada dislokatsioonide võrgu moodustumisega sadestumise ajal Si/teemant piiril termopinge tõttu.

Leiti, et NCD pinnete amorfisatsioon ja läbipaine korreleeruvad säbarlainetumustrite kujunemisega kulumisjälgedes. Säbarlainetumustrite ilming sõltub eelkõige kulumise parameetritest, nimelt koormusest ja distantsist.

DLC pinnete morfoloogilised muutused liuge käigus on seotud eelkõige pinde algkaredusega. Ilmnes korrelatsioon pinde pinna algkareduse ja kulumisjälgede pinnakareduse parameetrite R_a ja R_z vahel. DLC suured pinnakonarused võivad mängida olulist rolli hõõrdekäitumisel liugpüskulumise režiimis.

APPENDICES

Curriculum vitae

1. Personal data

Name Andrei Bogatov
Date and place of birth 6.11.1982, Tallinn, Estonia
E-mail address andrei.bogatov@mail.ru

2. Education

Educational institution	Graduation year	Education (field of study / degree)
Tallinn University of Technology (TUT)		Materials engineering / Ph.D. studies
TUT	2008	Product development / M.Sc. degree
TUT	2005	Product development / B.Sc. degree
Juhkentali High School	2000	Secondary education

3. Language skills

Language	Level
Russian	Mother tongue
English	Average
Estonian	Average
German	Basic skills

4. Professional employment

Period	Organization	Position
2014-...	TUT, Department of Materials Engineering	Early-stage researcher
2013	Teamwork Engineering OÜ	Design engineer / project manager
2012 – 2013	The First Linen Company OÜ	Sales manager
2005 – 2012	JOT Automation OÜ	Design engineer
2005	Pütz Prozessautomatisierung und Systemtechnik GmbH, Germany	Design engineer (trainee)
2003 – 2004	BLRT IK OÜ	Design engineer
2003	Elmas OÜ	Technologist / CNC lathe operator (trainee)
2001 – 2002	Kristmet OÜ	CNC gas-cutting machines programmer

5. Research activity

Duration	Project name	Project No.
2014	Multi-scale structured ceramic-based composites for extreme applications	IUT19-29
2011 - 2013	Evaluation and optimization of Diamond Like Carbon coating properties	ETF 8696
2010	Optimisation of tribological properties of PVD hard coatings	ETF 7442

6. Main area of scientific work

T155 Coatings and surface treatment

Elulookirjeldus

1. Isikuandmed

Nimi

Andrei Bogatov

Sünniaeg ja -koht

6.11.1982, Tallinn, Eesti

E-posti aadress

andrei.bogatov@mail.ru

2. Hariduskäik

Õppeasutus	Lõpetamise aasta	Haridus (eriala / kraad)
Tallinna Tehnikaülikool (TTÜ)		Materjalitehnika / doktoriõpe
TTÜ	2008	Tootearendus / magistrikraad
TTÜ	2005	Tootearendus / bakalaureusekraad
Juhkentali Gümnaasium	2000	Keskharidus

3. Keelteoskus

Keel	Tase
Vene	Emakeel
Inglise	Kesktase
Eesti	Kesktase
Saksa	Algtase

4. Teenistuskäik

Töötamise aeg	Tööandja	Ametikoht
2014 – ...	TTÜ, Materjalitehnika instituut	Nooremteadur
2013	Teamwork Engineering OÜ	Konstruktor / projektijuht
2012 – 2013	The First Linen Company OÜ	Müügijuht
2005 – 2012	JOT Automation OÜ	Konstruktor
2005	Pütz Prozessautomatisierung und Systemtechnik GmbH, Saksamaa	Konstruktor (praktikant)
2003 – 2004	BLRT IK OÜ	Konstruktor
2003	Elmas OÜ	Tehnoloog / CNC treipingi operaator (praktikant)
2001 – 2002	Kristmet OÜ	CNC gaasilõikeseade programmeerija

5. Teadusprojektid

Kestus	Teema	Projekti Nr.
2014	Mitmeastmeliselt struktureeritud keraamika-baasil komposiitmaterjalid kasutamiseks ekstreemtingimustes	IUT19-29
2011 - 2013	Teemantlaadse süsiniku pinde omaduste hindamine ning optimeerimine	ETF 8696
2010	Aurustussadestatud kõvapinnete triboloogia omaduste optimeerimine	ETF 7442

6. Urimisteema

T155 Pinded ja pinnatehnoloogia

Publications

- Publication I. Podgursky, V., Hantschel, T., Bogatov, A., Kimmari, E., Antonov, M., Viljus, M., Mikli, V., Tsigkourakos, M., Vandevorst, W., Buijnsters, J. G., Raadik, A. T., Kulu, P. Rippling on wear scar surfaces of nanocrystalline diamond films after reciprocating sliding against ceramic balls. *Tribology letters* 2014, Vol. 55, 3, 493-503

Rippling on Wear Scar Surfaces of Nanocrystalline Diamond Films After Reciprocating Sliding Against Ceramic Balls

V. Podgursky · T. Hantschel · A. Bogatov · E. Kimmari ·
M. Antonov · M. Viljus · V. Mikli · M. Tsigkourakos ·
W. Vandervorst · J. G. Buijnsters · A. T. Raadik · P. Kulu

Received: 10 December 2013 / Accepted: 12 July 2014
© Springer Science+Business Media New York 2014

Abstract The formation of nanoscopic ripple patterns on top of material surfaces has been reported for different materials and processes, such as sliding against polymers, high-force scanning in atomic force microscopy (AFM), and surface treatment by ion beam sputtering. In this work, we show that such periodic ripples can also be obtained in prolonged reciprocating sliding against nanocrystalline diamond (NCD) films. NCD films with a thickness of 0.8 μm were grown on top of silicon wafer substrates by hot-filament chemical vapor deposition using a mixture of methane and hydrogen. The chemical structure, surface

morphology, and surface wear were characterized by Raman spectroscopy, scanning electron microscopy (SEM), and AFM. The tribological properties of the NCD films were evaluated by reciprocating sliding tests against Al_2O_3 , Si_3N_4 , and ZrO_2 counter balls. Independent of the counter body material, clear ripple patterns with typical heights of about 30 nm induced during the sliding test are observed by means of AFM and SEM on the NCD wear scar surfaces. Although the underlying mechanisms of ripple formation are not yet fully understood, these surface corrugations could be attributed to the different wear phenomena, including a stress-induced micro-fracture and plastic deformation, a surface smoothing, and a surface rehybridization from diamond bonding to an sp^2 configuration. The similarity between ripples observed in the present study and ripples reported after repeated AFM tip scanning indicates that ripple formation is a rather universal phenomenon occurring in moving tribological contacts of different materials.

Electronic supplementary material The online version of this article (doi:10.1007/s11249-014-0379-z) contains supplementary material, which is available to authorized users.

V. Podgursky (✉) · A. Bogatov · E. Kimmari · M. Antonov ·
P. Kulu
Department of Materials Engineering, Tallinn University of
Technology, 19086 Tallinn, Estonia
e-mail: vitali.podgurski@ttu.ee

T. Hantschel · M. Tsigkourakos · W. Vandervorst
IMEC, 3001 Louvain, Belgium

M. Viljus · V. Mikli
Center of Materials Research, Tallinn University of Technology,
Ehiatajate tee 5, 19086 Tallinn, Estonia

M. Tsigkourakos · W. Vandervorst
Instituut voor Kern- en Stralingsfysica, KU Leuven, Louvain,
Belgium

J. G. Buijnsters
Department of Materials Engineering, KU Leuven, Kasteelpark
Arenberg 44, 3001 Louvain, Belgium

A. T. Raadik
Department of Materials Science, Tallinn University of
Technology, Ehiatajate tee 5, 19086 Tallinn, Estonia

Keywords Nanocrystalline diamond films · Friction ·
Wear · Sliding · Ripples

1 Introduction

Chemical inertness, low wear rate under high load, and generally low coefficient of friction (COF) make nanocrystalline diamond (NCD) an important engineering material for tribological applications, such as protective tool coatings [1], microelectromechanical systems (MEMS) [2], and scanning spreading resistance microscopy (SSRM) tips [3]. The NCD films are generally grown in hydrogen-rich (>90 %) and carbon-lean (<6 %) CVD growth environments and have diamond grain sizes up to

about 100–200 nm depending on the primary nucleation of diamond particles. Generally, NCD contains very low-to-moderate amounts of sp^2 -bonded carbon trapped at defects or grain boundaries, but NCD grown with high methane concentration may contain as much as 50 % non-diamond carbon [4].

In the past, much research attention was focused on the understanding of friction and wear mechanisms on diamond films [5–18]. The tribological properties of CVD diamond films depend on intrinsic factors (the ratio of sp^3/sp^2 hybridization of carbon bonds, hydrogen and impurities concentration, surface roughness, etc.) and extrinsic factors (test conditions and counter material). The polishing of diamond was intensively investigated experimentally and theoretically [5, 12–18]. The anisotropy of the mechanical properties of single-crystal diamond gives rise to diamond surface failure. The diamond polishing involves two- and three-body wear processes, and it proceeds differently along the ‘hard’ and ‘soft’ directions [14–18]. Along the ‘hard’ direction, micro-fracture is the predominant wear mechanism [14–16]. Scanning tunneling microscopy (STM) images of diamond surfaces polished in the ‘hard’ directions showed nanoscale ‘hill and valley’-type structures [18]. On the other hand, it appears that a structural transformation is responsible for material removal for the ‘soft’ direction polishing, since abrasive wear can be ruled out [14]. It was suggested that via the large shear stress present at the diamond–counterbody interface, it becomes energetically more favorable for the diamond bonding to rehybridize to an sp^2 configuration [15, 16]. Crystallographic anisotropy of wear was found on polycrystalline diamond surfaces as well [13]. The structure of polycrystalline diamond films plays an important role during the run-in period in sliding wear tests; namely, surface asperities interlock with counterbody surface asperities, resulting in material fracture followed by a micro-plowing and self-polishing wear mechanisms on the diamond film surfaces [6, 11, 19]. The elimination of the sp^2 -enriched amorphous layer from the contact zone occurs due to mechanical removal or etching of by ambient oxygen [5, 20]. In conclusion, wear is a load- and velocity-dependent process [5, 14]; the frictional behavior of diamond films depends on surface morphology [6, 8, 11], diamond grains orientation [12, 13], formation of an amorphous carbonaceous lubricating layer due to stress-induced mechanochemical amorphization [5, 7, 8, 10, 11, 14], and passivation of dangling carbon bonds produced during sliding by species from ambient environment [11, 21–23].

The formation of periodic surface ripples on compositionally diverse materials was reported in the literature for different surface processing methods. The ripple formation on ultra-high molecular weight polyethylene (UHMWPE) surfaces during cyclic loading in a sliding test against

Ti₆Al₄V was explained by the stress-induced preferential orientation of the crystalline lamellae in the UHMWPE and a micro-fatigue wear mode [24]. Nanoscopic ripple patterns were found after repeated scratching by an atomic force microscopy (AFM) tip on different materials, including polymers [25], ionic crystals and metals [26], and semiconductors [27]. It was suggested by Filippov et al. [28] that surface corrugations and frictional stress produced by the AFM tip play a decisive role in the formation of such a ripple morphology. Nanometric rippled surface patterns can also be produced via erosion by ion beam sputtering at off-normal incidence of targets, including semiconductors, metals, and single-crystal diamond [29–32].

Our paper reports ripple patterns on wear scar surfaces of NCD films formed under reciprocating sliding test conditions. Although ripple patterns were found among other morphological features observed on the wear scar surfaces of diamond films rubbed against cubic boron nitride (cBN) under stick–slip motion [33] and against diamond [34], no systematic studies of the formation and the nanoscale surface topography of ripples on NCD were carried out so far. The wear and friction of NCD films with a significant fraction of sp^2 -bonded carbon grown from relatively high methane concentrations are investigated in this study. The surface alternation of NCD films under conditions of back-and-forth (or reciprocating) sliding friction is elucidated. Three counterbody materials with different mechanical properties, i.e., Al₂O₃, Si₃N₄, and ZrO₂, were used to conduct the tests on the NCD films under different tribological conditions.

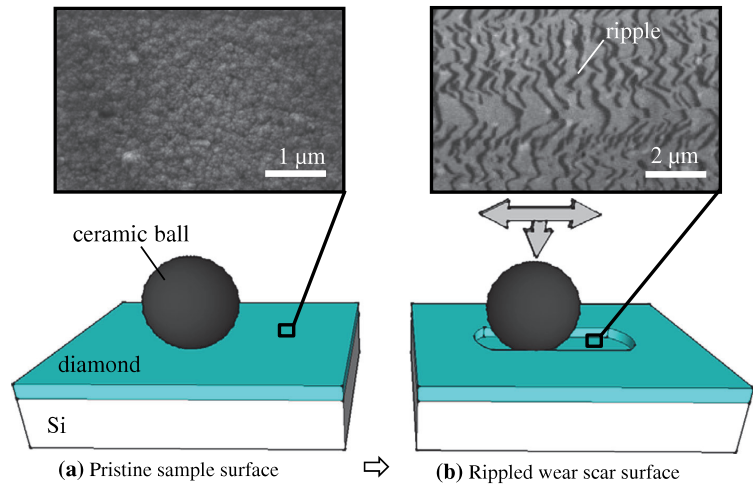
2 Experimental

NCD films were grown on 100-mm diameter (100)-oriented Si wafers by hot-filament chemical vapor deposition (HFCVD) using an sp^3 Diamond Technologies, Inc., 655 reactor in a 2.4 % CH₄/H₂ gas mixture. The substrate temperature was about 850 °C, and the chamber pressure was maintained at 6 Torr. The thickness of the NCD layers is about 0.8 μm, and the roughness R_q is about 24 nm.

Room temperature Raman spectra were recorded by using a Horiba LabRam HR 800 high-resolution spectrometer equipped with a multichannel CCD detection system in the backscattering configuration. The laser light wavelength was 532 nm, and the spectral resolution of the spectrometer was 0.5 cm⁻¹. In the case of investigation of the chemical composition on the wear scar surfaces, the spot size of the laser beam was 10 μm in diameter.

Reciprocating sliding tests (normal load 2 N, displacement amplitude 1 mm, frequency 5 Hz, relative humidity about 50 %, ball diameter Ø 3 mm) were carried

Fig. 1 Schematic drawing of **a** the reciprocating sliding test geometry and **b** the position of the ripples within the wear scar for the test with ZrO₂ ball



out by means of a CETR[®] UMT-2 tribometer. Al₂O₃, Si₃N₄, and ZrO₂ balls (surface roughness $R_a = 0.012 \mu\text{m}$) (REDHILL, Czech Republic) were used as counterbodies. According to producer provided data, the hardness and Young's modulus of the Al₂O₃, Si₃N₄, and ZrO₂ counterbodies were 1,400 HV (350 GPa), 1,400–1,700 HV (310 GPa), and 650–830 HV (195 GPa). The duration of the tests was 3,000, 9,000, and 36,000 cycles.

AFM measurements (NT-MDT Solver P47H) were performed in contact mode using Si cantilevers and tips. Scanning electron microscopy (SEM) images were taken by a Zeiss EVO MA-15 system with LaB6 cathode in secondary electron mode, applying an accelerating voltage of 10–15 kV and 6.5–8.5-mm working distance.

3 Results and Discussion

The schematic drawing in Fig. 1 illustrates the formation and position of the ripples within the wear scar during the reciprocating sliding test. The surface morphology of the as-deposited NCD film surface imaged by SEM can be classified as cauliflower-like [35] typical for NCD film growth by HFCVD under high re-nucleation conditions [36, 37]. The SEM image taken after the sliding test clearly shows ripple patterns formed transversely to the direction of the reciprocal sliding motion. These ripple patterns are discussed in more detail for different counterbody materials and cycles in the following text.

Figure 2 shows the COF versus number of cycles curves corresponding to sliding tests on the diamond films against different counterbody materials. In the case of Al₂O₃ and Si₃N₄, the COF decreases relatively fast followed by the

stabilization at a value of 0.1 after about 7,500 and 2,500 cycles, respectively. Some oscillations in the absolute value of the COF during steady-state sliding against Si₃N₄ (Fig. 2a) are observed as well, but their origin is not completely understood yet. In contrast, tests with ZrO₂ balls (Fig. 2c) demonstrate no steep descent, and eventually, no steady-state regime is reached after 36,000 cycles. To summarize, different running-in tribological behavior, particularly between the tests with ZrO₂ on one hand and Al₂O₃ and Si₃N₄ balls on the other hand, was observed.

Figure 3 shows the Raman spectra recorded on the as-deposited NCD films and within the wear scar surfaces created on the NCD films after 3,000, 9,000, and 36,000 cycles of sliding against Si₃N₄, Al₂O₃, and ZrO₂. The peaks at 522 and 976 cm⁻¹ correspond to the Si substrate, the peak at 1,332 cm⁻¹ relates to diamond, and the peaks at 1,134 and 1,478 cm⁻¹ are ascribed to the presence of *trans*-polyacetylene (*t*-PA) at the grain boundaries [38]. The peaks at 1,355 and 1,540 cm⁻¹ are the so-called D and G bands corresponding to sixfold ring breathing vibrations of *sp*² sites and the in-plane stretching of *sp*² bonds, respectively [39]. In contrast to the pristine NCD film surface, a clear decrease in the peak intensity ratios between the diamond peak and peaks corresponding to *sp*²(D,G) and *t*-PA at 1,478 cm⁻¹ is observed on the wear scar surfaces created after 3,000 cycles of sliding against Si₃N₄ and Al₂O₃, i.e., a stress-induced transition of diamond to *sp*² bonding takes place at the NCD surface (see Fig. 4). In the case of Al₂O₃, the ratios decrease even further after 9,000 cycles as well. Overall, a less remarkable alteration of the ratio value between the diamond peak and *sp*²(D,G) intensities is found for ZrO₂. The relative decrease in Raman peak intensity ratios seems to depend

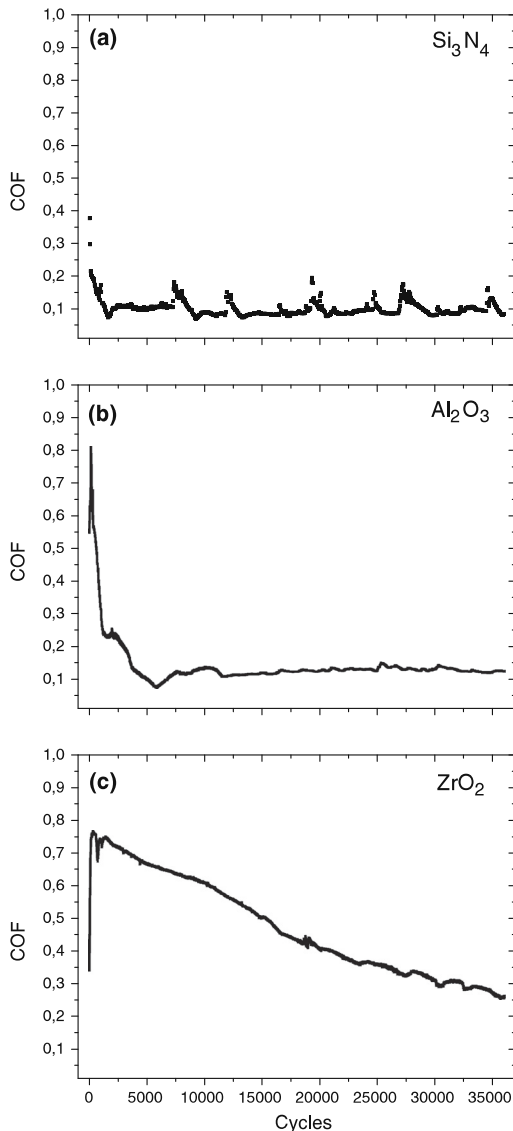


Fig. 2 The COF versus number of sliding cycles recorded on the NCD films. The test results (36,000 cycles) correspond to sliding against **a** Si_3N_4 , **b** Al_2O_3 , and **c** ZrO_2 ball counter bodies

on the mechanical properties of the ceramic counterbody material, i.e., the largest differences are detected with the hardest counter body materials (Si_3N_4 and Al_2O_3), whereas intermediate differences are recorded for the softer ZrO_2 balls, respectively.

At the beginning of each sliding test, the contact pressure is high and amorphization of diamond takes place,

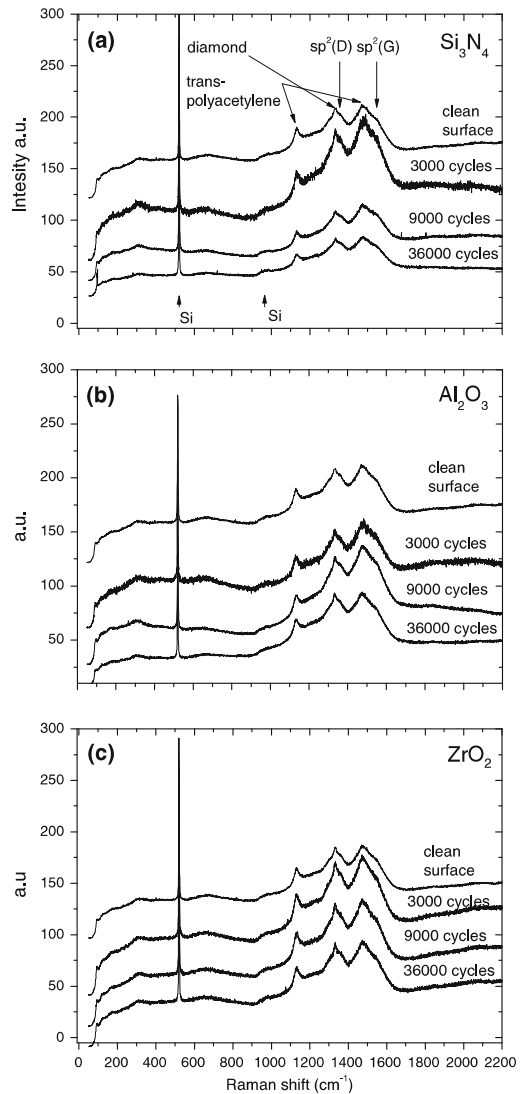


Fig. 3 Raman spectra recorded on the as-deposited NCD film and on the wear scar surfaces after 3,000, 9,000, and 36,000 cycles of sliding against **a** Si_3N_4 , **b** Al_2O_3 , and **c** ZrO_2

especially at the surface asperities [7, 8, 40]. Amorphization of the NCD film surface within the sliding wear track was claimed, for instance, by Erdemir et al. [8] and Kumar et al. [10]. Chromik et al. [9] showed that a higher sp^2 content in the NCD films results in a shorter run-in period of sliding tests. The tests in aforementioned publications [8–10] were carried out on the NCD films using different counter bodies (Si_3N_4 , sapphire, and steel), at room

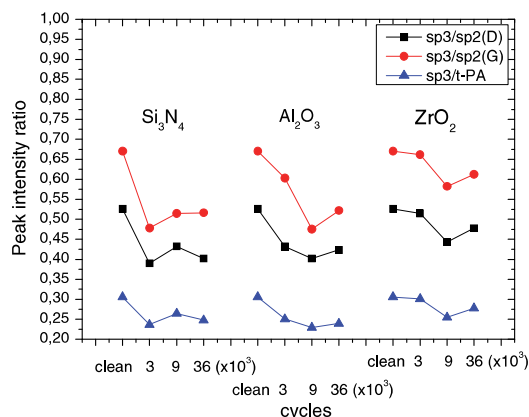


Fig. 4 The $sp^3/sp^2(G)$, $sp^3/sp^2(D)$, and $sp^3/trans$ -polyacetylene (*t*-PA peak at $1,478\text{ cm}^{-1}$) peak intensity ratios derived from the data shown in Fig. 3

temperature and under humidity conditions similar to the present study. Furthermore, the fast decrease in the COF value in the case of sliding against Si_3N_4 and Al_2O_3 (see Fig. 2a, b) could be related to a stress-induced amorphization of the NCD film surface next to a smoothening of the NCD film surface by removal of the surface asperities by fracture and micro-plowing wear. In contrast, in the case of ZrO_2 , the slow descent of the COF value might be due to the absence of a sufficiently sp^2 -rich low-friction layer. The Young's modulus of ZrO_2 is considerable lower than that of Al_2O_3 (or Si_3N_4); therefore, the contact pressure in the ZrO_2 -diamond friction pair is lower than that of the Al_2O_3 (or Si_3N_4)-diamond pair. The low hardness of ZrO_2 results in a faster abrasive wear of the ZrO_2 surface, thus decreasing the contact pressure further due to increase in contact area. In addition, the removal of an sp^2 -rich surface layer from the area of contact either mechanically or through etching by ambient oxygen [5] is possible cause of the observed trends in the evolution of the COF with ZrO_2 shown in Fig. 2c.

After extended tests (36,000 cycles) independent of the ball materials, all the peak intensity ratios shown in Fig. 4 are approximately the same as the ratio derived after 9,000 cycles, i.e., there is a saturation in the graphitization of the NCD film surface. The decrease in contact pressure reducing this graphitization and the removal of an sp^2 -rich surface layer from the area of contact either mechanically or through etching by ambient oxygen [5] are possible causes of the observed trends in the Raman spectra.

SEM images of the wear scar surfaces are shown in Fig. 5. Two main features observed on the surfaces can be classified into longitudinal grooves oriented along the wear scar and ripple patterns formed transversely to the direction

of the reciprocal sliding motion. The shape of the ripple patterns on certain wear scar surfaces alternates, i.e., although the ripples are rather equidistant, the manifestation of these corrugations varies from faintly to relatively clearly visible patterns emerging as ripple stripes, see for instance Fig. 5a. The ripple density, i.e., the number of ripples per micrometer of scan length along the sliding direction, was measured along the line scans of approximately $5\text{ }\mu\text{m}$ in length at the locations indicated by white dashed lines in Fig. 5. The ripple density varies with the ball material and sliding distance. In the case of Si_3N_4 balls, the ripple density is about 6 ripples/ μm after 3,000 and 9,000 cycles and about 4 ripples/ μm after 36,000 cycles. In the case of Al_2O_3 , the ripple density is about 6 and 3 ripples/ μm after 9,000 and 36,000 cycles, respectively. Finally, in the case of ZrO_2 , the ripple density is about 3 ripples/ μm after 36,000 cycles. The ripple density decreases with the sliding test duration for the tests with Si_3N_4 and Al_2O_3 balls. The grooves can be attributed to micro-plowing (involving diamond film, counter body, and third-body particles in-between). In contrast to tests performed with Al_2O_3 and Si_3N_4 , no polishing grooves were found on the NCD film surface after sliding against ZrO_2 .

The results of the present study show that rippling can be observed already after 3,000 cycles of sliding against Al_2O_3 and Si_3N_4 . The AFM investigation of the wear scars formed on the NCD films reveals a surface corrugation of about 30 nm in height with the ripple density about 2 ripples/ μm (Fig. 6). Note the deviation from the value of 4 ripples/ μm , measured by the SEM image analysis (Fig. 5c), which is due to aforementioned variation in the shape of ripple patterns along the surface. Rippling of the wear scar surfaces in the case of ZrO_2 was found only after 36,000 cycles (Figs. 5i, 7). In fact, using ZrO_2 as the counter body material, the process of formation of a corrugated surface can be elucidated in greater detail. After 3,000 and 9,000 cycles of sliding against ZrO_2 (Fig. 5g, h), a gradual smoothening of the wear scar surfaces takes place (i.e., darker polished contact areas are formed on the asperities of the as-deposited cauliflower-like surface of the NCD films). The contact area of the mating surfaces increases with increasing number of sliding cycles. The central part of the wear track created after 36,000 cycles looks smoother than areas close to the wear track periphery, and a transition from a flattened surface to the ripple patterns can be observed in the center of the wear scar (see Fig. 7). As a direct result of the ball geometry of the counterbody, the Hertzian contact pressure as well as shear stresses acting on the NCD film during the repetitive sliding motion will be highest in the center of the contact area. This explains the presence of the surface ripples in this central contact region. Due to the higher elastic modulus, the contact pressure is higher in the case of tests with Al_2O_3 (or Si_3N_4)

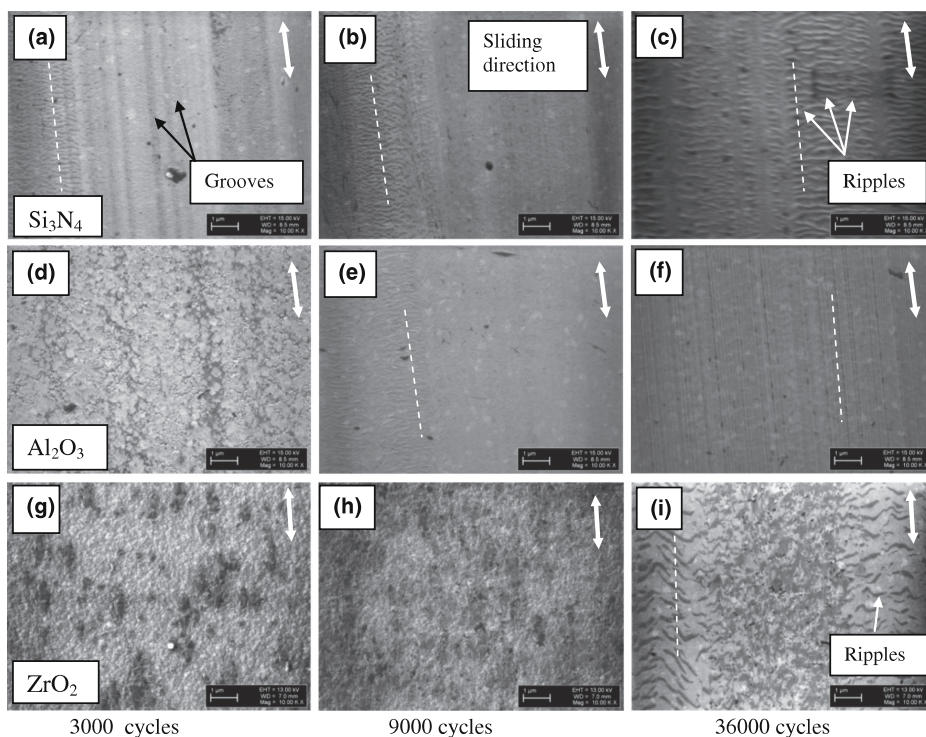


Fig. 5 SEM images of the wear scar surfaces recorded after 3,000, 9,000, and 36,000 cycles of sliding against **a–c** Si_3N_4 , **d–f** Al_2O_3 , and **g–i** ZrO_2 . The sliding direction, wear grooves, and ripple patterns are

indicated by *arrows*. The line scans of approximately 5 μm in length are shown by *white dashed lines*

balls. Therefore, ripples emerge uniformly distributed over the wear scar area in contrast to tests with ZrO_2 .

To our knowledge, no systematic research reports have addressed this phenomenon of forming ripple patterns on diamond films by a sliding movement. Commonly, the formation of surface ripples is associated with ductile materials such as polymers. Nevertheless, it is worth noting that the study by Rigney and Karthikeyan [41] based on molecular dynamical calculations predicts vorticity on the interface of two bodies within a sliding contact. The mechanisms of ripple formation on the diamond films are not yet well understood, and additional studies focusing on variations of different parameters of the tribological test (load, frequency, sliding distance, humidity, surface roughness of counterparts, diamond film chemical composition, etc.) are needed to unravel their effects on the size and shape of the ripples. However, from the results obtained, it may be inferred that in the first place, a noticeable different run-in behavior was observed for the tests with ZrO_2 , in comparison with Si_3N_4 and Al_2O_3 , and the ripple pattern shape depends on the ball materials

(Fig. 5). Therefore, the material properties of the NCD films and counter body play an important role in the sliding friction, since they determine the contact pressure, adhesion, failure mechanisms between the two contacting surfaces, etc.

The ripples are formed in surface regions enriched with amorphous carbon material. Therefore, it can be suggested that the structure and chemical composition of the amorphous layer may influence the ripple structure. In the case of sliding against Si_3N_4 , significant changes in the diamond/ sp^2 (D,G) intensity ratios were found already after 3,000 cycles, and simultaneously, the ripple patterns were observed on the wear scar surfaces. In the case of Al_2O_3 , clear ripple patterns emerge only after 9,000 cycles at the lowest values of the diamond/ sp^2 (D,G) intensity ratios. A gradual smoothening of the NCD pristine surface was observed in the case of ZrO_2 , with minor decreases in the diamond/ sp^2 (D,G) intensity ratios as compared with Si_3N_4 and Al_2O_3 , and no ripples were observed after 3,000 and 9,000 sliding cycles. Therefore, we believe that there is a correlation between the NCD surface amorphization and

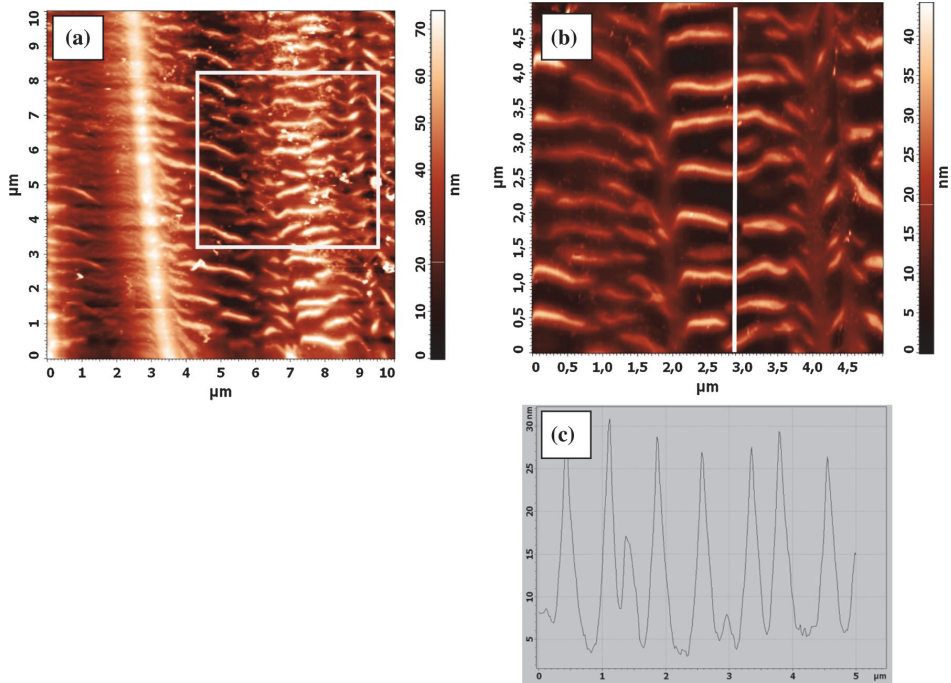


Fig. 6 AFM images recorded on the wear scar surfaces recorded after 36,000 cycles of sliding against Si_3N_4 . Surface scan areas are **a** 10×10 and **b** $5 \times 5 \mu\text{m}^2$, respectively. Line scan (**c**) was taken on the $5 \times 5 \mu\text{m}^2$ image (marked by white line)

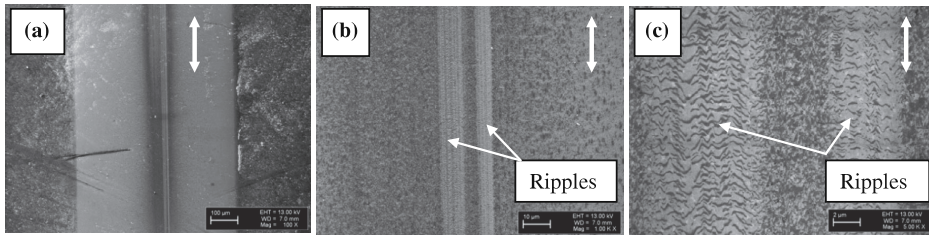


Fig. 7 SEM images at different magnifications: **a** $\times 100$, **b** $\times 1,000$, and **c** $\times 5,000$ taken from the center of the wear scar surface formed on the NCD film after 36,000 cycles of sliding against ZrO_2

the formation of ripple patterns. In addition to the alteration of the NCD surface chemical composition, probably a percolation of smoothed areas is essential for the ripple formation (compare Fig. 5d, g–i). Thus, the formation of surface corrugations or ripple patterns could be a result of stress-induced surface regions with local variations either only in sp^2 , or both sp^2 and diamond configurations.

The composite structure of the NCD films (i.e., diamond grains are embedded into a sp^2 -rich carbon matrix) and the relatively small domain sizes of both components can be important factors affecting friction and wear. Indeed, a

difference in mechanical properties between the sp^3 diamond grains and the sp^2 -rich grain boundaries could result in this peculiar behavior of ripples formation on the NCD films under continuously changing high shear stresses. Due to the high elastic modulus of diamond (or diamond grains in NCD films), the stress-induced deformation of the composite NCD structure may not be sufficient to overcome the threshold for an overall structural transition from the diamond bonding to the sp^2 configuration. However, such a phase transition may still take place at the very surface of the NCD film. On the other hand, in spite of the

high elastic modulus and fracture strength of NCD films, a plastic deformation or even fracture [33] on the NCD films surface could occur, which gives rise to an NCD surface modification and the formation of ripple patterns. In addition, the observed dependence of the ripple pattern appearance with the counterbody material indicates a different type of interaction between the various balls and the NCD film. This could result in slightly different specific sliding regimes for each of the applied counterbody materials. A stick–slip [42] type of sliding, rather than a gross–slip [43] sliding movement, could reasonably correlate with the nanoscale corrugated surface of the ripple patterns. However, in the present study, the type of sliding and failure mechanisms on the NCD surface cannot be unambiguously identified from the observed results.

A striking similarity in appearance of ripples created on the surface of different materials under remarkably different test conditions, i.e., in sliding tests with ceramic balls under 2 N normal load and in repeated scanning with a silicon tip under nanoNewtons load, allows to interpret surface rippling as a universal phenomenon. The importance of induced stress for ripple formation during AFM tip scanning reported in earlier studies [26, 28] is in line with the results of the present research. Additional reciprocating sliding tests on a diamond-like carbon (DLC) film also revealed rippling on the wear scar surface after testing with the ZrO₂ counter ball (see Supplementary Material).

4 Conclusions

The present study focuses on the friction and wear mechanisms of NCD films. A comparative analysis of the tribological behavior of NCD films is carried out using three different counter body materials, i.e., Al₂O₃, Si₃N₄, and ZrO₂, in the sliding tests. A rippling of the wear scar surfaces is clearly observed in the center of the sliding contacts independently of the counterbody materials used in the sliding tests. We suggest that shear stresses acting on the NCD films during the repetitive sliding motion between the NCD films and counterbody surfaces cause this surface corrugation. The mechanical properties of the counterparts (NCD film and ceramic ball), first of all the elastic modulus and fracture strength, and structural changes within the amorphous layer formed between the counterparts likely play a key role in the ripple pattern formation under high shear stress. We state that under particular sliding test conditions, the rippling of the wear scar surface can be considered as a characteristic material response of NCD. Moreover, the observation of surface ripples in repeated scanning by an AFM tip suggests that the rippling is an inherent feature occurring in different length-scale tribological systems.

Acknowledgments The work was supported by the Estonian Science Foundation Grant Number 8696. J.G.B. would like to thank the Executive Research Agency of the European Union for funding under the Marie Curie IEF Grant Number 272448.

References

1. Haubner, R., Kalss, W.: Diamond deposition on hardmetal substrates—comparison of substrate pre-treatments and industrial applications. *Int. J. Refract. Met. Hard Mater.* **28**, 475–483 (2010)
2. Auciello, O., Birrell, J., Carlisle, J.A., Gerbi, J.E., Xiao, X., Peng, B., Espinosa, H.D.: Materials science and fabrication processes for a new MEMS technology based on ultrananocrystalline diamond thin films. *J. Phys. Condens. Matter* **16**, R539–R552 (2004)
3. Hantschel, T., Niedermann, P., Trenkler, T., Vandervorst, W.: Highly conductive diamond probes for scanning spreading resistance microscopy. *Appl. Phys. Lett.* **76**(12), 1603–1605 (2000)
4. Butler, J.E., Sumant, A.V.: The CVD of nanodiamond materials. *Chem. Vap. Depos.* **14**, 145–160 (2008)
5. Pastewka, L., Moser, S., Gumbsch, P., Moseler, M.: Anisotropic mechanical amorphization drives wear in diamond. *Nat. Mater.* **10**, 34–38 (2011)
6. Bhushan, B., Subramaniam, V.V., Malshe, A., Gupta, B.K., Ruan, J.: Tribological properties of polished diamond films. *J. Appl. Phys.* **74**(6), 4174–4180 (1993)
7. Erdemir, A., Halter, M., Fenske, G.R., Zuiker, C., Csencsits, R., Krauss, A.R., Gruen, D.M.: Friction and wear mechanisms of smooth diamond films during sliding in air and dry nitrogen. *Tribol. Trans.* **40**, 667–675 (1997)
8. Erdemir, A., Fenske, G.R., Krauss, A.R., Gruen, D.M., McCauley, T., Csencsits, R.T.: Tribological properties of nanocrystalline diamond films. *Surf. Coat. Technol.* **120–121**, 565–572 (1999)
9. Chromik, R.R., Winfrey, A.L., Lüning, J., Nemanich, R.J., Wahl, K.J.: Run-in behavior of nanocrystalline diamond coatings studied by in situ tribometry. *Wear* **265**, 477–489 (2008)
10. Kumar, N., Panda, K., Dash, S., Popov, C., Reithmaier, J.P., Panigrahi, B.K., Tyagi, A.K., Raj, B.: Tribological properties of nanocrystalline diamond films deposited by hot filament chemical vapor deposition. *AIP Adv.* **2**, 032164-1–032164-14 (2012)
11. Holmberg, K., Ronkainen, H., Laukkanen, A., Wallin, K.: Friction and wear of coated surfaces—scales, modeling and simulation of tribomechanisms. *Surf. Coat. Technol.* **202**, 1034–1049 (2007)
12. Grillo, S.E., Field, J.E., van Bouwelen, F.M.: Diamond polishing: the dependency of friction and wear on load and crystal orientation. *J. Phys. D Appl. Phys.* **33**, 985–990 (2000)
13. El-Dasher, B.S., Gray, J.J., Tringe, J.W., Biener, J., Hamza, A.V.: Crystallographic anisotropy of wear on a polycrystalline diamond surface. *Appl. Phys. Lett.* **88**, 241915-1–241915-3 (2006)
14. Hird, J.R., Field, J.E.: Diamond polishing. *Proc. R. Soc. Lond. A* **460**, 3547–3568 (2004)
15. Van Bouwelen, F.M., Enckevort, W.J.P.: A simple model to explain the anisotropy of diamond polishing. *Diam. Relat. Mater.* **8**, 840–844 (1999)
16. Van Bouwelen, F.M., Field, J.E., Brown, L.M.: Electron microscopy analysis of debris produced during diamond polishing. *Philos. Mag.* **83**, 839–856 (2003)
17. Couto, M.S., van Enckevort, W.J.P., Seal, M.: On the mechanism of diamond polishing in the soft directions. *J. Hard Mater.* **5**, 31–47 (1994)
18. Couto, M.S., van Enckevort, W.J.P., Seal, M.: Diamond polishing mechanisms: an investigation by scanning tunnelling microscopy. *Philos. Mag. B* **69**, 621–641 (1994)

19. Abreu, C.S., Amaral, M., Fernandes, A.J.S., Oliveira, F.J., Silva, R.F., Gomes, J.R.: Friction and wear performance of HFCVD nanocrystalline diamond coated silicon nitride ceramics. *Diam. Relat. Mater.* **15**, 739–744 (2006)
20. Casari, C.S., Li Bassi, A., Ravagnan, L., Siviero, F., Lenardi, C., Piseri, P., Bongiorno, G., Bottani, C.E., Milani, P.: Chemical and thermal stability of carbyne-like structures in cluster-assembled carbon films. *Phys. Rev. B* **69**, 075422-1–075422-7 (2004)
21. Gardos, M.N., Soriano, B.L.: The effect of environment on the tribological properties of polycrystalline diamond films. *J. Mater. Res.* **5**, 2599–2609 (1990)
22. Gardos, M.N., Gabelich, S.A.: Atmospheric effects of friction, friction noise and wear with silicon and diamond. Part III. SEM tribometry of polycrystalline diamond in vacuum and hydrogen. *Tribol. Lett.* **6**, 103–112 (1999)
23. Konicsek, A.R., Grierson, D.S., Sumant, A.V., Friedmann, T.A., Sullivan, J.P., Gilbert, P.U.P.A., Sawyer, W.G., Carpick, R.W.: Influence of surface passivation on the friction and wear behavior of ultrananocrystalline diamond and tetrahedral amorphous carbon thin films. *Phys. Rev. B* **85**, 155448-1–155448-13 (2012)
24. Shi, W., Dong, H., Bell, T.: Tribological behaviour and microscopic wear mechanisms of UHMWPE sliding against thermal oxidation-treated Ti6Al4V. *Mater. Sci. Eng. A* **291**, 27–36 (2000)
25. Leung, O.M., Goh, M.C.: Orientational ordering of polymers by atomic force microscope tip-surface interaction. *Science* **255**, 64–66 (1992)
26. Socoliuc, A., Gnecco, E., Bennewitz, R., Meyer, E.: Ripple formation induced in localized abrasion. *Phys. Rev. B* **68**, 115416-1–115416-4 (2003)
27. Such, B., Krok, F., Szymonski, M.: AFM tip-induced ripple pattern on AlIn-BV semiconductor surfaces. *Appl. Surf. Sci.* **254**, 5431–5434 (2008)
28. Filippov, A.E., Popov, V.L., Urbakh, M.: Mechanism of wear and ripple formation induced by mechanical action of an atomic force microscope tip. *Phys. Rev. Lett.* **106**, 025502-1–025502-4 (2011)
29. Datta, D., Bhattacharyya, S.R., Chini, T.K., Sanyal, M.K.: Evolution of surface morphology of ion sputtered GaAs(100). *Nucl. Instr. Methods Phys. Res. B* **193**, 596–602 (2002)
30. Cuerno, R., Castro, M., Muñoz-García, J., Gago, R., Vázquez, L.: Nanoscale pattern formation at surfaces under ion-beam sputtering: a perspective from continuum models. *Nucl. Instr. Methods Phys. Res. B* **269**, 894–900 (2011)
31. Datta, A., Wu, Y.-R., Wang, Y.L.: Real-time observation of ripple structure formation on a diamond surface under focused ion-beam bombardment. *Phys. Rev. B* **63**, 125407-1–125407-6 (2001)
32. Adams, D.P., Vasile, M.J., Mayer, T.M., Hodges, V.C.: Focused ion beam milling of diamond: effects of H₂O on yield, surface morphology and microstructure. *J. Vac. Sci. Technol. B* **21**(6), 2334–2343 (2003)
33. Brookes, E.J., Greenwood, P., Xing, G.: Friction and wear of synthetic diamond. *Int. J. Refract. Metal Hard Mater.* **17**, 69–77 (1999)
34. Vandenbulcke, L., De Barros, M.I.: Deposition, structure, mechanical properties and tribological behavior of polycrystalline to smooth fine-grained diamond coatings. *Surf. Coat. Technol.* **146–147**, 417–424 (2001)
35. Castro, M., Cuerno, R., Nicoli, M., Vázquez, L., Buijnsters, J.G.: Universality of cauliflower-like fronts: from nanoscale thin films to macroscopic plants. *N. J. Phys.* **14**, 103039-1–103039-15 (2012)
36. Buijnsters, J.G., Vázquez, L.: Growth dynamics of nanocrystalline diamond thin films deposited by hot filament chemical vapor deposition: influence of low sticking and renucleation processes. *J. Phys. Chem. C* **115**, 9681–9691 (2011)
37. May, P.W., Ludlow, W.J., Hannaway, M., Heard, P.J., Smith, J.A., Rosser, K.N.: Raman and conductivity studies of boron-doped microcrystalline diamond, faceted nanocrystalline diamond and cauliflower diamond films. *Diam. Relat. Mater.* **17**, 105–117 (2008)
38. Ferrari, A.C., Robertson, J.: Raman spectroscopy of amorphous, nanostructured, diamond-like carbon, and nanodiamond. *Philos. Trans. R. Soc. Lond. A* **362**, 2477–2512 (2004)
39. Ferrari, A.C.: Robertson J Resonant Raman spectroscopy of disordered, amorphous, and diamondlike carbon. *Phys. Rev. B* **64**, 075414-1–075414-13 (2001)
40. Bowden, F.P., Freitag, E.H.: The friction of solids at very high speeds. *Proc. R. Soc. Lond. A* **248**, 350–367 (1958)
41. Rigney, D.A., Karthikeyan, S.: The evolution of tribomaterial during sliding: a brief introduction. *Tribol. Lett.* **39**, 3–7 (2010)
42. Heslot, F., Baumberger, T., Perrin, B.: Creep, stick-slip, and dry-friction dynamics: experiments and a heuristic model. *Phys. Rev. E* **49**, 4973–4988 (1994)
43. Mohrbacher, H., Celis, J.-P., Roos, J.R.: Laboratory testing of displacement and load induced fretting. *Tribol. Int.* **28**(5), 269–278 (1995)

Supplementary Information for:

Rippling on wear scar surfaces of nanocrystalline diamond films after reciprocating sliding against ceramic balls

V. Podgursky^{*1}, T. Hantschel², A. Bogatov¹, E. Kimmari¹, M. Antonov¹, M. Viljus⁵, V. Mikli⁵, M. Tsigkourakos^{2,3}, W. Vandervorst^{2,3}, J.G. Buijnsters⁴, A.T. Raadik⁶, P. Kulu¹

¹ Tallinn University of Technology, Department of Materials Engineering, 19086 Tallinn, Estonia

² IMEC, B-3001 Leuven, Belgium

³ Instituut voor Kern- en Stralingsfysica, KU Leuven, Leuven, Belgium

⁴ Department of Metallurgy and Materials Engineering, KU Leuven, Kasteelpark Arenberg 44, B-3001 Leuven, Belgium

⁵ Tallinn University of Technology, Center of Materials Research, Ehiatajate tee 5, 19086, Tallinn, Estonia

⁶ Tallinn University of Technology, Department of Materials Science, Ehiatajate tee 5, 19086, Tallinn, Estonia

*Corresponding author: vitali.podgurski@ttu.ee

- Rippling on wear scar surfaces of diamond-like carbon films after reciprocating sliding against zirconia

A diamond-like carbon (Me-C:H, metal doped DLC) sample was prepared by plasma enhanced chemical vapor deposition (PECVD) using the unit PLATIT[®] π80 (PLATIT). The DLC film was grown by dissociation of acetylene (C₂H₂) and the thickness of the DLC layer is 1.3 μm. Prior to the deposition of the DLC film, a CrN hard coating was deposited on top of the WC-Co substrate. The surface roughness R_q of the DLC film is about 100 nm and the nanohardness around 20 GPa.

Due to the composite structure of the NCD films characterized by a significant fraction of sp²-bonded carbon, DLC films are of interest for a direct comparison with these nanocrystalline diamond films. DLC possesses an amorphous structure, therefore a distinction between properties of the two materials is expected and the formation of ripple patterns during sliding tests is also of prime interest. In this respect, Fig. 1 shows the collection of data recorded on the DLC sample. The broad peak in the Raman spectrum (Fig. 1a) of the as-deposited DLC film is composed of two bands centered at approximately 1550 cm⁻¹ (G band) and 1360 cm⁻¹ (D band) [1]. Peaks at about 3000 cm⁻¹ are due to the presence of C-H bands [2]. The sliding test (10 Hz, 112000 cycles) (Fig. 1b) was done against ZrO₂. After a relatively extended running-in period (30000 cycles) the value of the COF in the steady state regime is about 0.1. Note that the SEM image at higher magnification (Fig. 1d) recorded on the wear scar surface (Fig. 1c) shows also a ripple pattern. The ripple density is about 3.5 ripples/μm, as measured along the line scan of approximately 5 μm in length at the location indicated by white dashed line in Fig. 1d.

From these results, we conclude that under particular sliding test conditions the rippling of the wear scar surface can be considered as a common property of a variety of carbon based materials including hard amorphous carbon thin films.

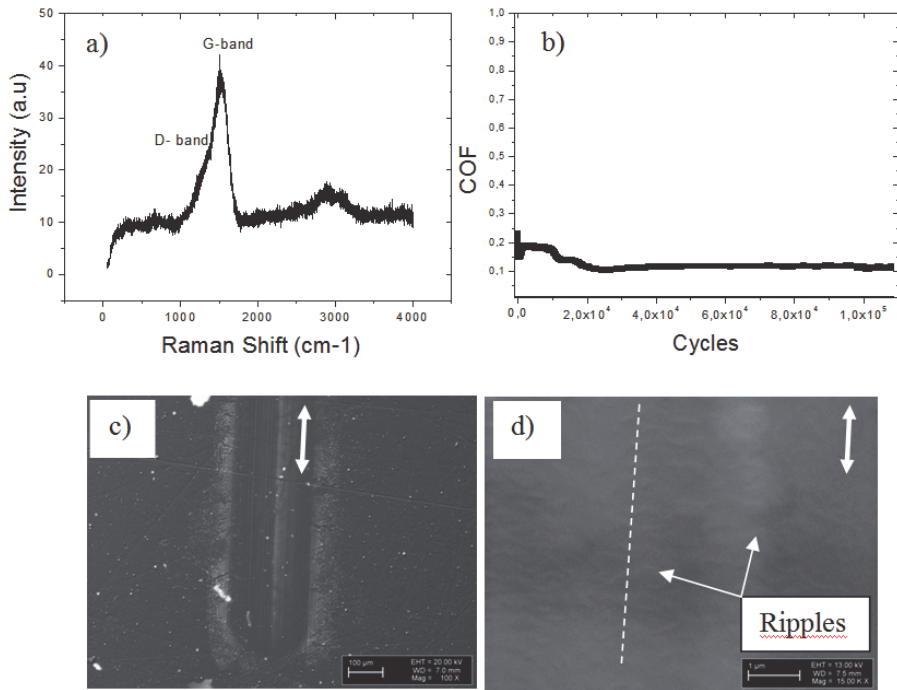


Fig. 1 (a) Raman spectrum, (b) the COF vs. number of sliding cycles and (c and d) SEM images taken at different magnifications ((c) x100 and (d) x 15000) of the wear scar surface formed on the DLC film. The line scan of approximately 5 μm in length is shown by the white dashed line and the sliding direction by the double-edged arrow

References

1. Robertson, J.: Diamond-like amorphous carbon. *Mater. Sci. Eng.* **37**, 129-281 (2002)
2. Ferrari, A.C., Robertson, J.: Resonant Raman spectroscopy of disordered, amorphous, and diamondlike carbon. *Phys. Rev. B* **64**, 075414-1- 075414-13 (2001)

Publication II. Bogatov, A., Podgursky, V., Raadik, A. T., Kamjula, A. R., Hantschel, T., Tsigkourakos, M., Kulu, P. Investigation of morphology changes on nanocrystalline diamond film surfaces during reciprocating sliding against Si₃N₄ balls. *Key Engineering Materials* 2014, Vol. 604, 126-129

Investigation of morphology changes on nanocrystalline diamond film surfaces during reciprocating sliding against Si₃N₄ balls

A. Bogatov^{1*}, V. Podgursky¹, A.T. Raadik², A. R. Kamjula¹, T.Hantschel³,
M.Tsigkourakos^{3,4}, P. Kulu¹

¹ Tallinn University of Technology, Department of Materials Engineering, 19086 Tallinn, Estonia

² Tallinn University of Technology, Department of Materials Science, Ehitajate tee 5, 19086, Tallinn, Estonia

³ Imec, Kapeldreef 75, B-3001 Leuven, Belgium

⁴ Instituut voor Kern- en Stralingsfysica, K.U. Leuven, Leuven, Belgium

Corresponding author: *andrei.bogatov@mail.ru

Keywords: nanocrystalline diamond film, surface morphology, ripples

Abstract

This paper investigates the morphological modifications of the nanocrystalline diamond (NCD) film surface under reciprocating sliding test conditions. The surface morphology was characterized by atomic force microscopy (AFM). We observed longitudinal grooves and transverse ripples which were formed during the sliding tests on the NCD film surface. The primary goal of the study was to understand the influence of frequency, sliding distance and load variations on the formation of ripple patterns on the wear scars surface. The morphological alteration from continuous to broken ripple shapes was observed. Our study suggests that the geometrical shape of ripples is affected by the formation of the periodic array of grooves.

Introduction

Diamond has high chemical inertness, low wear rate under high load, and low coefficient of friction (COF) which makes diamond films attractive for many tribological applications. This study focuses on the observation and description of ripple patterns on top of nanocrystalline diamond (NCD) films formed under reciprocating sliding test conditions against Si₃N₄ balls. We recently showed that characteristic ripple patterns can be observed during reciprocating sliding experiments on top of NCD and diamond-like-carbon (DLC) films for different counter body materials, namely Al₂O₃, ZrO₂ and Si₃N₄ [1]. The formation of such surface ripples has been reported for diverse materials using different surface processing methods such as ion beams [2] and scanning probes [3]. The present study aims to understand for diamond the mechanisms of the ripple patterns formation by means of the preparation of ripple patterns with different morphology and the quantitative evaluation of their geometrical parameters.

Experimental

The NCD films were grown on (100)-oriented Si wafers by hot-filament chemical vapor deposition (HFCVD) using an sp³ Diamond Technologies, Inc. 655 reactor with a gas flow of 65 sccm CH₄ and 3000 sccm H₂. The substrate temperature was about 850 °C and the chamber pressure was 6 Torr. The diamond was deposited on 100-mm diameter (100)-oriented Si wafers. The thickness of diamond layer was 0.8 μm. The reciprocating sliding tests were carried out by a CETR[®] tribometer at room humidity using 3-mm diameter Si₃N₄ balls at a normal force of 2 and 3 N and a frequency of 2, 5 and 10 Hz. Two tests at each frequency were carried out, i.e. tests with 14 400 and 21 600 cycles at 2 Hz, 36 000 and 54 000 cycles at 5 Hz and 72 000 and 108 000 cycles at 10 Hz were conducted.

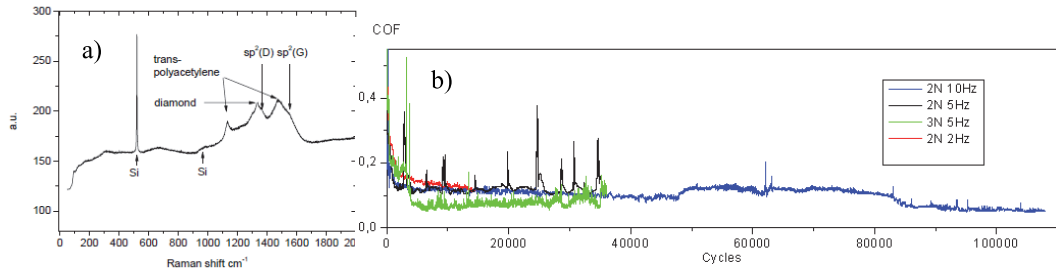


Fig. 1. (a) Raman spectrum of the pristine NCD film and (b) coefficient of friction versus cycles for tests at 2Hz, 5Hz and 10Hz for different sliding distances.

The chemical structure of the films was characterized by Raman measurements using a Horiba LabRam HR 800 high-resolution spectrometer equipped with a multichannel CCD detection system in the backscattering configuration. The laser light wavelength was 532 nm, and the spectral resolution of the spectrometer was 0.5 cm^{-1} . The surface morphology of the NCD pristine film surface and the ripple patterns geometrical parameters were evaluated by atomic force microscopy (AFM) using an NT-MDT Solver P47H system at scan sizes of 20×20 and $5 \times 5 \text{ }\mu\text{m}^2$.

Results and discussion

Fig. 1a shows the Raman spectrum of the pristine NCD film. Peaks at 522 and 976 cm^{-1} correspond to Si, the peak at 1332 cm^{-1} is related to diamond and the peak at 1134 cm^{-1} is ascribed to the amorphous network. Peaks at 1355 and 1478 cm^{-1} correspond to sp^2 bonds (D and G peaks) and at 1540 cm^{-1} to sp^2 bonds in hydrogenated amorphous carbon or graphitic clusters.

Fig. 1b shows typical COF versus number of cycles curves recorded during the sliding tests on the NCD films against Si_3N_4 . Note that for the region with the same applied sliding distances, all tests done at 2 N show a similar trend, i.e. all three curves merge together after about 14 000 cycles at a COF value of about 0.12 followed by a further decrease to 0.06 for the test done at 10 Hz and 108 000 cycles of sliding distance. The experiment carried out at 3 N shows a rapid decrease in the COF during the running-in period due to surface smoothening followed by a stabilization of the COF value at about 0.08.

Figs. 2 and 3 show AFM images recorded on the wear scars surface formed after the sliding tests. Line scans of approximately $5 \text{ }\mu\text{m}$ in length were taken from Figs. 2c and 3a-c at the locations indicated by straight white lines and the surface geometrical parameters R_a (arithmetic average roughness), R_q (root-mean-square roughness), R_z (ten point height of irregularities) and D (profile peak density, i.e. number of peaks along the scan line) were obtained from it and are reported in Table 1. A periodic array of longitudinal grooves can be observed in Fig. 2a and 2b. A number of grooves on the NCD surface decreases from Fig. 2a to Fig. 2c and only two grooves can be found in Fig. 2c. Ultimately the grooves disappear in Fig. 2d. Therefore, the number of grooves decreases with increasing frequency (from 2 Hz to 10 Hz) and sliding distance (from 14 400 to 108 000 cycles).

The ripple patterns morphology depends on the sliding test conditions as well. Fig. 3a is a part of Fig. 2b confined within the white square; the same applies for Figs. 3c and 2d. It is worth noting the similarity between the experiments done at 2 and 3 N, see Fig. 3. The transversal ripples appear as continuous surface corrugations in both tests at 5 Hz and 36 000 cycles, see Fig. 3a and 3b. Interestingly, the difference between R_a , R_q and R_z is about 20-25 %, however the peak density obtained from Fig. 3a nearly doubles compared to Fig. 3b; see Table 1 (line scans No. 3 and 4). Variations in roughness parameters for different line scans taken on the NCD film surface shown in

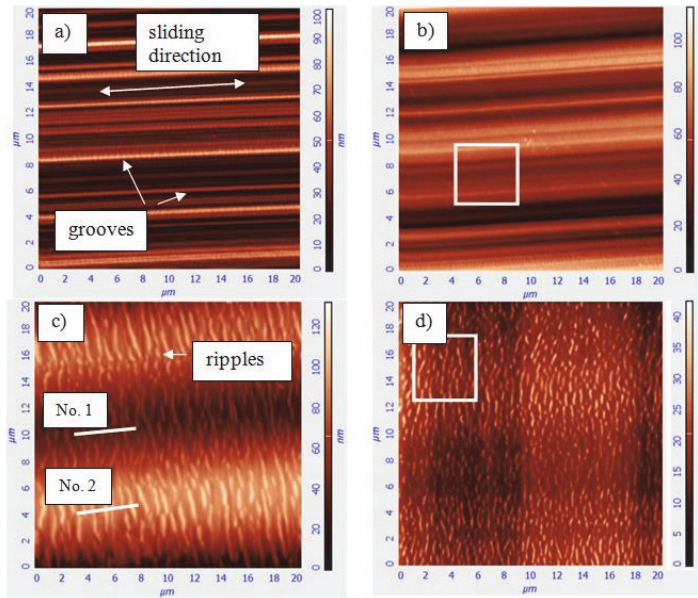


Fig. 2. AFM images ($20 \times 20 \mu\text{m}^2$) taken after (a) 2 N, 2 Hz (14 400 cycles), (b) 2 N, 5 Hz (36 000 cycles), (c) 2 N, 10 Hz (72 000 cycles) and (d) 2 N, 10 Hz (108 000 cycles) tests. The white squares in Fig. 2b and 2d are about $5 \times 5 \mu\text{m}^2$ in size and indicate locations at which images shown in Fig. 3a and 3c were taken.

Fig. 3a were about $\pm 10\%$, however the variations were about 23-30 % for several line scans, see line scan No. 3* in Table 1 and two white arrows in Fig. 3a indicating the position of this line scan.

Although continuous ripples are observed in Fig. 3a and 3b, the ripples become broken in Figs. 2c, 2d and 3c. The line scans shown in Fig. 2c were taken on bottom (No. 1) and top (No. 2) of the groove observed after the experiment at 2 N (10 Hz, 72 000 cycles). The values obtained for the R_a , R_q and R_z parameters on top of groove are about 21-26 % higher than the ones on the bottom, however, the peak density shows an opposite trend, see Table 1. This behavior is typical for the whole area along the groove, i.e. not only for the line scans shown in Fig. 2c, i.e. the ripple pattern formed on the bottom of the groove differs from that on the top. Taking this into account, we conclude that the changes in the array of grooves probably induce the shape alteration of the ripples. The decrease in peak density for the line scan No. 3* can be explained by a fragmentation of ripples due to wear, which starts on top of the ripples and results in a decrease of their apparent height and possible final elimination. It is indicated by a decrease in the roughness parameter value for the line scan No. 3*, as opposed to No. 3. A difference in wear regime for certain ripples may explain the formation of the complex ripple patterns shown in Fig. 2c and 2d. The geometrical parameters for the line scan between the black arrows (see Fig. 3a) was similar to those for the line scan No. 3. In addition, the shape of the broken ripples is sensitive to the test conditions. For instance, the parameter values R_a , R_q and R_z of the broken ripples shown in Fig. 2c (see line scan No. 2) are almost twice as high compared to the ones obtained from Fig. 3c (see line scan No. 5), however parameter D remains nearly the same.

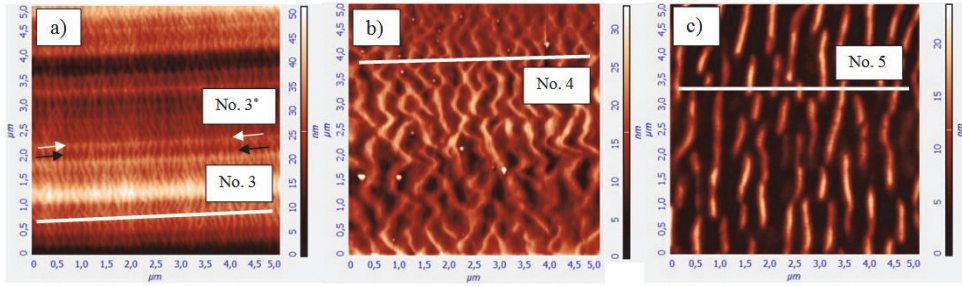


Fig. 3. AFM images ($5 \times 5 \mu\text{m}^2$) taken after (a) 2 N, 5 Hz (36 000 cycles), (b) 3 N, 5 Hz (36 000 cycles) and (c) 2 N, 10 Hz (108 000 cycles) tests. The image a) was taken on the place marked by white square in Fig. 2b and the image c) in Fig. 2d, respectively.

Table 1. Parameters R_a (arithmetical average roughness), R_q (root-mean-square), R_z (ten point height of irregularities) and D (profile peak density) derived from line scans No. 1 - No. 5.

Line scan number (AFM scan area)	R_a (nm)	R_q (nm)	R_z (nm)	D
No. 1 ($20 \times 20 \mu\text{m}^2$)	4.6	5.8	19.6	9.4
No. 2 ($20 \times 20 \mu\text{m}^2$)	6.2	7.9	24.8	7.5
No. 3 ($5 \times 5 \mu\text{m}^2$)	1.7	2.0	8.4	38.0
No. 3* ($5 \times 5 \mu\text{m}^2$)	1.2	1.5	6.4	29.0
No. 4 ($5 \times 5 \mu\text{m}^2$)	2.3	2.7	10.4	17.8
No. 5 ($5 \times 5 \mu\text{m}^2$)	3.3	3.9	12.5	7.8

Conclusions

The morphology of the NCD film surface obtained under reciprocating sliding test conditions against Si_3N_4 balls undergoes morphological changes, which depend on frequency, load and sliding distance of the test. Longitudinal grooves and transversal ripples are formed on the wear scars surface. Continuous and broken types of ripples are observed. The influence of the morphology of the array of grooves on the ripple patterns formation is suggested.

References

- [1] V. Podgursky, T. Hantschel, A. Bogatov, E. Kimmari, M. Antonov, M. Viljus, V. Mikli, M. Tsigkourakos, W. Vandervorst, J.G. Buijnsters, A.T. Raadik, P. Kulu, Tribological Properties of Conductive Boron Doped Nanocrystalline Diamond Films, International Conference on Diamond and Carbon Materials 2012, Granada, Spain.
- [2] R. Cuerno, M. Castro, J. Muñoz-García, R. Gago, and L. Vázquez, Nanoscale pattern formation at surfaces under ion-beam sputtering: A perspective from continuum models Nucl. Instr. Meth. in Phys. Res. B 269 (2011) 894–900.
- [3] B. Such, F. Krok, and M. Szymonski, AFM tip-induced ripple pattern on AlIII-BV semiconductor surfaces, Appl. Surf. Sci. 254 (2008) 5431-5434.

Acknowledgment

The work was supported by the Estonian Science Foundation grant Nr. 8696.

Publication III. Bogatov, A., Viljus, M., Raadik, T., Hantschel, T., Podgursky, V. Nanocrystalline diamond films deformation observed during sliding tests against Si₃N₄ balls. *Accepted for publication in Materials Science (Medžiagotyra)*

Nanocrystalline Diamond Films Deformation Observed During Sliding Tests Against Si₃N₄ Balls

Andrei BOGATOV^{1*}, Mart VILJUS², Taavi RAADIK³, Thomas HANTSCHEL⁴, Vitali PODGURSKY¹

¹ Tallinn University of Technology, Department of Materials Engineering, Ehitajate tee 5, 19086 Tallinn, Estonia

² Tallinn University of Technology, Center of Materials Research, Ehitajate tee 5, 19086 Tallinn, Estonia

³ Tallinn University of Technology, Department of Materials Science, Ehitajate tee 5, 19086 Tallinn, Estonia

⁴ Imec, Kapeldreef 75, B-3001 Leuven, Belgium

crossref <http://dx.doi.org/10.XXXX/j01.xxxxxx>

Received XX June 201X; accepted XX December 201X

The study investigates wear performance of nanocrystalline diamond (NCD) films under reciprocating sliding conditions. The NCD films were grown by hot-filament chemical vapor deposition (HFCVD) method on (100) oriented Si wafers. The surface morphology was characterized by atomic force microscopy (AFM), scanning electron microscopy (SEM) and mechanical profilometry. The study focuses on the understanding of mechanisms resulting in NCD films deformation and formation of ripple patterns on the wear scars surface observed during reciprocal sliding tests. Plastic deformation of the Si wafer due to NCD film deposition and high local contact pressure and temperature during sliding lead to structural changes on the Si(100)/NCD film interface, thus causing the NCD film to deform and the characteristic ripple patterns to develop on the wear scars surface.

Keywords: diamond films deformation, tribology, wear mechanisms, ripples

1. INTRODUCTION

Diamond and diamond films have attracted considerable interest in tribological applications due to unique properties of diamond including high hardness and Young's modulus, low coefficient of friction (COF) and high chemical inertness. In the past different wear mechanisms of the diamond films were investigated. Wear on diamond is a load- and velocity-dependent process [1]. Surface morphology [2], diamond grain orientation [3], formation of an amorphous carbonaceous lubricating layer [1] and passivation of dangling carbon bonds by species from ambient environment [4] play a significant role in understanding of the frictional behavior of diamond films.

The formation of transversal ripples and longitudinal grooves on the wear scars surface on NCD films were reported in our previous studies [5,6]. It is a complex phenomenon and can therefore not be explained by a single mechanism [6]. For instance, it was found that the morphological changes in ripple patterns depend on the ball material [6] and test duration [5].

The present study aims to investigate the underlying mechanisms of NCD film deflection and ripples formation during sliding against Si₃N₄ balls.

2. EXPERIMENTAL DETAILS

A 0.8 μm thick NCD film was grown on a 100-mm diameter (100)-oriented 500 μm thick Si wafer by hot-filament chemical vapour deposition (HFCVD) using an

sp3 Diamond Technologies, Inc. 655 reactor in a 2.4% CH₄/H₂ gas mixture. The substrate temperature was about 850 °C and the chamber pressure was maintained at 6 Torr. After the NCD film deposition, the Si wafer was cut into bars of about 10 mm² in size along cleavage directions.

Room temperature Raman spectra were recorded by using a Horiba LabRam HR 800 high-resolution spectrometer equipped with a multichannel CCD detection system in the backscattering configuration. The laser light wavelength was 532 nm, and the spectral resolution of the spectrometer was 0.5 cm⁻¹.

Reciprocating sliding tests (normal load 2 N, displacement amplitude 1 mm, frequency 2, 5 and 8Hz, relative humidity about 35 %, ball diameter Ø 3 mm) were carried out by means of a CETR[®] UMT-2 tribometer. Si₃N₄ balls (surface roughness R_a = 0.012 μm) (REDHILL, Czech Republic) were used as a counter body. The duration of the tests was 1800, 3000 and 6000 cycles.

According to producer provided data, the hardness, Young's modulus and Poisson ratio of the Si₃N₄ balls were 1400-1700 HV, 310 GPa and 0.27, respectively. Monocrystalline Si (100) possesses a hardness of about 12 GPa [7]; due to crystal anisotropy its Young's modulus varies along the (100) plane from about 130 [8] to 170-180 GPa [7,8], the Poisson ratio is 0.278 [9], the fracture strength measured on Si (100) wafers is about 6.1 GPa [10]. In the context of the present study, a dependence of mechanical properties of the Si single crystal on the temperature should be considered. The brittle-to-ductile transition (BDT) occurs in Si at about 530 °C [11-13]. Brittle rupture (brittle plasticity) of monocrystalline Si takes place at a temperature of <530 °C and at higher

* Corresponding author. Tel.: +372-56506423.
E-mail address: andrei.bogatov@ttu.ee

temperature the formation and movement of dislocations results in ductile plasticity.

AFM measurements (NT-MDT Solver P47H) were performed in contact mode using Si cantilevers and tips. Profilometric scans were done with a Mahr Perthometer® (Göttingen, Germany).

3. RESULTS AND DISCUSSION

Fig. 1 shows an AFM image taken on the as-deposited NCD film surface. The diamond grains with sharp edges cover the entire Si wafer surface. The maximum grain size is about 0.5 μm .

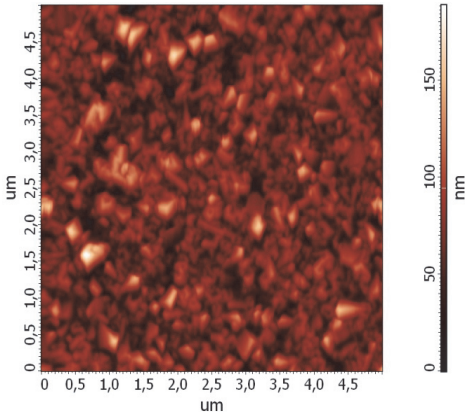


Fig. 1. AFM image of the pristine NCD film surface.

Fig. 2 shows the typical Raman spectrum of the NCD film. The peaks at 522 and 976 cm^{-1} correspond to the Si substrate, the peak at 1332 cm^{-1} relates to diamond and the peaks at 1134 and 1478 cm^{-1} are ascribed to the presence of trans-polyacetylene (t-PA) at the grain boundaries [14]. The peaks at 1355 and 1540 cm^{-1} correspond to the D and G bands [15].

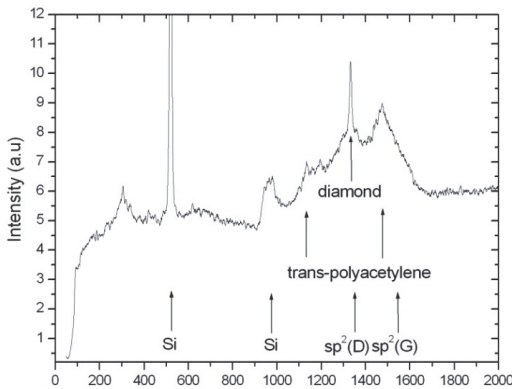


Fig. 2. Raman spectrum of the pristine NCD film.

Fig. 3 shows the coefficient of friction (COF) versus number of cycles curves for 6000 cycles of sliding for the used test frequency of 2, 5 and 8 Hz respectively. The

highest COF value is observed at the beginning of the tests and is related to the high NCD film surface roughness. Because of the progressing NCD film surface abrasion, the COF value decreases gradually and, finally, stabilizes at about 0.1. In the case of the test done at 8 Hz, the run-in period is shorter than for tests carried out at 2 and 5 Hz, i.e. the surface smoothing proceeds faster with the higher ball velocity.

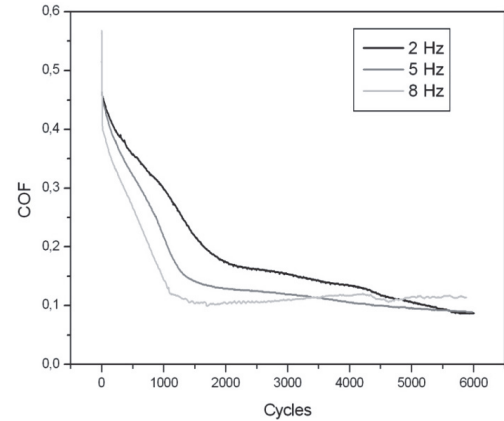


Fig. 3. COF versus cycle curves after 6000 cycles of sliding at 2, 5 and 8 Hz.

Fig. 4 shows an AFM image taken on the central region of the wear scar after 1800 cycles sliding at 8 Hz.

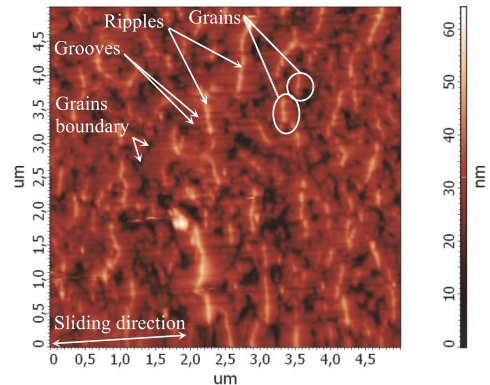


Fig. 4. AFM image of the worn NCD film surface after 1800 cycles of sliding at 8 Hz.

A polished surface on top of diamond grains can be observed and clear ripple patterns are formed approximately at the middle of diamond grains (visible as white lines in the AFM image). Line scans taken on the wear scars by means of mechanical profilometry are shown in Fig. 5. The roughness of the NCD film as measured by AFM decreases from the average roughness value $R_a=0.019 \mu\text{m}$ (ten point height of irregularities value $R_z=0.105 \mu\text{m}$) for the as-deposited NCD film surface to $R_a=0.005 \mu\text{m}$ ($R_z=0.032 \mu\text{m}$) for the wear scar surface

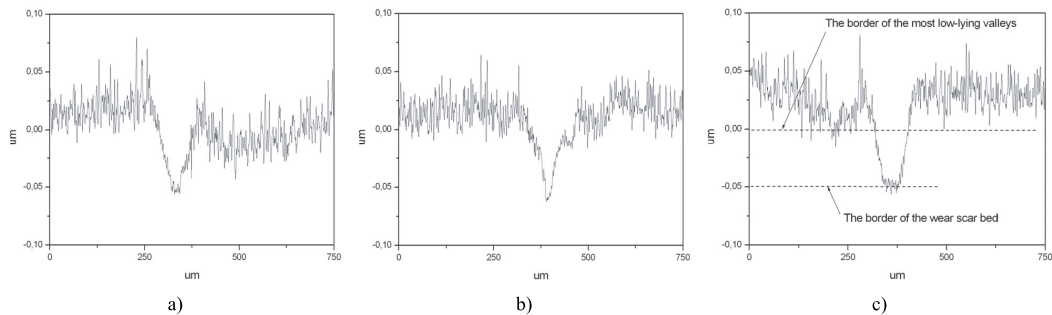


Fig. 5. Line scans taken on the wear scars after 1800 cycles of sliding at 2 Hz (a), 5 Hz (b) and 8 Hz (c).

after 1800 cycles of sliding at 8 Hz, see Fig. 6(a). In other words, the parameter R_z is an average distance between the highest peaks and deepest valleys. A level of the border of the most low-lying valleys is schematically indicated by the dashed line in Figs. 5(c) and 6. At the beginning of the sliding, wear takes place on the NCD film surface corrugations. After 1800 cycles of sliding at 8 Hz, grain boundaries can clearly be observed in Fig. 4. Therefore, it can be expected that the level of the border of the wear scar bed should lie above the level of the border of the most low-lying valleys of unaffected as-deposited NCD film surface. However, the level of the border of the wear scar bed lies well below the level of the border of the most low-lying valleys of the pristine NCD film surface, see Fig. 5(c). Schematically, these results are represented in Fig. 6(a). The results of profilometric measurements shown in Fig. 5(c) are more adequately described by the scheme shown in Fig. 6(a) than in Fig. 6(b) by recognizing that the grain boundaries can be seen in Fig. 4. Indeed, it is assumed that the NCD film is not deflected at the scheme

shown in Fig. 6(b), however the analysis of wear scars profile suggests that the NCD film can be plastically deformed during the sliding tests. This vertical deformation (further called 'deflection') is about $0.05 \mu\text{m}$ after 1800 cycles sliding at 8 Hz, wherein, no visible cracks were observed on the wear scars surface. Note that a similar NCD film deflection was observed after 3000 and 6000 cycles of tribotests (not shown) as well.

The contact pressure of the Si (100) clean surface in contact with a Si_3N_4 ball can be estimated based on Hertzian contact mechanics. It is about 0.8 - 0.9 GPa under a load of 2 N. Due to the high hardness and fracture strength of silicon, it is unlikely that under such a contact pressure Si (100) undergoes a brittle fracture at room temperature.

In this case of a hard coating on a soft substrate the coating thickness and hardness and the Young's modulus of both coating and substrate are the principal parameters affecting the tribological behavior of the coating/substrate system [16]. Thin layers subjected to contact with the

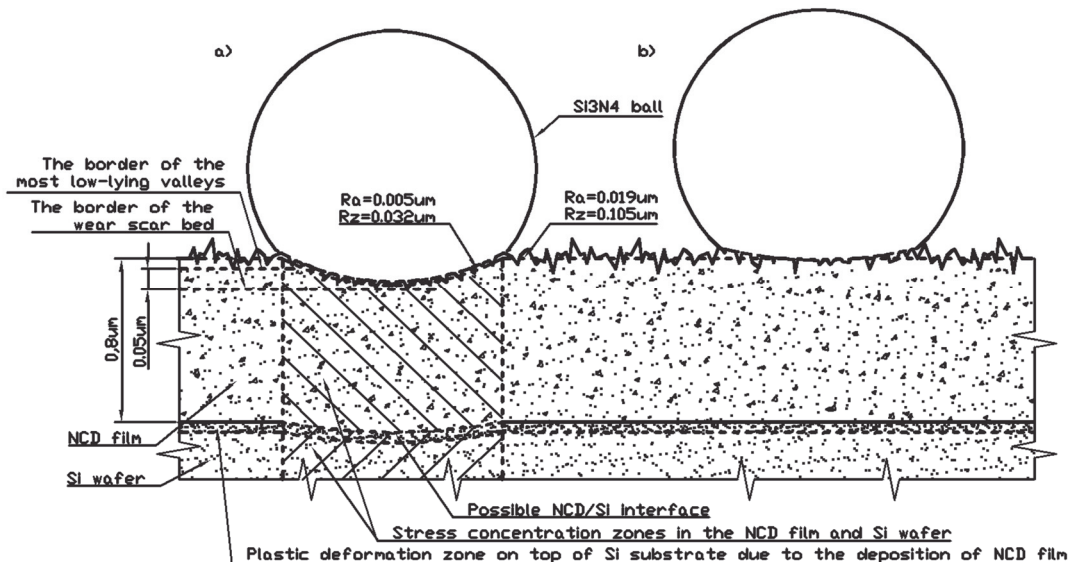


Fig. 6. Schematic representation of the results shown in Fig. 5(c) : wear scar profile according to profilometric measurements after 1800 cycles sliding at 8 Hz (a) and expected wear scar profile in assumption that no NCD film deflection occurs (b).

counterpart only partially carry the stress distribution, the rest of the stress is carried by the substrate, see Fig. 6 (a). In the case of the NCD film on top of Si (100) wafer, the calculation of contact pressure becomes more complicated due to the roughness of the diamond film (see Fig. 1).

Based on our experimental observations, we believe that the NCD film deformation can be explained by the plastic deformation of the Si (100) substrate. *Firstly*, the formation of a dislocation network on the Si (100)/diamond film interface was found after the deposition of diamond film at 690 °C [17]. Note that the NCD film deposition temperature was 850 °C in the present study, i.e. well above the BDT temperature in Si (> 530 °C). Therefore, an induced plastic deformation of the Si wafer can already be expected after the NCD film deposition. *Secondly*, the actual value of the contact pressure on the Si wafer can be remarkably higher than the calculated value mentioned above. Indeed, at the beginning of the test the Si₃N₄ ball is placed in contact with the apex of sharp diamond grains. Therefore, the local contact pressure between a particular grain and the Si₃N₄ ball surface can be greatly underestimated from the aforementioned calculation for the ball on the plain surface. This high local contact pressure could induce the deformation of the Si wafer surface. *Thirdly*, a high local temperature at the so-called frictional hot-spots [18, 19], i.e. at points of contact between surface asperities of the counterbodies, can account for the Si wafer mechanical properties variation. In conclusion, the BDT effect in Si at high NCD film deposition temperature and high local contact pressure and temperature during sliding can lead to the plastic deformation of Si surface on the Si(100)/NCD interface. Thus, the NCD film deformation could occur as a consequence of the Si substrate plastic deformation. However, likely due to the high Young's modulus and fracture strength of the NCD film no cracks on the NCD film surface were found. It is worth noting that the aforementioned high local contact pressure and temperature during sliding are considered in conjunction with the graphitization of diamond and diamond films [1,6,18,19 and references therein], without the possible influence on the global deformation of diamond films.

The high Young's modulus and a relatively small thickness of the NCD film provide flexibility to the NCD film [16] and hence the NCD film surface can follow the surface deformation during sliding without cracks and surface failure. A bent torus on the NCD film surface is likely formed in front of the ball as shown in [16] during sliding. In addition, the torus size can be affected due to the plastic deformation on the Si(100)/NCD film interface. Periodic bending of the NCD film during reciprocating sliding could contribute to the formation of transversal protrusions on top of NCD film, i.e. surface ripples.

4. CONCLUSIONS

We observed the deformation of NCD films after sliding tests. The BDT effect in Si, high local contact pressure and temperature during sliding induce a plastic deformation on the Si single crystal surface, which leads to the deflection of the NCD film during reciprocal sliding.

On the other hand the periodic bending of the NCD film during sliding can be considered as an extra factor affecting the formation of ripple patterns on the wear scars surface.

Acknowledgment

This work was supported by institutional research funding IUT-19-29 of the Estonian Ministry of Education and Research.

REFERENCES

1. **Pastewka, L., Moser, S., Gumbsch, P., Moseler, M.** Anisotropic mechanical amorphization drives wear in diamond. *Nature Materials* 10 2011: pp. 34-38
2. **Bhushan, B., Subramaniam, V.V., Malshe, A., Gupta, B. K., Ruan, J.** Tribological properties of polished diamond films *Journal of Applied Physics* 74 (6) 1993: pp. 4174-4180
3. **El-Dasher, B.S., Gray, J. J., Tringe, J. W., Biener, J., Hamza, A. V.** Crystallographic anisotropy of wear on a polycrystalline diamond surface. *Applied Physics Letters* 88 2006: pp. 241915-1 - 241915-3
4. **Konicek, A. R., Grierson, D. S., Sumant, A. V., Friedmann, T. A., Sullivan, J. P., Gilbert, P. U. P. A., Sawyer, W. G., Carpick, R. W.** Influence of surface passivation on the friction and wear behavior of ultrananocrystalline diamond and tetrahedral amorphous carbon thin films. *Physical Review B* 85 2012: pp. 155448-1 - 155448-13
5. **Bogatov, A., Podgursky, V., Raadik, T., Kamjula, A. R., Hantschel, T., Tsigkourakos, M., Kulu, P.** Investigation of morphology changes on nanocrystalline diamond film surfaces during reciprocating sliding against Si₃N₄ balls, *Key Engineering Materials* 604 2014: pp. 126-129
6. **Podgursky, V., Hantschel, T., Bogatov, A., Kimmari, E., Antonov, M., Viljus, M., Mikli, V., Tsigkourakos, M., Vandervorst, W., Buijnsters, J.G., Raadik, A.T., Kulu, P.** Rippling on wear scar surfaces of nanocrystalline diamond films after reciprocating sliding against ceramic balls, To be published.
7. **Bhushan, B., Li, X.** Micromechanical and tribological characterization of doped single-crystal silicon and polysilicon films for microelectromechanical systems devices *Journal of Materials Research* 12 (01) 1997: pp. 54 – 63
8. **Boyd, E. J., Uttamchandani, D.** Measurement of the Anisotropy of Young's Modulus in Single-Crystal Silicon, *Journal of Microelectromechanical Systems* 21 (1) 2012: pp. 243-249
9. **Gan, L., Ben-Nissan, B., Ben-David, A.** Modelling and finite element analysis of ultra-microhardness indentation of thin films *Thin Solid Films* 290–291 1996: pp. 362–366

10. **Ericson, F., Schweitz, J.-A.** Micromechanical fracture strength of silicon, *Journal of Applied Physics* 68 1990: pp. 5840-5844
11. **John C. S.** The Brittle-to-ductile transition in Pre-cleaved Silicon Single Crystals *Philosophical Magazine* 32 1975: pp. 1193-1212
12. **Sen, D., Thaulow, C., Schieffer, S. V., Cohen, A., Buehler M. J.** Atomistic Study of Crack-Tip Cleavage to Dislocation Emission Transition in Silicon Single Crystals, *Physical Review Letters* 104 2010: pp. 235502-1 - 235502-4
13. **Sen, D. Cohen, A., Thompson, A. P., Duin, A. V., Goddard III, W. A., Buehler, M. J.** Direct atomistic simulation of brittle-to-ductile transition in silicon single crystals. *Materials Research Society Proceedings* 1272 2010: pp. 1272-04 – 1272-13
14. **Ferrari, A.C., Robertson, J.** Raman spectroscopy of amorphous, nanostructured, diamond-like carbon, and nanodiamond *Philosophical Transactions of the Royal Society A* 362 2004: pp. 2477-2512
15. **Ferrari, A.C., Robertson, J.** Resonant Raman spectroscopy of disordered, amorphous, and diamondlike carbon *Physical Review B* 64 2001: pp. 075414-1 - 075414-13
16. **Holmberg, K., Laukkanen, A., Ronkainen, H., Wallin, K., Varjus, S., Koskinen, J.** Tribological contact analysis of a rigid ball sliding on a hard coated surface Part II: Material deformations, influence of coating thickness and Young's modulus. *Surf. Coat. Technol.* 200 2006: pp. 3810-3823
17. **Michler, J., Mermoux, M., von Kaenel, Y., Haoui, A., Lucazeau, G., Blank, E.** Residual stress in diamond films: origins and modelling *Thin Solid Films* 357 (2) 1999: pp. 189-201
18. **Bowden, F. P., Freitag, E. H.** The friction of solids at very high speeds *Proceedings of the Royal Society A* 248 1958: pp. 350–367
19. **Erdemir, A., Halter, M., Fenske, G.R., Zuiker, C., Csencsits, R., Krauss, A.R., Gruen, D.M.** Friction and Wear Mechanisms of Smooth Diamond Films During Sliding in Air and Dry Nitrogen *Tribology Transactions* 40 1997: pp. 667-675

Publication IV. Podgursky, V., Bogatov, A., Freund, M., Kulu, P. Influence of surface morphology on the tribological behavior of diamond-like carbon coating. *Key Engineering Materials* 2013, Vol. 527, 83-91

Influence of surface morphology on the tribological behavior of diamond-like carbon coating

V. Podgursky^a, A. Bogatov, M. Freund, P. Kulu

Tallinn University of Technology, Department of Materials Engineering, Ehitajate tee 5, 19086 Tallinn, Estonia

^aCorresponding author: vitali.podgurski@ttu.ee

Keywords: diamond-like carbon, surface morphology, friction

Abstract

Diamond-like carbon (DLC) films were prepared on top of hard coatings, namely, prior to the DLC deposition, CrN, TiCN and nanocomposite nACo (nc-AlTiN/(a-Si₃N₄)) layers were deposited on WC-Co substrates. The R_a roughness of WC-Co substrates was 0.05 and 0.2 μm . Surface morphology of DLC coatings was investigated by means of profilometry and geometrical parameters R_a (average roughness), R_{sk} (skewness), R_{ku} (kurtosis) and R_z (mean peak to valley height) were evaluated. Fretting tests were conducted with 3 mm in diameter alumina balls under 1 and 2 N load, at slip distance of 2 mm and frequency of 2 Hz. Statistical analysis shows significant correlation between R_a and R_z parameters corresponding to initial DLC surface and wear scar surfaces produced by fretting tests after 2400 and 4800 cycles, respectively. This finding indicates a relationship between friction (wear) and R_a and R_z parameters. Positive correlation between the coefficient of friction (COF) and kurtosis R_{ku} indicates that surface flatness is an important factor for optimal friction of an alumina ball against DLC coating.

Introduction

There has been an increasing interest in diamond-like carbon (DLC) coatings. Low coefficient of friction (COF), high hardness, as well as chemical inertness of DLC are an ideal combination of properties for a variety of tribological applications [1]. High wear resistance and low COF are a consequence of the solid lubrication effect of DLC, high hardness gives a good resistance to abrasive wear and, finally, high chemical stability results in a high resistance to solution wear. Tribological properties of DLC depend on the intrinsic factors (the ratio of sp^3/sp^2 hybridization of carbon bonds, hydrogen and impurities concentration, surface roughness, etc) and extrinsic factors (test conditions) [1-3]. Finally, it can be stated that the COF and wear correlate positively with the roughness of a DLC surface [1, 4-6].

It is widely accepted that initial surface morphology plays an important role during the running-in period of the tribological test [7-13]. In practice, many surfaces possess non-Gaussian height distribution function (HDF) that was taken into account by C. A. Kotwal and B. Bhushan [9]. The theory is based on the model that friction is proportional to the real area of contact, and the key geometrical parameters of the surface are skewness and kurtosis. The theory predicts that the COF decreases with increasing kurtosis, assuming positive skewness. Good agreement with the mentioned conclusion was found in previous works [10-12].

Asperities on the coating surface are considered as centers where coating failure or excessive wear can occur. It is worth noting that different post-treatment techniques are used to reduce the number of defects on the coating surface. In other words, due to post-treatment a lifetime of the coating can be significantly extended, i.e. properties at the later stages of coating development can strongly depend on the properties of a freshly deposited coating.

By the qualitative description, coating surface becomes smoother after initial transient and adhesive/abrasive wear increase during the steady state of the tribological test [2,13]. In addition to the influence of surface morphology, the investigation of the DLC coating is complicated by the lubrication effect, which is explained in terms of transfer layer formation between the counterbodies in the tribological test. The approach based on the correlation analysis of the results was used in the present study. Focus was on the evaluation of geometrical parameters corresponding to the surface of tribological contact, which undergoes permanent modification during the test. Subsequently, a correlation between the COF and geometrical parameters of initial and wear scar surfaces of the DLC coating were under investigation.

Experimental method

Diamond-like carbon (Me-C:H, metal doped DLC) samples with different surface morphology were prepared by means of the Plasma Enhance Chemical Vapor Deposition (PECVD) method. Prior to the deposition of the DLC, hard coatings (nanocomposite nACo (nc-AlTiN/(a-Si₃N₄)) and single layers of CrN and TiCN) were deposited on top of WC-Co substrates with different roughness R_a , namely 0.05 and 0.2 μm . In total, six DLC samples were under investigation. The abbreviation for the DLC coatings investigated is as follows: FiVic²[®] (nACo+DLC), CROMVic²[®] (CrN+DLC) and CVic²[®] (TiCN+DLC). The thickness of the DLC layer was 1-1.5 μm .

The hard coatings and DLC were deposited in Physical Vapor Deposition- Plasma Enhance Chemical Vapor Deposition (PVD-PECVD) unit PLATIT[®] π 80. Hard coatings (nACo, CrN, TiCN) were prepared by the arc ion plating process on AlSi, Cr and Ti cathodes, in nitrogen or nitrogen/acetylene (for TiCN) atmosphere. The deposition temperature was 450 °C. DLC film were grown by dissociation of acetylene. Due to plasma etching on cathodes, traces of cathode materials in DLC are expected.

The flat WC-Co specimens (3.0 x 15.0 x 25.0 mm) were cleaned in an ultrasonic bath with alcohol. Immediately after the cleaning procedure, samples were placed into the vacuum chamber and mounted on the sample holder. Finally, samples were sputter-cleaned in argon plasma and a thin metallic Ti layer was deposited on the substrates prior to the hard coating deposition.

The room temperature Raman spectra were recorded by using a Horiba's LabRam HR 800 high resolution spectrometer equipped with a multichannel CCD detection system in the backscattering configuration. The spectral resolution of the spectrometer was 0.5 cm^{-1} .

The fretting tests (1 and 2 N, 2 mm, 2 Hz, room humidity, \varnothing 3 mm Al₂O₃) were conducted by means of a CETR[®] tribometer. Alumina balls were used to diminish the tribochemical wear. The samples were tested for 2400 and 4800 cycles.

Profilometric scans were done with a Mahr Perthometer[®] (Göttingen, Germany). Scan length was 1.25 mm and sample size was 12, i.e. 12 scans were carried out on each initial DLC sample surface and along the wear scar surfaces. Height distribution function (HDF) parameters, including average roughness (R_a), kurtosis (R_{ku}), skewness (R_{sk}) and mean peak to valley height (R_z), were computed automatically.

Results and discussion

Characteristic Raman spectrum of a DLC coating is shown in Fig. 1. The laser wavelength of 514.5 nm was used. The broad peak is composed of two bands centered at approximately 1550 cm^{-1}

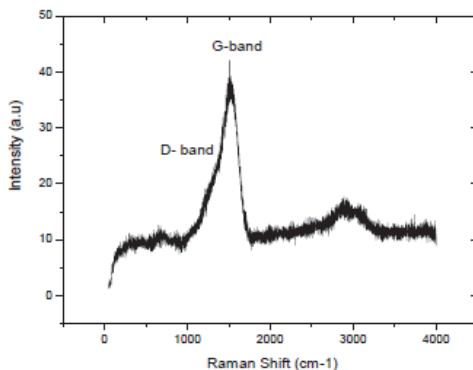


Fig. 1. Raman spectrum of the DLC coating.

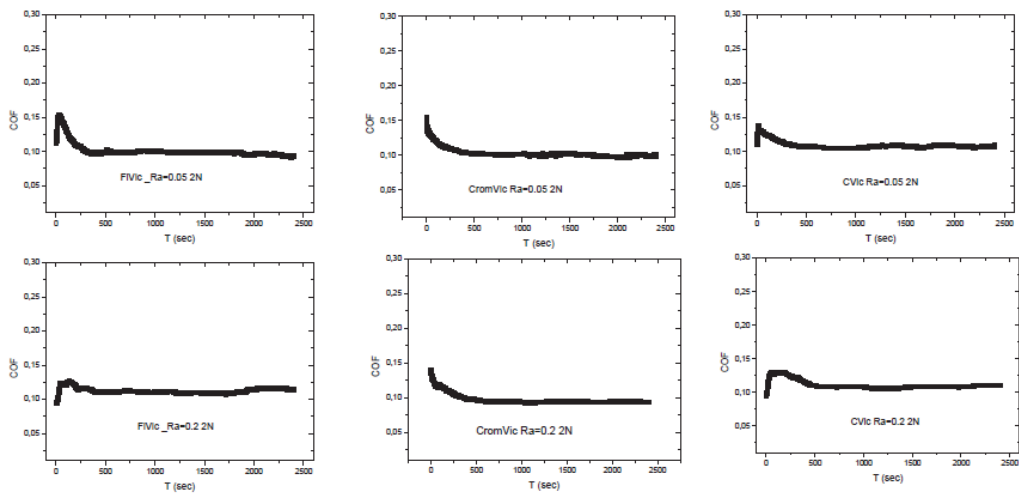


Fig. 2. The COF value versus the number of cycle curves recorded on FiVic^{2®}, CROMVic^{2®} and CVic^{2®} samples after 2400 cycles.

Table 1. Geometrical parameters R_a , R_z , R_{sk} and R_{ku} of clean DLC surface and wear scar surfaces after 2400 and 4800 cycles, respectively. The roughness of WC-Co substrates were 0.05 and 0.2 μm , and the load during the fretting test was 1 and 2 N.

	R_a [μm] clean DLC	R_z [μm] clean DLC	R_{sk} clean DLC	R_{ku} clean DLC	R_a [μm] 2400 cycles	R_z [μm] 2400 cycles	R_{sk} 2400 cycles	R_{ku} 2400 cycles	R_a [μm] 4800 cycles	R_z [μm] 4800 cycles	R_{sk} 4800 cycles	R_{ku} 4800 cycles
FiVic ^{2®} (0.05 μm) Load 1 N	0.13	1.89	2.34	21.39	0.01	0.09	-1.62	6.84	0.01	0.07	-1.08	9.28
FiVic ^{2®} (0.05 μm) Load 2 N	0.13	1.89	2.34	21.39	0.01	0.06	-2.03	11.22	0.01	0.06	-0.68	4.00
FiVic ^{2®} (0.2 μm) Load 1 N	0.21	2.38	-0.04	10.56	0.03	0.25	-2.71	14.57	0.01	0.10	-4.67	39.64
FiVic ^{2®} (0.2 μm) Load 2 N	0.21	2.38	-0.04	10.56	0.03	0.24	-2.98	16.35	0.02	0.11	0.49	9.82
CROMVic ^{2®} (0.05 μm) Load 1 N	0.09	1.08	2.4	22.78	0.02	0.11	-1.18	5.46	0.02	0.13	-3.05	17.45
CROMVic ^{2®} (0.05 μm) Load 2 N	0.09	1.08	2.40	22.78	0.01	0.10	-1.95	11.12	0.02	0.14	-2.44	12.68
CROMVic ^{2®} (0.2 μm) Load 1 N	0.20	2.64	0.09	11.61	0.08	0.44	-1.37	5.37	0.08	0.49	-2.31	12.58
CROMVic ^{2®} (0.2 μm) Load 2 N	0.20	2.64	0.09	11.61	0.06	0.39	-2.29	11.62	0.07	0.39	-1.68	7.93
CVic ^{2®} (0.05 μm) Load 1 N	0.24	2.78	2.45	15.59	0.02	0.14	-3.79	29.42	0.02	0.18	-3.47	29.37
CVic ^{2®} (0.05 μm) Load 2 N	0.24	2.78	2.45	15.59	0.01	0.12	-4.64	40.44	0.01	0.12	-3.49	22.22
CVic ^{2®} (0.2 μm) Load 1 N	0.27	2.85	1.09	9.1	0.05	0.43	-3.67	22.30	0.03	0.17	-2.77	15.28
CVic ^{2®} (0.2 μm) Load 2 N	0.27	2.85	1.09	9.1	0.04	0.31	-2.46	12.04	0.02	0.19	-4.05	29.29

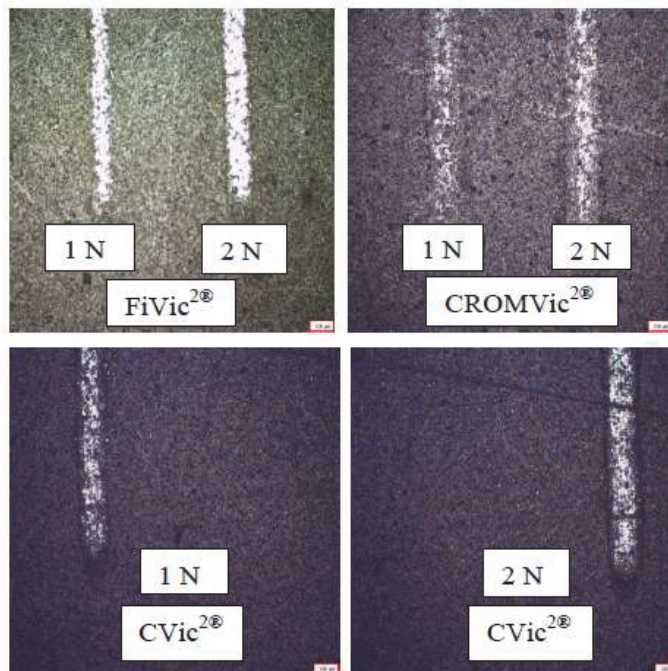


Fig. 3. Optical microscopy images of wear scar surfaces after 2400 cycles test under 1 and 2 N load, respectively. The distance bar is 100 μm .

(G band, corresponding to the well-ordered graphite) and 1360 cm^{-1} (D band, corresponding to disordered graphite) [3]. Peaks at about 3000 cm^{-1} are due to the C–H bands [14].

The typical COF value versus the number of cycle curves recorded on FiVic^{2®}, CROMVic^{2®} and CVic^{2®} samples after 2400 cycles are shown in Fig. 2. The running-in period (400-600 cycles) is followed by a steady stage. Surface geometrical parameters for an initial (clean) DLC surface and wear scar surfaces after 2400 and 4800 cycles of the tribological test are shown in Table 1. In contrast to the initial DLC surface, a decrease in R_a , R_z and R_{sk} corresponding to the wear scar surfaces was observed. Fig. 3 shows optical microscopy images of DLC coatings grown on the WC-Co substrates ($R_a = 0,02\ \mu\text{m}$) after 2400 cycles test under 1 and 2 N load, respectively. DLC roughness changes and the surface structure within wear tracks looks smoother than for a clean DLC surface. This observation is in a good agreement with the decrease in R_a and R_z parameters for the surface created after 2400 cycles (see Table 1). On the other hand, after testing with a 2 N load, the wear track looks more worn (smooth) than with 1 N load. The data in Table 1 support this observation as well, as R_a and R_z parameters are slightly higher for tests with 1 N than with 2 N, particularly for CROMVic^{2®} and CVic^{2®} samples. Finally, for the clean DLC surface, skewness is positive, however, skewness values for both wear scar surfaces are negative. It is well known that grinding and polishing (abrasion) produce surfaces with negative skewness [15]. Therefore, abrasive wear occurs during fretting on the DLC against alumina.

The correlation was estimated by means of the Spearman test, see e.g. T. Hill and P. Lewicki [16] and reference therein. The value of the correlation coefficient ranges between ± 1 . Low, moderate and high degree of correlation corresponds to the value of the correlation coefficient ranging between $0 - \pm 0,25$, $\pm 0,25 - \pm 0,75$ and $\pm 0,75 - \pm 1$, respectively. Statistical tests were performed using Statistica[®] package. The critical quantity $t(N-2)$ was calculated according to $R \times \sqrt{(N-2) / (1-R^2)}$, which corresponds to the value of quintile c_p of students' distribution with the $N-2$ degrees of

Table 2. Coefficient of correlation R between R_a and R_z parameters of the initial DLC surface and wear scar surfaces observed after 2400 and 4800 cycles. N - sample size. R - Spearman coefficient of correlation. Critical quantity $t(N-2)$ is explained in the text. The significant correlation is highlighted in bold.

<i>1. Correlation between geometrical parameters for particular surface (either clean DLC, or wear scar surfaces after 2400 and 4800 cycles)</i>	N	Spearman R	$t(N-2)$	p-value
R_a clean DLC & R_z clean DLC	6	0,98561	11,66190	0,000309
R_a 2400 & R_z 2400	12	0,964918	11,6219	0,000009
R_a 4800 & R_z 4800	12	0,920671	7,4587	0,000022
<i>2. Correlation between geometrical parameters for different surfaces</i>				
R_a clean DLC & R_a 2400	12	0,460539	1,6407	0,131894
R_z clean DLC & R_a 2400	12	0,510651	1,8782	0,089795
R_a 2400 & R_a 4800	12	0,838950	4,8750	0,000647
R_z 2400 & R_a 4800	12	0,814846	4,4452	0,001244
R_z clean DLC & R_z 2400	12	0,678483	2,9206	0,015284
R_z clean DLC & R_z 4800	12	0,522998	1,9404	0,081028
R_z 2400 & R_z 4800	12	0,741259	3,4923	0,005801

freedom. Sample size N is the number of observations included in a statistical sample. In practice, 90% is the minimum of confidence level for statistically significant results.

Table 2 shows significant correlation between R_a and R_z , corresponding to the three kinds investigated surfaces, namely, initial DLC surface and wear scar surfaces created after 2400 and 4800 cycles of the test. Among the geometrical parameters, the most sensitive ones were R_a and R_z , i.e. the highest correlation coefficient between these parameters for different surfaces were found. In the case of particular surface, i.e. either initial DLC or wear scar, there is a strong correlation between R_a and R_z . It must be expected, as higher roughness means higher difference between the highest peak and the lowest valley, therefore the correlation coefficient must be positive. The correlation between geometrical parameters corresponding to a different kind of a surface was observed as well. For instance, there is correlation between R_a and R_z measured on the wear scar and clean DLC surfaces, which is particularly remarkable between R_z parameters corresponding to the different surfaces. The existence of such correlation can indicate that, probably, wear correlates with the large asperities distribution and properties. The latter suggestion can be supported by the following reasons. First, this finding is in a good agreement with the statement in the Introduction that the roughness of the DLC surface is an important factor in the characterization of wear. Second, in the case of polytetrafluoroethylene (PTFE) composites, parameter R_{3z} is well correlated with the COF and linear wear, as mentioned by Wieleba [17]. Roughness parameter R_{3z} is similar to R_z except that less extreme peaks and valleys are included into the evaluation of the roughness parameter R_{3z} .

Table 3. Coefficient of correlation R between the COF (within the range of 5-200 cycles) and R_a and R_{ku} of the initial DLC surface. The significant correlation is highlighted in bold.

	N	Spearman R	t(N-2)	p-value
R_a clean DLC & COF ₅	24	-0,552611	-3,1100	0,005105
R_a clean DLC & COF ₁₀	24	-0,527803	-2,9147	0,008030
R_a clean DLC & COF ₂₀	24	-0,534065	-2,9629	0,007185
R_a clean DLC & COF ₃₀	24	-0,420362	-2,1730	0,040828
R_a clean DLC & COF ₅₀	24	-0,462398	-2,4460	0,022903
R_a clean DLC & COF ₆₀	24	-0,449975	-2,3633	0,027364
R_a clean DLC & COF ₈₀	24	-0,359544	-1,8073	0,084417
R_a clean DLC & COF ₁₀₀	24	-0,230008	-1,1086	0,279595
R_a clean DLC & COF ₁₅₀	24	-0,018786	-0,0881	0,930570
R_a clean DLC & COF ₂₀₀	24	0,044749	0,2101	0,835523
R_{ku} clean DLC & COF ₅	24	0,509406	2,7766	0,011005
R_{ku} clean DLC & COF ₁₀	24	0,497284	2,6885	0,013422
R_{ku} clean DLC & COF ₂₀	24	0,502574	2,7267	0,012318
R_{ku} clean DLC & COF ₃₀	24	0,396683	2,0269	0,054961
R_{ku} clean DLC & COF ₅₀	24	0,437233	2,2803	0,032636
R_{ku} clean DLC & COF ₆₀	24	0,430274	2,2357	0,035840
R_{ku} clean DLC & COF ₈₀	24	0,370237	1,8694	0,074935
R_{ku} clean DLC & COF ₁₀₀	24	0,252279	1,2228	0,234327
R_{ku} clean DLC & COF ₁₅₀	24	0,037032	0,1738	0,863601
R_{ku} clean DLC & COF ₂₀₀	24	-0,065275	-0,3068	0,761865

Table 4. Coefficient of correlation R between the COF (within the range of 2000 - 3000 cycles) and R_{ku} of wear scar surfaces produced after 2400 cycles of the test. The significant correlation is highlighted in bold.

	N	Spearman R	t(N-2)	p-value
R_{ku} 2400 & COF ₂₀₀₀	24	0,234628	1,1321	0,269780
R_{ku} 2400 & COF ₂₂₀₀	24	0,360306	1,8117	0,083712
R_{ku} 2400 & COF ₂₄₀₀	24	0,384650	1,9545	0,063463
R_{ku} 2400 & COF ₂₆₀₀	12	0,640861	2,6400	0,024736
R_{ku} 2400 & COF ₂₈₀₀	12	0,605955	2,4088	0,036759
R_{ku} 2400 & COF ₃₀₀₀	12	0,518182	1,8176	0,102492

The correlation between the COF corresponding to the running-in period (5- 200 cycles) and geometrical parameters for the initial DLC surface are shown in Table 3. Total sample size was 24, i.e. 12 tests with 2400 and 4800 cycles, respectively. The correlation between R_a and the COF is significant for the level of confidence of 90 %. The sign of the correlation coefficient between R_a and the COF is negative, i.e. the COF decreases with an increase in roughness R_a . A similar relationship between the COF and R_z was established (not shown). Negative correlation between the COF and R_a (R_z) is in contradiction with the statement mentioned in the Introduction for the steady state period of the test, i.e. higher roughness leads to higher friction. Positive correlation between the COF and kurtosis contradicts with the theory developed by C. A. Kotwal and B. Bhushan [9].

Tribological properties of a material under lubricated conditions differ from those under non-lubricated ones. It is a well known fact in industry that tools show better performance under lubricating conditions if an optimal surface finish is used, such an interconnection between the COF and R_a is shown in Fig. 2, see reference [18]. The lubricant film can be effectively confined by surface asperities. The same conclusion was drawn by B. Bhushan et al. for diamond films [19]. In the case of carbon nanofibers (CNFs), it was suggested that nanofibers can be interlocked within the surface asperities [20,21]. On the other hand, surface kurtosis or excess is a measure of "peakedness" (or "flatness") of the height distribution function, therefore a more flat (i.e. most peaks of similar height) surface exhibits lower kurtosis. In conclusion, as related to the running-in period, correlation between the COF and R_a and the COF and R_{ku} indicates that average roughness and flatness of the clean DLC surface affect friction during an initial transient. By analogy with the aforementioned instances, surface morphology of the DLC coating influence the formation of a stable lubricant layer (or a transfer layer).

For the steady state period of the test, the most significant correlation between the COF (within the range of 2200 - 2800 cycles) and roughness parameters of the wear scar surfaces created after 2400 cycles is shown in Table 4. The correlation between the COF and kurtosis is positive, which means that optimal surface flatness and the COF value are related, namely the surface with perfect flatness should exhibit the lowest COF.

In the case of tests with 4800 cycles no significant correlation between the COF and geometrical parameters measured on the wear scar surfaces was found. However, insignificant correlation does not mean statistical independence of variables [22]. Regarding to the present study, the main reasons can be insufficient variation in geometrical parameters of the DLC surfaces, limited resolution of equipment used in the measurements, etc.

Conclusions

The present study focuses on the influence of geometrical parameters of the DLC surface on the tribological properties. Geometrical parameters were investigated on three kinds of surfaces, namely clean DLC and wear scar created after 2400 and 4800 cycles of the fretting test, respectively. Correlation between R_a and R_z parameters corresponding to the clean DLC surface and wear scar surfaces was found, which means that large asperities on the DLC surface affect the wear. In the course of the steady state period, i.e. 2200-2800 cycles of the test, the COF correlates positively with kurtosis measured on the wear scar surfaces after 2400 cycles, therefore optimal surface flatness is an important factor in the friction behavior of the DLC coating.

Acknowledgement

The work was supported by the Estonian Science Foundation grant Nr. 8696.

References

- [1] A. Erdemir, C. Donnet, Tribology of diamond-like carbon films: recent progress and future prospects, *Journal of Physics D*. 39 (2006) R311–R327.
- [2] K. Holmberg, H. Ronkainen, A. Laukkanen, K. Wallin, Friction and wear of coated surfaces scales, modelling and simulation of tribomechanisms, *Surface & Coating technology*. 202 (2007) 1034-1049.
- [3] J. Robertson, Diamond-like amorphous carbon, *Materials Science and Engineering*. 37 (2002)129–281.
- [4] J. Jiang, R.D. Arnell, The effect of substrate surface roughness on the wear of DLC coatings, *Wear*. 239 (2000) 1–9.

- [5] T. Ohana, M. Suzuki, T. Nakamura, A. Tanaka, Y. Koga, Tribological properties of DLC films deposited on steel substrate with various surface roughness, *Diamond & Related Materials*. 13 (2004) 2211–2215.
- [6] B. K. Gupta, A. Malshe, B. Bhushan and V. Subramaniam, Friction and wear properties of chemomechanically polished diamond films, *J. Tribology*. 116 (1994) 445-453.
- [7] P.J. Blau, On the nature of running-in, *Tribol. Int.* 38 (2005) 1007–1012.
- [8] P.J. Blau, Interpretations of the friction and wear break-in behavior of metals in sliding contact, *Wear*. 71 (1981) 29–43.
- [9] C. A. Kotwal, and B. Bhushan, Contact analysis of non-Gaussian surfaces for minimum static and kinetic friction and wear, *Tribology Transactions*. 39(4) (1996) 890-898.
- [10] S. Chandrasekaran, S. Sundararajan, Effect of microfabrication processes on surface roughness parameters of silicon surfaces, *Surf. Coat. Technol.* 188-189 (2004) 581-587.
- [11] V. Podgursky, R. Nisumaa, E. Adoberg, A. Surzhenkov, A. Sivitski, P. Kulu, Comparative study of surface roughness and tribological behavior during running-in period of hard coatings deposited by lateral rotating cathode arc, *Wear*. 268 (2010) 751-755.
- [12] V. Podgursky, E. Adoberg, A. Surzhenkov, E. Kimmari, M. Viljus, V. Mikli, M. Hartelt, R. Wäsche, M. Šíma, P. Kulu, Dependence of the friction coefficient on roughness parameters during early stage fretting of (Al,Ti)N coated surfaces, *Wear*. 271 (5–6) (2011) 853-858.
- [13] J.M. Lackner, W. Waldhauser, R. Berghauser, R.Ebner, B.Major, T.Schöberl, Structural, mechanical and tribological investigations of pulsed laser deposited titanium nitride coatings, *Thin Solid Films*. 453-454 (2004) 195-202.
- [14] A. C. Ferrari and J. Robertson, Resonant Raman spectroscopy of disordered, amorphous, and diamond like carbon, *PRB* 64 (2001) 075414-1 - 075414-13.
- [15] B. Bhushan, *Modern Tribology Handbook*, CDC Press, 2001, pp. 49–80.
- [16] T. Hill and P. Lewicki, *Statistics (Methods and Applications)*, StatSoft Inc., 2006.
- [17] W. Wieleba, The statistical correlation of the coefficient of friction and wear rate of PTFE composites with steel counterface roughness and hardness, *Wear*. 252 (2002) 719–729.
- [18] P. L. Menezes, K. Kailas and S.V. Kailas, Influence of roughness parameters on coefficient of friction under lubricated conditions, *Sādhanā*. 33 (3) (2008) 181–190.
- [19] B. Bhushan, V. V. Subramaniam, A. Malshe, B. K. Gupta, and J. Ruan, Tribological properties of polished diamond films, *J. Appl. Phys.* 74 (1993) 4174–4180.
- [20] A. Hirata, N. Yoshioka, Sliding friction properties of carbon nanotube coatings deposited by microwave plasma chemical vapor deposition, *Tribol. Int.* 37 (2004) 893-898.
- [21] E. Kimmari, V. Podgursky, M. Simunin, E. Adoberg, A. Surzhenkov, M. Viljus, M. Hartelt, R. Wäsche, I. Sildos, P. Kulu, Tribological behavior of carbon nanofibers deposited on superhard nanocomposite nACo coating, Submitted to *Tribology International*.
- [22] John Mandel, *The statistical analysis of Experimental data*, Dover Publications Inc. New York, 1984, pp.55.

**DISSERTATIONS DEFENDED AT
TALLINN UNIVERSITY OF TECHNOLOGY ON
*MECHANICAL ENGINEERING***

1. **Jakob Kübarsepp**. Steel-Bonded Hardmetals. 1992.
2. **Jakub Kõo**. Determination of Residual Stresses in Coatings & Coated Parts. 1994.
3. **Mart Tamre**. Tribocharacteristics of Journal Bearings Unlocated Axis. 1995.
4. **Paul Kallas**. Abrasive Erosion of Powder Materials. 1996.
5. **Jüri Pirso**. Titanium and Chromium Carbide Based Cermets. 1996.
6. **Heinrich Reshetnyak**. Hard Metals Serviceability in Sheet Metal Forming Operations. 1996.
7. **Arvi Kruusing**. Magnetic Microdevices and Their Fabrication methods. 1997.
8. **Roberto Carmona Davila**. Some Contributions to the Quality Control in Motor Car Industry. 1999.
9. **Harri Annuka**. Characterization and Application of TiC-Based Iron Alloys Bonded Cermets. 1999.
10. **Irina Hussainova**. Investigation of Particle-Wall Collision and Erosion Prediction. 1999.
11. **Edi Kulderknu**. Reliability and Uncertainty of Quality Measurement. 2000.
12. **Vitali Podgurski**. Laser Ablation and Thermal Evaporation of Thin Films and Structures. 2001.
13. **Igor Penkov**. Strength Investigation of Threaded Joints Under Static and Dynamic Loading. 2001.
14. **Martin Eerme**. Structural Modelling of Engineering Products and Realisation of Computer-Based Environment for Product Development. 2001.
15. **Toivo Tähe**maa. Assurance of Synergy and Competitive Dependability at Non-Safety-Critical Mechatronics Systems design. 2002.
16. **Jüri Resev**. Virtual Differential as Torque Distribution Control Unit in Automotive Propulsion Systems. 2002.
17. **Toomas Pihl**. Powder Coatings for Abrasive Wear. 2002.
18. **Sergei Letunovitš**. Tribology of Fine-Grained Cermets. 2003.
19. **Tatyana Karaulova**. Development of the Modelling Tool for the Analysis of the Production Process and its Entities for the SME. 2004.
20. **Grigori Nekrassov**. Development of an Intelligent Integrated Environment for Computer. 2004.

21. **Sergei Zimakov**. Novel Wear Resistant WC-Based Thermal Sprayed Coatings. 2004.
22. **Irina Preis**. Fatigue Performance and Mechanical Reliability of Cemented Carbides. 2004.
23. **Medhat Hussainov**. Effect of Solid Particles on Turbulence of Gas in Two-Phase Flows. 2005.
24. **Frid Kaljas**. Synergy-Based Approach to Design of the Interdisciplinary Systems. 2005.
25. **Dmitri Neshumayev**. Experimental and Numerical Investigation of Combined Heat Transfer Enhancement Technique in Gas-Heated Channels. 2005.
26. **Renno Veinthal**. Characterization and Modelling of Erosion Wear of Powder Composite Materials and Coatings. 2005.
27. **Sergei Tisler**. Deposition of Solid Particles from Aerosol Flow in Laminar Flat-Plate Boundary Layer. 2006.
28. **Tauno Otto**. Models for Monitoring of Technological Processes and Production Systems. 2006.
29. **Maksim Antonov**. Assessment of Cermets Performance in Aggressive Media. 2006.
30. **Tatjana Barashkova**. Research of the Effect of Correlation at the Measurement of Alternating Voltage. 2006.
31. **Jaan Kers**. Recycling of Composite Plastics. 2006.
32. **Raivo Sell**. Model Based Mechatronic Systems Modeling Methodology in Conceptual Design Stage. 2007.
33. **Hans Rämmal**. Experimental Methods for Sound Propagation Studies in Automotive Duct Systems. 2007.
34. **Meelis Pohlak**. Rapid Prototyping of Sheet Metal Components with Incremental Sheet Forming Technology. 2007.
35. **Priidu Peetsalu**. Microstructural Aspects of Thermal Sprayed WC-Co Coatings and Ni-Cr Coated Steels. 2007.
36. **Lauri Kollo**. Sinter/HIP Technology of TiC-Based Cermets. 2007.
37. **Andrei Dedov**. Assessment of Metal Condition and Remaining Life of In-service Power Plant Components Operating at High Temperature. 2007.
38. **Fjodor Sergejev**. Investigation of the Fatigue Mechanics Aspects of PM Hardmetals and Cermets. 2007.
39. **Eduard Ševtšenko**. Intelligent Decision Support System for the Network of Collaborative SME-s. 2007.
40. **Rünno Lumiste**. Networks and Innovation in Machinery and Electronics Industry and Enterprises (Estonian Case Studies). 2008.

41. **Kristo Karjust.** Integrated Product Development and Production Technology of Large Composite Plastic Products. 2008.
42. **Mart Saarna.** Fatigue Characteristics of PM Steels. 2008.
43. **Eduard Kimmari.** Exothermically Synthesized B₄C-Al Composites for Dry Sliding. 2008.
44. **Indrek Abiline.** Calibration Methods of Coating Thickness Gauges. 2008.
45. **Tiit Hindreus.** Synergy-Based Approach to Quality Assurance. 2009.
46. **Karl Raba.** Uncertainty Focused Product Improvement Models. 2009.
47. **Riho Tarbe.** Abrasive Impact Wear: Tester, Wear and Grindability Studies. 2009.
48. **Kristjan Juhani.** Reactive Sintered Chromium and Titanium Carbide-Based Cermets. 2009.
49. **Nadežda Dementjeva.** Energy Planning Model Analysis and Their Adaptability for Estonian Energy Sector. 2009.
50. **Igor Krupenski.** Numerical Simulation of Two-Phase Turbulent Flows in Ash Circulating Fluidized Bed. 2010.
51. **Aleksandr Hlebnikov.** The Analysis of Efficiency and Optimization of District Heating Networks in Estonia. 2010.
52. **Andres Petritšenko.** Vibration of Ladder Frames. 2010.
53. **Renee Joost.** Novel Methods for Hardmetal Production and Recycling. 2010.
54. **Andre Gregor.** Hard PVD Coatings for Tooling. 2010.
55. **Tõnu Roosaar.** Wear Performance of WC- and TiC-Based Ceramic-Metallic Composites. 2010.
56. **Alina Sivitski.** Sliding Wear of PVD Hard Coatings: Fatigue and Measurement Aspects. 2010.
57. **Sergei Kramanenko.** Fractal Approach for Multiple Project Management in Manufacturing Enterprises. 2010.
58. **Eduard Latõsov.** Model for the Analysis of Combined Heat and Power Production. 2011.
59. **Jürgen Riim.** Calibration Methods of Coating Thickness Standards. 2011.
60. **Andrei Surzhenkov.** Duplex Treatment of Steel Surface. 2011.
61. **Steffen Dahms.** Diffusion Welding of Different Materials. 2011.
62. **Birthe Matsi.** Research of Innovation Capacity Monitoring Methodology for Engineering Industry. 2011.
63. **Peeter Ross.** Data Sharing and Shared Workflow in Medical Imaging. 2011.
64. **Siim Link.** Reactivity of Woody and Herbaceous Biomass Chars. 2011.

65. **Kristjan Plamus**. The Impact of Oil Shale Calorific Value on CFB Boiler Thermal Efficiency and Environment. 2012.
66. **Aleksei Tšinjan**. Performance of Tool Materials in Blanking. 2012.
67. **Martinš Sarkans**. Synergy Deployment at Early Evaluation of Modularity of the Multi-Agent Production Systems. 2012.
68. **Sven Seiler**. Laboratory as a Service – A Holistic Framework for Remote and Virtual Labs. 2012.
69. **Tarmo Velsker**. Design Optimization of Steel and Glass Structures. 2012.
70. **Madis Tiik**. Access Rights and Organizational Management in Implementation of Estonian Electronic Health Record System. 2012.
71. **Marina Kostina**. Reliability Management of Manufacturing Processes in Machinery Enterprises. 2012.
72. **Robert Hudjakov**. Long-Range Navigation for Unmanned Off-Road Ground Vehicle. 2012.
73. **Arkadi Zikin**. Advanced Multiphase Tribo-Functional PTA Hardfacings. 2013.
74. **Alar Konist**. Environmental Aspects of Oil Shale Power Production. 2013.
75. **Inge Roos**. Methodology for Calculating CO₂ Emissions from Estonian Shale Oil Industry. 2013.
76. **Dmitri Shvarts**. Global 3D Map Merging Methods for Robot Navigation. 2013.
77. **Kaia Lõun**. Company's Strategy Based Formation of e-Workplace Performance in the Engineering Industry. 2013.
78. **Maido Hiimaa**. Motion Planner for Skid-Steer Unmanned Ground Vehicle. 2013.
79. **Dmitri Goljandin**. Disintegrator Milling System Development and Milling Technologies of Different Materials. 2013.
80. **Dmitri Aleksandrov**. Light-Weight Multicopter Structural Design for Energy Saving. 2013.
81. **Henrik Herranen**. Design Optimization of Smart Composite Structures with Embedded Devices. 2014.
82. **Heiki Tiikoja**. Experimental Acoustic Characterization of Automotive Inlet and Exhaust System. 2014.
83. **Jelena Priss**. High Temperature Corrosion and Abrasive Wear of Boiler Steels. 2014.
84. **Aare Aruniit**. Thermoreactive Polymer Composite with High Particulate Filler Content. 2014.
85. **Dmitri Gornostajev**. Development of the Calculation Method for Barge Hull. 2014.

86. **Liina Lind.** Wear of PVD Coatings on Fineblanking Punches. 2014.
87. **Nikolai Voltšihhin.** Design and Technology of Oxides-Containing Ceramic-Based Composites. 2014.